UNIVERSITY OF CALIFORNIA SAN DIEGO

Dexterous Robotics for Image-Guided Needle Insertion

A dissertation submitted in partial satisfaction of the
requirements for the degree
Doctor of Philosophy

in

Electrical Engineering (Intelligent Systems, Robotics, and Control)

by

Dimitrious Schreiber

Committee in charge:

Michael Yip, Chair
Nikolay Atanosav
Vikash Gilja
Tania Morimoto
Alexander Norbash
Rebecca Theilmann

2022

The dissertation of Dimitrious Schreiber is approved, and it is acceptable in quality and form for publication on microfilm and electronically.

University of California San Diego

2022

DEDICATION

To my family, who helped and supported me through this journey. My parents, Ruth and Sebastian, provided me the opportunity, confidence, and space to explore while pushing me to reach outside my comfort zone to try new things. My partner and best friend, Nicole, who supported me throughout the highs and lows. Her silliness brought endless joy to my day-to-day life. I am grateful for their care and love throughout this time.

TABLE OF CONTENTS

LIST OF FIGURES

LIST OF TABLES

ACKNOWLEDGEMENTS

I thank my advisor, Dr. Michael Yip, for providing me the space, support, and opportunity to learn. I have learned a great deal from him, not only about engineering and research but on the professional skills required to succeed in my career.

I would also like to thank my committee members, Dr. Nikolay Atanosov, Dr. Vikash Gilja, Dr. Tania Morimoto, Dr. Alexander Norbash, and Dr. Rebecca Thielmann. I greatly appreciate their availability for discussion both on my research and career. Furthermore, I would like to thank Dr. Rebecca Thielmann for mentorship generally on the graduate school process, MRI experiments, clinical device application, and volumetric medical imaging. Dr. Alexander Norbash, for providing guidance, mentorship, and resources on the medical applications for this work, CT experiments. I am grateful for funding support that enabled me to explore my research field: National Science Foundation's Graduate Research Fellowship, ARCS Foundation Scholarship, UC San Diego's Accelerating Innovations to Market grant, Shah Family Fellowship, Chancellor's Research Excellence Scholarship, and Electrical and Computer Engineering Department Fellowship.

Additionally, I would like to thank Dr. Zachary Berman, Dr. Quinn Meisinger, Dr. Jeet Minocha, Dr. Michael Taddonio, Dr. Anthony Tadros, and Dr. Sean Tutton for supporting procedural observations and discussion of clinical needs.

Finally, I would like to thank all of the members of ARCLab and the Contextual Robotics Institute who I have had the pleasure of becoming friends with and working alongside: Andrew Bilan, Derek Chen, Zih-Yun (Sarah) Chiu, Christopher D'Ambrosia, Dr. Nikhil Das, Peter Gavrilov, Daniel George, Taylor Henderson, Hanpeng Jiang, Jacob Johnson, Lucas Jonasch, Calvin Joyce, Hoi Man (Kevin) Lam, Guosong Li, Jason Lim, Dr. Shan Lin, Dr. Fei Liu, Jingpei Lu, Elizabeth Peiros, Casey Price, Dr. Ahmed Qureshi, Dr. Florian Richter, Andrew Saad, Daniel Shak, Harleen Singh, Jared Walker, Julie Yu, Zhaowei Yu, Yuheng Zhi, and Renjie Zhu.

Thank you all for your friendship, guidance, and help on this journey. I am grateful to

have the chance to meet and work-alongside you all.

Chapter 2 is, in part, a reprint of material from D. Schreiber, D. Shak, A. Norbash, M. Yip, "An Open-Source 7-Axis, Robotic Platform to Enable Dexterous Procedures within CT Scanners," in 2019 IEEE/RSJ International Conference on Intelligent Robots and Systems (IROS). The dissertation author is the primary author of this paper.

Chapter 3 is, in part, a reprint of material from D. Schreiber, Z. Yu, H. Jiang, T. Henderson, G. Li, J. Yu, R. Zhu, A. Norbash, M. Yip, "CRANE: a 10 Degree-of-Freedom, Tele-surgical System for Dexterous Manipulation within Imaging Bores" in 2022 IEEE International Conference on Robotics and Automation (ICRA) and, in part, has been submitted for publication of the material as it may appear in IEEE Transactions on Robotics, 2023, D. Schreiber, Z. Yu, T. Henderson, A. Norbash, M. Yip. The dissertation author is the primary author of these papers.

Chapter 4, in part, has been submitted for publication of the material as it may appear in IEEE Transactions on Robotics, 2023, D. Schreiber, Z. Yu, T. Henderson, A. Norbash, M. Yip. The dissertation author is the primary author of this paper.

VITA

2017	Bachelor of Science in Electrical Engineering (Intelligent Systems, Robotics, and Control), University of California San Diego
2020	Master of Science in Electrical Engineering (Intelligent Systems, Robotics, and Control), University of California San Diego
2022	Doctor of Philosophy in Electrical Engineering (Intelligent Systems, Robotics, and Control), University of California San Diego

PUBLICATIONS

D. A. Schreiber, D. B. Shak, A. M. Norbash, and M. C. Yip, "An Open-Source 7-Axis, Robotic Platform to Enable Dexterous Procedures within CT Scanners," in *IEEE/RSJ International Conference on Intelligent Robots and Systems*, pp. 386-393, 2019.

D. A. Schreiber*, F. Richter*, A. Bilan, P. V. Gavrilov, H. L. Man, C. H. Price, K. C. Carpenter, and M. C. Yip, "ARCSnake: An Archimedes' Screw-Propelled, Reconfigurable Robot Snake for Complex Environments," in *IEEE International Conference on Robotics and Automation*, pp. 7029-7034, 2020. (* indicates equal contribution)

D. A. Schreiber, Z. Yu, H. Jiang, T. Henderson, G. Li, J. Yu, R. Zhu A. M. Norbash, and M. C. Yip, "CRANE: a 10 Degree-of-Freedom, Tele-surgical System for Dexterous Manipulation within Imaging Bores," in *IEEE/RSJ International Conference on Intelligent Robots and Systems*, pp. 5487-5494, 2022.

M. Yip, **D. Schreiber**, and A. Grant, "Cable driven hydraulic rolling diaphragm transmission and servo-system," US11391303B2, 2022

ABSTRACT OF THE DISSERTATION

Dexterous Robotics for Image-Guided Needle Insertion

by

Dimitrious Schreiber

Doctor of Philosophy in Electrical Engineering (Intelligent Systems, Robotics, and Control)

University of California San Diego, 2022

Michael Yip, Chair

Image-guided surgery (IGS) enables accurate and safe minimally invasive treatment of diseases, including cancer and chronic pain, with needle-like tools via a percutaneous approach. During a percutaneous IGS, the physician plans, inserts, and adjusts the needle with image feedback to help them "close the loop" and compensate for the accuracy limitation of free-hand adjustment and patient physiological motion. When performed with Computed Tomography (CT) guidance, robots provide high positional accuracy, enabling fewer intermediate control scans and lower radiation doses. To fit into the clinical workflow, the robots must be simple to set up and operate within the confined imaging bore while retaining sufficient dexterity to insert and manipulate the needle. This thesis explores CT-guided needle insertion, focusing on technologies

required for dexterous manipulation of needles within an imaging bore, considering the interplay between device kinematics, mechatronics, planning, and control. The clinical problem and existing guidance technologies are reviewed. From this, abstract and measurable clinically motivated metrics for in-bore dexterity applicable to general-purpose intra-bore image-guided needle placement robots are defined and applied to different procedure areas. Two generations of redundant CT-compatible robots are developed and tested both on bench-top and in-situ. The designs' ability to meet clinical requirements is analyzed. Specifically, it is demonstrated that the redundant linkage design provides dexterity across various human morphology, and that the transmission, sensing, and the control meets the clinical requirements for target accuracy during an in-situ evaluation. Finally, methods for automated robot planning and control for intra-bore needle manipulation from image guidance are explored.

Chapter 1

Introduction

1.1 Motivation

Interventional radiologists (IRs) perform minimally invasive procedures under real-time medical imaging guidance, such as ultrasound, fluoroscopy, computed tomography (CT), and magnetic resonance imaging (MRI). Within Interventional Radiology, CT guidance is the standard-of-care for biopsy and ablation procedures in the abdominal region for a wide variety of diseases. In recent years, percutaneous CT-guided procedures have increased dramatically in both type and frequency due to their decreased complications and recovery time compared to more invasive open-surgery and laparoscopic surgery, enabled by technique and technological advances [JDC+18, Len18]. This approach allows the minimally invasive diagnosis and therapy of numerous diseases. These include lung, liver, and kidney cancer and chronic lumbar-sacral spine pain, which in combination affect approximately one-in-six people during their lifetime [noae, noac]. Physicians use needle-like tools to diagnose and treat these diseases, including fine needles for injection and aspiration, core-biopsy needles, and ablation probes. However, despite these strong clinical advantages, accurately inserting the needle is challenging during these procedures, especially for accessing small lesions within the abdominal and thoracic region. In United States, approximately

2 million new cases of cancer are diagnosed yearly [noa15] with 600,000 deaths [Can22] resulting in direct healthcare costs of over 200 billion dollar [CBG22]. Due to an increasing median population age [Age] and significantly higher prevalence of cancer in older populations [Ris00, TDC+10], the incidence is expected to increase nearly 50% by 2050 [Wei21, SSH+09].

Typically, CT-guided procedures involve multiple steps where the IRs alternate between manually and incrementally advancing the needle-like tool and stepping away from the gantry to scan the patient. The physician must balance frequency of scanning to understand the in-body environment with the radiation exposure for both the patient and physician. This trade-off directly affects tip-to-target accuracy [Len18], [YLL+09]. Frequently, the IR withdraws the patient from the imaging bore for needle insertion between scans for improved ergonomics. The combination of delayed feedback and freehand control presents a challenge when high accuracy is required and results in physicians performing a move-and-wait strategy [FS67] where they scan the patient, view the scan, make a conservative needle adjustment, and scan again. These procedural challenges results in the average diagnosis necessitating 1.7 insertion attempts [ZSS+20] with increased frequency of for repeat procedure [CKS+21, ZSS+20], severe side-effects, and cost [WSWW11, DTSD+19, IGG+19, MPF+10, BLE+18].

1.2 Navigated Needle Insertion

Clinically, navigation systems that track the needle's base position providing real-time needle visualization have received high adoption due to their simple setup [noad, noah] and demonstrated improvements in clinical outcomes [KBFD21, WTW+14, BLE+18, WSH+11a, BSE+19, SJL+21, WSOB12a]. However, these systems' performance is limited within the imaging bore [AHF+15] and have decreased clinical accuracy in comparison with robotic approaches [vBWSH21].

Recent work presented many challenges relating to decreased adoption of image-guided

robotics outside of orthopedic and neurosurgery [FTH22] with a strong focus on the procedural workflow changes required to integrate the device overcoming their added value. Robotics can improve tip-to-target accuracy and ergonomics while decreasing radiation exposure by providing real-time visualization of the system state to avoid many of the current move-and-wait challenges and allowing for the precise adjustment of tools while the patient is within the bore [CTL+15, LGR+21]. This decreases the potential for organ displacement due to the patient being moved back and forth from the bore combined with less physiological motion due to a shorter time between sensing and acting.

A considerable number of robotic platforms have been developed for use for trans-abdominal and trans-thoracic access, where the robot must ultimately operate well within the CT bore. Existing robotic platforms have demonstrated excellent needle placement accuracy, including small size systems with low weight and large platforms with a fully active workspace with numerous methods of inserting needles [UBM21, SMW+21] and a variety of levels of human-involvement required during the procedure. However, existing systems fail to offer automatic hands-free device setup, control, and needle insertion within the imaging bore; resulting in performance compromises, the need for clinical workflow changes with increased overhead, the loss of existing abilities, or decreased safety in some situations [AHF+15, SBM16, SES+13, BDSR+18a, SES+13, BLE+18, MBG+06].

Research robotics have been developed and demonstrated improvements for tip-to-target accuracy and ergonomics while decreasing radiation exposure by providing real-time visualization of the system state to avoid many of the current move-and-wait challenges and allowing for the precise adjustment of tools while the patient is within the bore [CTL+15, LGR+21] by enabling the physician to know the location of their tool in real-time with lower potential for organ displacement due patient remaining stationary within the bore and a shorter time between sensing and acting decreasing the likely-hood of physiological motion.

1.3 Clinical Workflow

An image-guided percutaneous surgical procedure has three main phases: Preoperative Setup, Procedure Planning, and Procedure Execution, described in detail below. The procedure is performed within an imaging scanners, such as a CT scanner, frequently consist of an imaging gantry and a couch. The imaging gantry has a bore that the patient resides within during imaging. This bore can be a physical bore, such as in a CT or MR scanner, or a virtual constraint, such as in a C-arm fluoroscopy scanner or a medical linear accelerator. The patient rests on a couch consisting of a base and a table. The imaging gantry is typically stationary for CT scanners, and the tabletop of the couch moves in and out of the bore.

1. *Preoperative Setup Phase* – Before the surgery, the physician reviews the preoperative images to determine a rough plan of the procedure approach, including patient positioning (e.g., prone, supine, left or right lateral recumbent). These images are typically from initial diagnostic imaging scans (e.g., CT, MR) used to diagnose the existence of an ailment that requires an intervention. Frequently, these scans are from days, weeks, or months prior.

2. *Procedure Planning Phase* – With the patient in position, the physician takes an initial volumetric scan to provide an accurate view of the patient's anatomy with which they can plan their precise needle-insertion approach. They must consider the in-body obstacles (e.g., bone, blood vessels, other organs) and the confined space they are working in (e.g., imaging bore, patient) to avoid collisions between the environment and needle. The physician can select their preferred visualization (2D slices or 3D rendering) within the scanner software during this step. If using a robot, an additional, non-trivial challenge involves setting up the robot to the planned trajectory, assuming it is reachable and stable concerning the kinematics of the robot.

3. *Procedure Execution Phase* – the physician inserts the needle into the patient towards the target point within the patient's body. Typically, the physician alternates between

making minor adjustments and inserting the needle with intermediate control scans. Upon complications or after multiple failures of attempting to navigate the needle to the target, the physician may loop back to *Step 2 - Procedure Planning Phase* and determine a new needle insertion trajectory and begin again. Inserting and adjusting the needle requires up to $10N$ of axial force and $0.05Nm$ of torque [Wal10, PSV+16, WHS+08a]. The insertions may be up to $140mm$ [WLH+14] deep while requiring $< 4mm$ position and $< 4^\circ$ orientation error [DMGS+17].

A primary consideration is the space within the imaging bore. The space available for manipulation is limited to the area between the patient, patient table, and the scanner bore. Withdrawing the patient from the scanner provides more working room. However, this increases the procedure time and the possibility of a mismatch between the previously captured image and the current patient state due to patient physiological motion or patient shifting. Working within the bore allows for shorter and more precise procedures but decreases the physician's ergonomics as they must reach between a narrow scanner bore and the patient. Even then, they must remove their hands and body from the bore between intermittent scanning to avoid radiation. Surgical robot platforms can enable more ergonomic manipulation of surgical instruments within the imaging bore and, with the appropriate design, even increase the space available versus a physician by providing a lower profile.

1.4 Related Works for Robotic Percutaneous Needle Insertion

This related work focuses on several device design attributes significantly affecting clinical workflow (e.g., device setup, control), value-add (e.g., accuracy, procedure time, general-purpose applicability), and safety (e.g., failure mode, device energy). The primary focuses are the device's kinematic structure and workspace, needle interface, and automation level for planning and control.

1.4.1 Robot Design: Device Setup, Workspace, and Safety

The surgical robot platform's mounting location (e.g., floor, scanner couch, or patient) sets many constraints on the device's kinematic design, size, and mass. This affects the device's setup, workspace, and safety. Setup is frequently time-consuming and challenging and can require restarting from the beginning due to device self-collisions and environment collissions [GBL+18, KBFD21, LTK+06]. Large workspace fully-active systems provide many advantages, including lower procedure setup complexity, remote teleoperation, and the ability to regulate cartesian space tip stiffness to limit tissue damage in the case of gross or respiratory patient motion [KSKK17, MAM15]. We discuss and compare works focused on these attributes with multi-organ applicability in the thoracic and abdominal regions. Table 1.1 provides comparison of several fully-active systems which can adjust the needles angle and position.

Floor-mounted platforms (e.g., Innomotion, Maxio, Virtobot) are frequently fully active and simple to set up with large active workspaces. However, they can pose a safety risk in the case of relative motion between the patient on the scanner couch and the robot platform [CTL+15, WKK+17, HMK+18, KHK+20, YWQ+10, TATPO+11a, EPN+10, EPB+14, noag, GHT+22]. Frequently, these designs use industrial robots with a custom end-effector (EE), [TATPO+11a, WKK+17] which occupy significant space within the scanner bore, have large inertia, and are not passively backdrivable. This limits the ability of the device to perform in-bore needle insertion, to adjust for unexpected patient motion safely, results in high energy within the system during robot motion, and is difficult to remove in case of system failure. Therefore, the needle insertions are typically performed outside the scanner bore and with the patient under deep sedation with decreased accuracy, longer procedure time, higher risk of complications, and higher cost than general or local anesthesia.

Couch-mounted systems (e.g. Acubot/PAKY, I-Sys/Biorob) [DLJ+98, SES+13, MFP+01a, SSNY19, GSS20, LN00, HFG+03, MGR+08a, SCP+03a, KKT+14, CWL+05, SHvK+17] may be fully active or partially active with the use of setup joints. These devices are strapped or bolted to

Table 1.1: *Fully Actuated* Robots for In-bore Abdominal and Thoracic Percutaneous Interventions

Project	Mounting	Active DoF	Active Pos. Space	Active Ori. Space	Needle Insertion Method	In-bore Volume	Control Method	Manually Positionable
ZeroBot [HKM+17, KHK+20]	Floor	6	Large	Large	Prismatic	Large	IK	No
[TOC05, TCO08, TKCM07, CAO+07, OT08]	Floor	7	Large	Large	Prismatic	Low	IK w/ col. detect.	No
Acubot/PAKY [SCP+03a, SPB+02, CPG+05, DLJ+98, MFP+01a, SKD+08a, CWL+05]	Couch	6	Medium	Medium	Prismatic	Low	IK	Yes
I-Sys/B-Rob II [SES+13, MPS+14]	Couch	5	Small	Large	Passive	Low	IK	Yes
Innomotion [MGR+08a, HFG+03, ZME+11]	Couch	6	Medium	Medium	Prismatic	High	IK	Yes
Open 7-DoF [SSNY19]	Couch	7	Medium	Medium	Prismatic	Low	IK	No
LPR [OT08]	Patient	5	Medium	Low	Clutching	High	IK	No
CTBot [MBG+06, MDG+05, MBP+08, PBB+09]	Patient	5	Low	Low	Clutching	Medium	IK	No
XACT [BDSR+18b]	Patient	5	Low	Medium	Gear	Low	IK	Yes
CRANE (ours)	Floor/Couch	8	Large	Large	Clutch	Low	Automated Planning	Yes

the couch and passively move with the patient during couch motion for intraoperative scanning. However, scanner attachment can be challenging and poses a risk of system damage and patient injury in the case of improper fixation [noaa]. Manual setup joints significantly increase device adjustability while retaining a low profile and stiffness without backlash but are challenging to use, especially without gravity compensation for the device's weight, and preclude the option of a fully automatic device setup. Instead, they require the physician to carefully manipulate the device to the correct position by hand while considering potential collisions with the environment. Many devices in this class use small and highly geared non-backdriveable motors. This limits their dynamic performance and requires patients to be under deep sedation.

Patient-mounted systems (including Light Puncture Robot, XACT, and Robopsy) are small and intrinsically compensate for gross patient and table motion improvement [MDG+05,MBP+08, MBG+06,HBCF16a,WHS+07,WLP+19a,YJY+17,WHS+09,LSS+13,LSL+19,N21]. However, they frequently occupy more space in the scanner and possess less dexterity. Additionally, it can be difficult to balance point pressure application with sufficient stability and rigidity for accurate needle insertion when mounting to a patient.

Throughout these device designs, in-bore workspace and dexterity analysis primarily focus on swept volume accessible by the robot's tip in free-space [MBG+06, HBCF16a, YJY+17, JYY+17], potentially with a single reference human body size [WLP+19a] or the ability to reach target organs and tumors in specific patient cases [BGBE18]. [SSNY19] used the orientable needle insertion transform on a demonstration human mesh surface as a proxy for in-body reachability. These evaluations are limited in their general purpose applicability and do not consider dexterity in patients with large body habitus.

1.4.2 Needle Interface

Needle interfaces assist a physician in inserting the needle into the patient while maintaining a target orientation and position. They must be sterile, safe, and replaceable. Many needle inter-

faces exist, including passive guides [DLJ+98,SES+13,SCP+03a,MGR+08a,BZJ+08a,KKT+14] and active mechanisms [FIS+21,YWQ+10,SSNY19,SHOM15a,SWH+09a,SKD+08a,LGR+21]. Passive guides orient and position the needle at the surface entry point where the physician manually inserts the needle. They decrease the unintentional application of torques and forces to the needle, deflecting it and decreasing accuracy.

Active needle drivers enable precise and quick insertion while the physician remains remote and away from radiation or contagious diseases. Existing active needle driver designs have utilized numerous mechanisms including limited travel prismatic axis [YWQ+10, SSNY19, SHOM15a], friction rollers [SWH+09a, SHOM15a], clutching graspers [FIS+21, GMGH+18a, BZJ+08a, FKP+20], and rack-and-pinion [LGR+21] while incorporating aspects such as force sensing and safety release [SKD+08a]. These active designs have high complexity and limited replaceability resulting in potential challenging sterilization procedures and limited compatibility with different needles and probes while providing sufficient gripping force to insert them without slipping or damaging the probe itself [SAM+02].

1.4.3 Device Planning, Setup, and Control

Device setup and user control methods significantly affect the *Procedure Execution Phase* and fall into three main categories: direct joint control, EE control, and automated.

Direct joint control [CSA+14, SWH+09a, noab, BGT+21] has the physician manually control the robot joints. The system helps a physician perform a static insertion trajectory and achieve fine adjustment. Stereotactic frames are examples of this in image-guided surgery today. However, they can be complex and unintuitive to set up and plan for due to their frequently unintuitive kinematics and joint limitations [SBM16].

Teleoperated EE control [noaf,BWM+04,MBG+06,HBCF16a,YJY+17,SSNY19,MBP+08] via Inverse Kinematics (IK), either in robot coordinates or image frame, allows a physician to abstract away the device's joint motions and make precise needle adjustments. This is the most

common operating model today, especially for small workspace and under-actuated systems, which require manual setup for rough positioning and do not have to solve large-scale motion planning problems for device setup. However, with this approach, the responsibility of considering potential collisions with obstacles in the environment and limitations of the robot's dexterity is left to the physician operators, which is cognitively challenging to keep track of given the variety and complexity of linkage designs across different platforms. More broadly within the field of robotics, IK algorithms exist that locally consider collision avoidance, and device dexterity [HS87, BB98, AGS+13, HC21] but have not yet been applied to the problem of in-bore needle insertion.

Automated EE control with planning directly in imaging space [PBN+21, GDBNR21] enables the physician to select their target needle insertion trajectory from which they guide the system to a course alignment. Then the robot automatically performs the fine adjustment based on image tracking, decreasing the physician's cognitive burden and improving procedural accuracy [vBWSH21]. However, the physician is still responsible for the device setup for course alignment and environmental collision considerations. Existing works have included methods for environmental and self-collision checking [CAO+07, TCO08, TOC05, MBP+08, HTV+21] prior to a commanded motion. However, the physician still must determine the collision-free robot trajectory themself.

Collision-free motion planning from image-space needle trajectory allows the physician to select their target needle insertion trajectory and then allows the robotic system to solve the associated motion planning problem to avoid self and environment collisions while supporting angulation adjustment during the procedure. This is most relevant in large fully-active workspace systems, which can perform automated setup, allows the physician to focus on the higher-level surgical tasks, and decreases the cognitive overhead of introducing a robotic system. Ideally, the physician is confident in the system's ability to follow through on this task regardless of the specific patient and needle insertion location. Previous works on collision-free planning for

image-guided needle insertion provide methods of planning for nominal trajectory insertions outside the bore [EFP+16, LXL+16, LQD+19] or in simulation within a scanner bore [BGBE18] without considering dexterity required for needle pose adjustment around the nominal insertion pose for device kinematics or collision constraints with the imaging bore.

Significant research exists for assisting physicians in determining optimal trajectories for needle insertion within the patient's body during the *Procedure Planning Phase* to perform the primary surgical task (e.g., biopsy, ablation, deep brain stimulation) while optimizing for a variety of objectives (e.g., obstacle avoidance, cranial-caudal needle angulation, needle deflection, tissue deflection, brachytherapy radiation distribution, ablation zone) from medical imaging data [SEHC+21]. Many approaches exist for both straight [SES+11, PAVE20, HCE17, GSY+14, LKKC12, CMG09, TKII18, SJA+10, RCNY+14] and steerable needles [ABG08, NKS+20, SHvK+17, DXA+10, vdBPA+11, XDAG08, PA10]. A select few of these methods integrate this in-body needle trajectory planning with robot planning for out-of-bore insertion [LXL+16, LQD+19, BSK18] or within a simulated environment for in-bore [BGBE18].

1.4.4 Scanner Image Feedback

When performing a procedure, the physician's target is determined within the imaging space and they perform control in their world coordinate system. This requires a registration between these two spaces, providing a mapping between target poses for insertion and motions to achieve the insertion. When performing a manual procedure, the physician performs this registration and tracking internally, and then decides based on this internal tracking how to best adjust the needle without realtime feedback. However, both the internal registration and performing the adjustment by hard are difficult. Therefore, systems and methods [CBCV15] have been developed to automate the tracking. Automated tracking has been applied both for real-time visualization and for robot control. This related works focuses on two areas: methods for image-based device tracking, and methods of using the tracking to guide a robot performing a needle

insertion. [CBCV15] provides a more general overview of navigational tools for Interventional Radiology and Interventional Oncology.

Tracking fundamentally is determining a registration between the image-space and task-space. Image-space tracking is primarily performed using fiducials (e.g., spheres [CBCV15, PKK16, LMWS11, FJM$^+$21, Qua], bars, arbitrary geometries [HBCF16b, RBF21, LYC$^+$15]) and anatomical surface registration [JSF$^+$06]. Pose estimation of stereotactic rigid bodies is solved as classical computer vision problem using multiple point fiducial correspondence [Yan10, DNMK08, FRD$^+$12] and as surface matching problem [HBCF16b]. The fiducials are directly segmented using classical [FRD$^+$12] or deep learning segmentation techniques [RBF21] in both 2D [Yan10, PKK16] and 3D [FRD$^+$12, RBF21]. For fiducial based methods, the fiducial arrangement within the rigid body body is critical for good accuracy at the clinically relevant location [WM04, PKK16, WM04]. Fiducials typically consist of radio-opaque materials, such as plastic, ceramic, and metal [You, ORK$^+$19]. Approaches work directly off 3D volumetric data [DNMK08, FRD$^+$12, HBCF16b, FJM$^+$21] or 2D projecthions [MWX08, PKK16]. 3D volumetric data is provided openly for CT imaging and 2D data is available from flouroscopic and C-arm imaging. The use of 2D projections can enable higher-speed tracking with low radiation dose [MWX08]. Real-time world-space tracking is performed using wireless methods (e.g., optical [CBCV15, LYC$^+$15, Qua] or magnetic tracking [CBCV15, LMWS11, CIV, Int]) and hardware methods with encoded arms [Tur]. This tracked information can help a physician directly perform the insertion them-self by providing real-time feedback via a graphical 2D/3D visualization [WSOB12b, CBCV15, WSH$^+$11b, Qua, Int], laser overlay [WSOB12b, CBCV15], or robotic guidance.

Robotic needle insertion methods consist of two primary groups: image-space teleoperation and visual servoing. Given a registered robot, the physician teleoperates the robot motions to adjust the needle based on visually observing the most recent image, as described above (Sect. 1.4.3). Visual servoing methods automate the process of interpreting the im-

Table 1.2: *Fully Actuated* Robots for In-bore Abdominal and Thoracic Percutaneous Interventions

Paper	Robot Model	Needle Model	Imager	Sensors
[SHv+17, Sha18]	Yes	Yes	CT	EM
[LWDW19]	Yes	No	CT	Camera
[MJY+19]	Yes	No	CT	EM
[SFJ+05, JSF+06]	Yes	No	CT	Camera
[TTP+11]	Yes	No	CT	Camera
[PMP+03, PSW+00, BWM+03]	No	No	Ultrasound, CT, Fluoroscopy	–
[ÖVP+20]	Yes	No	CT	–
[SKP+17, MPP+06, CHGS19]	Yes	No	MRI	–

ages and adjusting the robot. Methods use varying levels of environment modeling (e.g., robot, needle) for control and are tested within different imagers (e.g., ultrasound, fluroscopy, CT, and MRI). Additionally, a variety of secondary sensors (e.g., cameras, magnetic trackers, encoders) are used for needle-base pose tracking. Based on their modeling and control scheme, these range from fully model-free approaches without a robot or needle model [PMP+03, PSW+00, BWM+03], to methods using a robot model without modeling needle tissue interactions [LWDW19, MJY+19, ÖVP+20, SKP+17, MPP+06, CHGS19], to fully-modeled approaches performing needle steering [SHv+17, Sha18]. Model-free approaches improve generalizability due requring less understanding of the environment but may neglect aspects of the system (e.g., joint kinematics, bevel-tip needle steering) decreasing performance (e.g., slow convergence, decreased accuracy). Model-based methods enable faster convergence and improved control. However, generating these model can be time-consuming or difficult to apply clinically. An overview of existing works performing image-guided closed-loop needle insertion within an imaging bore is provided in Table 1.2.

1.5 Thesis Contributions

This thesis explores the design, development, and evaluation of robots for in-bore needle insertion, focusing on developing and testing technologies that can ultimately fit into and improve the existing clinical workflow and resolve existing clinical challenges. We aim to accomplish this by developing a robot that can insert a needle into a patient with minimal hands-on effort from the physician while improving their ability to reach the target accurately. This resulted in creating a platform with a large workspace, high dexterity, and high accuracy with an automated control method for in-bore device setup and control.

In summary, the contributions of this thesis are as follows:

1. *Robot design for in-bore dexterity* – developed a low profile and redundant serial link robot design and controller, achieving clinically required accuracy, minimal in-bore footprint, dexterity to insert needles across a patient body, and a large active workspace.

2. *Mechanism for grasping a needle* - developed a solid-state clutching needle gripper that enables deep needle insertion with short axis length, simple manufacture and replacement, compatibility with different size needles, and functions as a passive guide when deactivated.

3. *Framework for in-bore planning and image-guided control of redundant robot* – developed clinically focused metrics for workspace and dexterity are utilized within a unified framework incorporating physician-specified task prioritizing for control of a redundant robot. Additionally, a method for utilizing CT image feedback for controlling a robot are presented. This framework enables fully hands-free device operation and is used for simulated design evaluation and control synthesis in-situ experiments.

4. *Method for robot design dexterity evaluation* - developed a design evaluation method for robotic systems dexterity during in-bore tool manipulation with retrospective motivating clinical cases and generalized synthetic cases across multiple patient body habitus. This

method can help improve robot design to maximize the possible needle insertion trajectories in patients, resulting in improved safety, ease of use, and a greater breadth of possible procedures with a single platform.

1.6 Dissertation Overview

This dissertation comprises five chapters. This first introductory chapter, *Chapter 1*, described the clinical problem, including an overview of related works and an overview of this dissertation. *Chapter 2* describes the development of our initial teleoperated robot for CT-guided needle insertion focused upon a specific procedure: needle lung biopsy. This chapter introduces our chosen kinematic and transmission design for minimal in-bore volume and backlash. Based on the lessons learned developing this system, a new platform was developed with a more broad focus: abdominal and thoracic CT guided needle insertion. This work is described in *Chapter 3*, covering the design and development of CRANE, a fully active system providing a low in-bore profile with a large workspace, high accuracy, and high dexterity and deep needle insertion. *Chapter 4* describes a method for automatic dexterous device setup and image-guided control. Finally, *Chapter 5* concludes this thesis with a summary of key results and contributions while presenting ideas for future directions.

Chapter 2

Low-profile Table-mounted Robot

Primary lung cancer is by far the leading cause of cancer death worldwide. When symptoms arise, the five-year lung cancer survival rate is 17% [Ame19]. Early lung cancer detection through screening with low-dose CT and needle biopsy has been shown to reduce mortality for high-risk patients. Definitive lung cancer diagnosis requires tissue sampling, often performed by percutaneous transthoracic CT-guided lung biopsy. Smaller lesions, especially those under 1cm in size, are challenging to target with current hand-guided methods [TWL+17].

During a needle lung biopsy, the radiologist must localize and target a pulmonary lesion several centimeters below the skin's surface. The radiologist moves a patient in and out of a CT scanner when alternating between viewing the position so f the needle and nodule on the CT scan in a separate room and manually advancing the needle. The non-real-time 3D scans and the freehand adjustments often result in the need for multiple punctures [HDBd+17] and restrict the angles at which the needle can confidently be advanced. This limits the radiologist's ability to reach lesions that require an atypical approach to avoid sensitive vessels or bone. Furthermore, repetitive CT scans have a significant risk of secondary imaging-induced cancer. Robotics can serve as a technological aid to significantly reduce these risks [KK15].

This chapter presents an the design of a teleoperated robot for intra-bore CT-guided lung

Figure 2.1: CT-guided robotic system with a low-intra-bore-profile serial-link redundant 7-DoF arm. A is the cartesian positioning stage. B is the trunnion and rotary axis. C is the robote 4DoF arm.

biopsies (Fig. 2.1). The robot uses a redundant serial linkage design that offers 7-DoF cable-driven control for minimal backlash and smooth positioning and inserting of biopsy needles. This robot significantly increases the number of approach vectors to peripheral targets. End-to-end development from mechanical design to full user interface was required to achieve both low in-bore profile and intuitive teleoperation.

Thus, we provide the following set of contributions:

1. Low-in-bore profile 7-DoF robotic biospy arm leveraging serial linkage design with outlined CT-compatible design considerations,

2. Zero-backlash, stiff transmission through the use of belt and cable drives as required for

high-fidelity teleoperation,

3. Intuitive teleoperational interface and control for direct image-guided intervention while the patient remains within the scanner bore,

4. Complete simulation environment in V-REP with full workspace analysis demonstrating reach, and

5. Fully open-source approach to engage the robotics community.

We present a description and analysis of the robot's mechanical design, characteristics, and capabilities. Furthermore, we verify the collision-free workspace through simulation, and perform experiments to determine the system's repeatability, teleoperated accuracy. In addition, a phantom biopsy procedure is performed under CT guidance.

The proposed robot will enable a radiologist to target a lung nodule, precisely adjust and align the needle's trajectory with the nodule, and biopsy the nodule. This will reduce the number of punctures and CT scans required for the procedure. However, given the large workspace and effective teleoperation of the robot, we also see a potential to use this platform for various intra-bore applications. Thus, by open-sourcing the platform, we aim to contribute a base platform solution to the surgical robotics community. Our design overcomes many coupled mechanical, electrical, user-interface, and systems engineering challenges. This reduces the barrier for other researchers in surgical robotics working toward 3D image-guided teleoperation or automation research.

2.1 Related Works

Robotic systems have been developed to address a range of image-guided needle biopsy applications ranging from liver ablation to prostate brachytherapy [KK15, MCS18]. Yet only

a select few have been designed to address the specific challenges of performing lung biopsy [SPB+02, AAP+15b, KSM+16, BDSR+18b, DJY+17, MSC15, ZTK+11].

Prior robotic approaches to lung biopsy can be broadly categorized by their physical approach to lesions, the number of active joints, their mechanical stiffness, and their controllers. Both platforms that use industrial robot arms and those with passive setup joints for transthoracic biopsy have a reduced number of feasible biopsy approach due to their limited reach into the bore due to their arm size [AKS+13, ZTK+11, AAP+15a] and limited active range of motion, respectively. They may be well suited for smaller anatomies with single approach vectors. Robotic systems using a device secured to the chest [WHS+07, SWH+09b, HBCF16c] have limited reach but may have better precision for positioning instruments as the body shifts.

Other robotic systems [SMH+17, KRS+11, vvDv15, SMR+15, RMK+11], including recently released commercial lung biopsy systems [Int19, Aur19], offer a bronchoscopic approach via intraluminal steerable needles [RUM18, FBS+17]. However, they have low diagnostic yield in peripheral lungs and for lesions smaller than 20mm [MNS12, GAO+14], [HKK+18, Aer16].

The success of these application-specific CT-compatible robotics systems illustrates the utility of CT-guided needle biopsy robots. However, due to the tight working conditions combined with stringent material limitations, existing robots have deficiencies in their operating area and reachable collision-free workspace. This precludes them from general-purpose applications. The proposed serial linkage robotic system overcomes several challenges by striking a balance between the high-stiffness industrial robot arm methods and the low-stiffness intra-bronchoscopic needle approaches.

2.2 Methods

This section describes the clinical requirements for lung biopsy and the considerations required for teleoperated robot design. This includes the mechanical design, the electrical

interfaces, kinematics, and user interface for teleoperation.

2.2.1 Clinical Requirements

Clinical requirements for lung biopsy includes the ability to hit 10mm biopsy targets with an average needle placement depth of 73mm (4.8-139.6 range) [WLH+14]. Commonly used needles range in length from 8cm to 30cm. The average human lungs are 25cm to 35cm in length and 10 to 15cm in width. Vasculature and ribs preclude certain approaches and other approaches are sub-optimal due to their high risk of heart and diaphragm puncture. This motivates a highly dexterous robot with a large working volume to enable access to target nodules from several orientations throughout the lungs without reconfiguration and manual setup. The robot must be radiolucent to minimize visual artifacts in the CT images.

Teleoperation enables direct "surgeon in-the-loop control". Humans naturally adjust for bias resulting from kinematic model inconsistencies with the real robot, as evidenced from the well-accepted teleoperation of the daVinci Surgical System for laparoscopic surgery (the robot uses a serial linkage approach). Furthermore, due to the radiologist's extensive training, they can compensate for needle deflections which occur due to tissue non-homogeneity and small initial placement errors. This places smooth and fine adjustability as a higher priority than pure kinematic accuracy and stiffness.

Furthermore, due to the closed bore CT scanner's 70cm bore and limited spThe kinematic structure of the platform is shown in Fig. 2.3. Kinematically and mechanically, the robot is composed of two distinct structure. The 3-DoF exo-bore stage is a linear-linear-roll belt driven positioning platform. Each actuator for this platform resides on the previous joint. The 4-DoF cable driven in-bore actuator is kinematically yaw-pitch-yaw-linear assembly. The four actuators for this assembly reside on a trunion which serves as the structure for the stage's rotary axis.

2.2.2 Linkage Design

Kinematically and mechanically, the robot is composed of two distinct structures. The 3-DoF exo-bore motion stage is a linear-linear-roll belt driven positioning platform. Each actuator for this platform resides on the previous link. The 4-DoF cable driven in-bore actuator is kinematically a yaw-pitch-yaw-translational assembly. The four actuators for this assembly reside on a trunnion which serves as the structure for the system's rotary axis.

For the serial cable driven joints, the number of idler pulleys increases with order N^2, where N is the number of joints. Therefore, it is beneficial to limit the number of serial cable driven joints required. This platform's 4-DoF cable driven intra-bore arm with the 3-DoF positioning stage provides a compromise between design complexity and system dexterity. This maximizes the platform's in-bore performance while minimizing its cross-sectional area. Mechanical benefits to using the serial cable driven design include:

- *Zero Backlash:* The use of cables with pulleys (in contrast with Bowden tubes) allows the arm to have zero backlash and high transparency which provides fine incremental motion. Additionally, there is no "stiction" which would interfere with fine adjustment.

- *High Load Bearing:* In contrast with belts, synthetic cables have high load bearing capabilities while still allowing flexible 3D routing and tolerating a small pulley diameter to cable diameter bending radius (D:d).

- *Improved Dexterity and Volume:* The serial link design contributes to the robot's high dexterity while minimizing its in-bore profile. Motors are placed out of the bore, where space is less constrained.

- *Reduced Mass:* The remote drive significantly decreases the arm's static loading, as each joint does not have to hold the following joints' actuators.

- *Improved Image Quality:* There is a significant reduction in imaging artifacts in comparison

with joint mounted actuators.

For needle placement, the combined 7-DoF design (including 1 needle advancement access) provides two redundant DoF (a needle is symmetric around its roll axis) which can be used for external collision avoidance via nullspace control.

A long carbon-fiber tube with the terminal 4-DoF cable driven end-effector reaches into the bore to place the dexterous end in the general working area. Carbon-fiber is both radiolucent (due to its low density) and possesses very high stiffness. The out-of-bore stage's two prismatic axes enable motion within the frontal plane. The revolute axis enables the trunnion to roll in the transverse plane.

Linear ball bearing rails with a belt drive are used for the stage's prismatic axis due to their high stiffness, accuracy, and low friction, and lack of backlash, respectively. Belt drives provide an excellent solution for backlash-free motion when space is less constrained, and the routing path is not tortuous. This decoupling of the intra-bore and exo-bore components enables our 7-DoF arm to have less than a 50mm$\times$50mm frontal cross section in the bore, increasing the use-able working space and decreasing the impingement upon the patient's area. Furthermore, image artifacts are virtually eliminated (see Fig. 2.9b) due to the few dense materials present in the bore. The design has 0.3m travels in both the robot's x-axis and y-axis.

Maxon RE339152 (24V, 10900 free RPM) motors connected to Maxon 370805 planetary gearbox (3.4Nm rated torque, 479:1 ratio) with US Digital E4T 500 count encoders on the motor shaft are used for all axis. This results in $3.7e-4$ degrees per count encoder resolution at the output shaft.

The robot end-effector is manufactured using a combination of Selective Light Activation 3D printing, continuous fiber reinforced Fused Deposition Modeling 3D printing, laser-cut acrylic plates, and turned pulleys. The robot base is constructed of plastics (Delrin, PTFE, Acrylic-like materials, nylon), composites (carbon and glass fiber composites), and minimal metallic components (steel bearings, rods, bolts).

2.2.3 Linkage Analysis

The up-to-10N loads applied when inserting and sampling a tissue during a lung biopsy result in elastic deformation of the robot's remote 4-DoF joint and cables, and may cause brinelling of the idler pulleys' bearings. Tested lung biopsy forces are measured below 4N, but, they may be as high as 8N [WHS+08b]. Assuming needle loading primarily acts as thrust load and torques applied to the needle, and consequently the insertion joint, are minor, the maximum joint torques for the three revolute joints on the 4-DoF arm can be bounded by:

$$\begin{aligned} \tau_{q_4} &= \max_x [sin(x)(0.16\text{m})(8\text{N})] \\ \tau_{q_5} &= \max_y [sin(y)(0.08\text{m})(8)\text{N})] \\ \tau_{q_6} &= 0 \end{aligned} \tag{2.1}$$

Therefore, the maximum applied load from the needle biopsy is 1.28Nm, 0.64Nm, and 0Nm for joints 4, 5, and 6 respectively.

The 4-DoF cable driven arm's idler pulley bearing load ratings primarily limits the robot's load tolerance. The R2-5 stainless steel bearings (McMaster Carr P/N 57155K347) have a static load rating of 177.8N. For the 4^{th}, 5^{th}, and 6^{th} joints, this corresponds to maximum joint torques at the lowest load rating configuration of greater than 2.49Nm, 1.25Nm, and 1.25Nm, respectively. Pulley force increases at higher deviations from straight for joints 5, 6, and 7. Joint 7 has a bearing limited force rating of 177.8N. Therefore, the arm has a sufficient load rating to perform a core needle biopsy. The gravity torques (≤ 0.011Nm) applied to joints of the cable driven arm are negligible compared to the torques due to needle insertion.

Cable stretch is, in general, a concern for precise control of serial linkage cable driven actuators. Disturbances due to cable stretch, unlike backlash, are linear. Nonetheless, it is still beneficial to minimize. The properties of several cable materials are summarized in Table 2.1. We

used Dyneema SK99 cable due to its ease of sourcing, high stiffness, low D:d ratio, acceptable creep, and UV resistance.

Table 2.1: Comparison of Cable Materials

Material	Tensile Modulus	Tensile Strength	D:d	Creep	Image Artifacts	Sourcing
SK99	155 GPa	4.1 GPa	5:1	Fair	Low	Easy
DM20	94 GPa	3.4 GPa	8:1	Great	Low	Difficult
Vectran	103 GPa	3 GPa	8:1	Good	Low	OK
SS	210 GPa	2 GPa	18:1	Great	High	Easy

The linkages themselves are made of 3D-printed carbon-fiber-reinforced plastic. Finite Element Analysis (FEA) simulation of the base joint (which observes the highest deflection) is presented in Fig. 2.2 using MarkForged's carbon fiber material properties. The FEA shows that the link deflection is negligible in comparison to the cable deflection.

To determine the worse-case deflection scenario, we consider a maximal deflection when the force is applied perpendicular to the outstretched arm (joint 4 with joint 5 straight). Due to negligible link deflection, the stiffness for this configuration is calculated as follows:

$$\Delta L = \frac{F L_0}{AE} \quad \text{and} \quad \Delta\theta = \frac{\Delta L}{2\pi r} \tag{2.2}$$

where ΔL, the change in cable length, is calculated using the definition of Young's Modulus, L_0 is the static length, F is the force applied to the cable, A is the cross-sectional area of the cable, and E is the cable's Young's Modulus. Using a first order approximation for tip deflection motion, this results in an end-effector stiffness of at least 1.55N/mm, or at most 0.64mm of movement for each 1N of additional force.

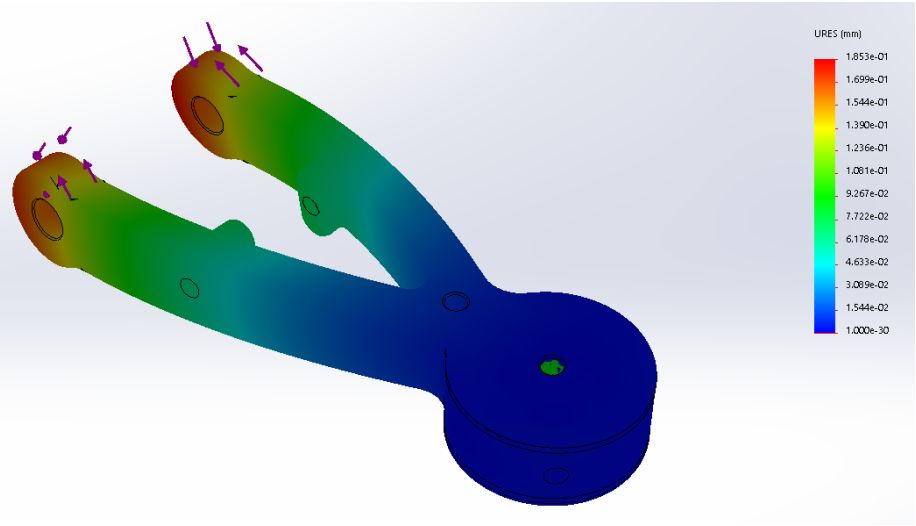

Figure 2.2: Finite Element Analysis deflection simulation with 2Nm applied torque for a single (base) linkage of the multi-linkage biopsy arm that extends into the bore.

2.2.4 Robot Kinematics

The kinematic structure of the platform is shown in Fig. 2.3. The robot's kinematic chain is described using Modified Denavit-Hartenberg (DH) parameter. The DH parameters define the pose of the next frame by origin

$$c_{n+1} = c_n + ax_n + dz_{n+1} \tag{2.3}$$

and orientation

$$R_{n+1} = R_n \begin{bmatrix} 1 & 0 & 0 \\ 0 & cos(\alpha) & -sin(\alpha) \\ 0 & sin(\alpha) & cos(\alpha) \end{bmatrix} \begin{bmatrix} cos(\theta) & -sin(\theta) & 0 \\ sin(\theta) & cos(\theta) & 0 \\ 0 & 0 & 1 \end{bmatrix} \tag{2.4}$$

where R_n is the n-th frame's orientation and c_n is the n-th frame's position. For this robot, $n \subset \{1,...,7\}$ is the robot's reference frame for the joints and $n = 8$ is the end-effector frame.

The modified DH parameters for this robot corresponding to the kinematic diagram presented in Fig. 2.3 and are provided in Table 2.2; the actuator-to-joint mixing matrix that converts unit steps in the actuator to unit steps in joint angles is presented in Table 2.3. In this table, q_i and m_i correspond to the i-th joint's configuration and actuator's configuration,

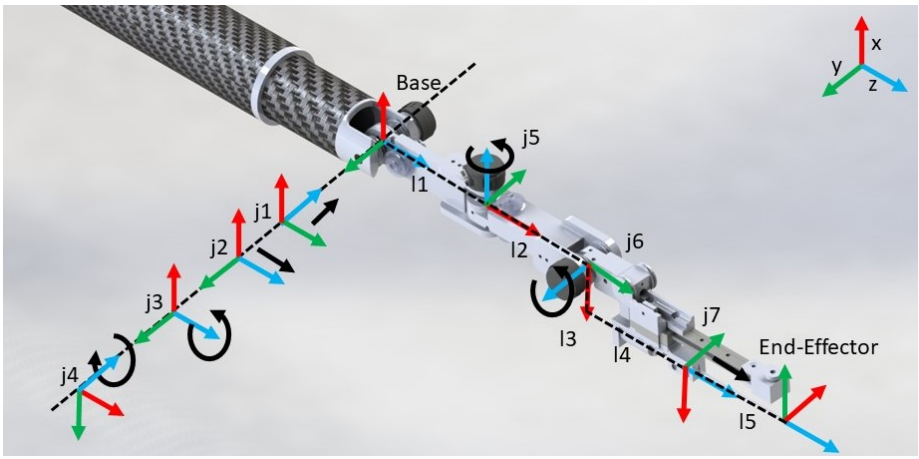

Figure 2.3: Kinematic diagram of the distal end of the robot, illustrating needle and base coordinate frames. A backend motion stage enables Cartesian positioning of the base joint.

respectively. The actuator-to-joint mixing matrix accounts for the pulley reductions of the 3-DoF stage's belt drives and joint coupling for 4-DoF cable-driven arm due to the varying amount of cable wrap as coupled joints move.

Table 2.2: DH parameters where p is prismatic and r is revolute. All angles and distances are in radians and meters, respectively.

Frame	Type	a_{i-1}	α	D_i	θ_i
1	p	0	$\frac{\pi}{2}$	q_1	0
2	p	0	$-\frac{\pi}{2}$	q_2	0
3	r	0	0	0	q_3
4	r	0	$\frac{\pi}{2}$	0	$q_4+\frac{\pi}{2}$
5	r	8e-2	$\frac{\pi}{2}$	0	q_5
6	r	8e-2	$\frac{\pi}{2}$	0	$q_6-\frac{\pi}{2}$
7	p	5.57e-2	$-\frac{\pi}{2}$	$2.74e-2+q_7$	0
8	-	0	0	1.15e-1	$\frac{\pi}{2}$

2.2.5 Embedded System Controller

Low-level motor control is performed using synchronized Proportional Integral Derivative (PID) controllers on a DE0 Nano SOC FPGA development board with a custom motor control PCB for 8-axis brushed DC motor control (MAX14870 driver IC) with current sensing (INA169

Table 2.3: Actuator-to-Joint mixing matrix, where p is revolute and r is prismatic.

Joint	Type	m_1	m_2	m_3	m_4	m_5	m_6	m_7
q_1	p	5.73e-3	0	0	0	0	0	0
q_2	p	0	5.73e-3	0	0	0	0	0
q_3	r	0	0	0.24	0	0	0	0
q_4	r	0	0	0	0.45	0	0	0
q_5	r	0	0	0	-0.35	0.45	0	0
q_6	r	0	0	0	0.94	-0.62	0.79	0
q_7	p	0	0	0	-5.26e-3	3.23e-3	-8.73e-3	6.35e-3

amplifier). The DE0 Nano SOC development board is a combination of a dual-core ARM Cortex A9 Hard Processor System (HPS) with a Cyclone V FPGA, interconnected through shared memory. Motors directly interface with the FPGA for encoder pulse counting, PWM generation, and current sensing. Additionally, a watchdog timer and emergency stop are implemented through the FPGA. High-frequency PID position motor control (1kHz loop rate) is implemented through the HPS and communicates with the FPGA using Direct Memory Access. The HPS hosts a TCP/IP web server to allow the remote master PC to update the motor position setpoints and disable/enable the robot. This physically separates the high-frequency, latency sensitive control from the low-frequency, high-level control.

2.2.6 User Interface

A kinematic simulation of the robot and collision simulation of the CT bore are developed using Coppelia Robotic's V-REP [RSF13a]. A Python backend communicates with the simulator, interfaces with various peripheral devices, and brings the physical robot system together such that the simulator matches with the physical robot and the peripheral devices can be utilized to control either the simulation alone or the synchronized simulator and robot. The 3DConnexion SpaceMouse is used as the input device to update Frame 6's position $p[n]$ and rotation matrix

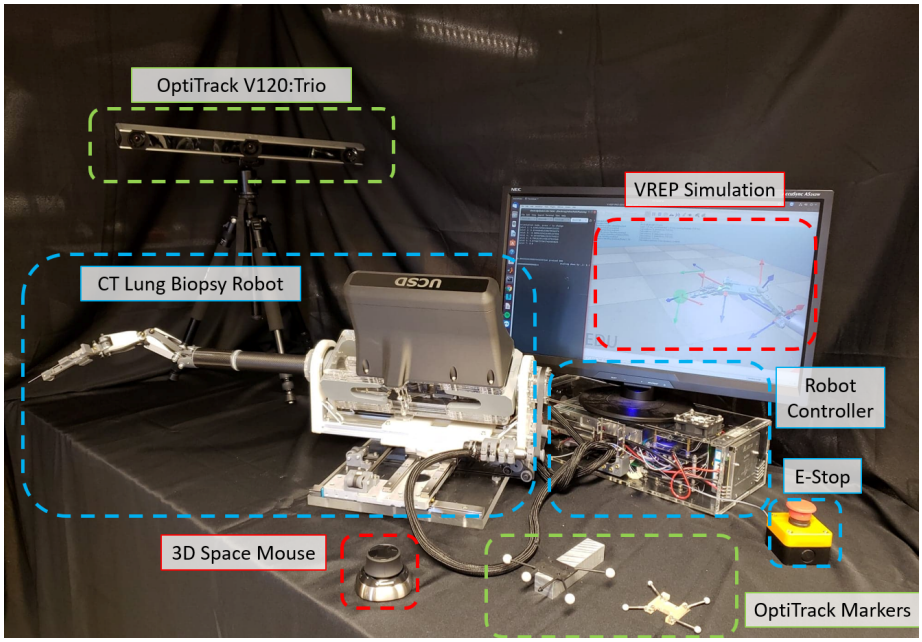

Figure 2.4: Experimental setup for the robot with Optitrack system and marker for benchtop tests (green box), robot and controller (blue box), and simulation with input device (red box).

$R[n]$ as follows:

$$p[n+1] = p[n] + \gamma v[n] \tag{2.5}$$

$$R[n+1] = \text{euler2mat}(\gamma \cdot r[n])R[n]. \tag{2.6}$$

$\gamma \in (0,1]$ is a velocity scaling constant which can be dynamically adjusted using two auxiliary buttons on the 3DConnexion mouse, $v[n] \in \mathbb{R}^3$ is a discretized linear force reading from the 3DConnexion mouse in the $[x,y,z]^T$ axis, and $\gamma \cdot r[n] \in \mathbb{R}^3$ is an γ-scaled and discretized rotational velocity reading from the 3DConnexion mouse around $[roll, pitch, yaw]^T$ axis and converted into a rotation matrix via euler2mat$(\cdot)$. Inverse kinematics is calculated using a damped-least-squares method, available through V-REP, to solve for the joint configuration. This discrete time system is sampled at 400Hz. The final joint, needle insertion, is advanced and retracted using the control computer's keyboard in 0.1mm increments.

For visual feedback, the radiologist who is teleoperating the robot, views the CT images

on the computer present in the standard imaging suite for CT scanners. Additionally, a 1.6mm diameter video endoscope (Misumi MD-V1001L-120) is mounted parallel to the needle, and is displayed to the user to provide a first-person needle insertion view.

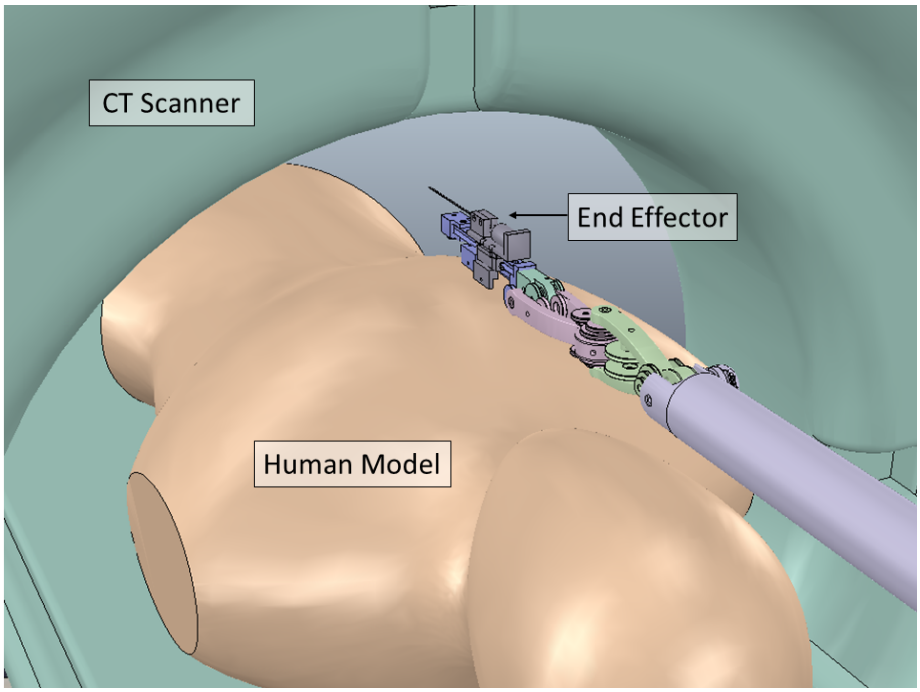

Figure 2.5: V-REP simulation environment shows the working space afforded by the serial linkage design that extends into the bore.

2.3 Experiments

Experiments were conducted to show the performance and effectiveness of the system. Through simulation, the large reachable workspace on a human model in a CT bore is shown. A repeatability test is conducted to measure the precision of the system. Finally, the effectiveness of the system's teleoperational control is shown through a repeated needle targeting experiment and a in CT bore biopsy puncture of a phantom lung. The hardware test setup for the lab experiments are shown in Fig. 2.4. Due to limited parts on hand, the platform used in the hardware tests had shorter translational stage travels.

The following section describes experiments conducted to validate the system. The motivation is to evaluate the robot for needle biopsies which generally require high precision, and with closing-the-loop through a human teleoperator for accuracy in targeting lesions. Here we explore the workspace reach, precision and repeatability tests on benchtop target tests, and finally intra-CT bore biopsy sets using a phantom. The hardware test setup is shown in Fig. 2.4.

2.3.1 Collision-free workspace

V-REP was used to evaluate the collision-free workspace of the robot design. A virtual environment with a 65cm CT bore, a human adult dummy, and the robot are built as shown in Fig. 2.5. Over one million ($N = 1.77e6$) joint configurations for the first six joints were evaluated to determine the reachable collision-free work-space afforded by the robot's in-bore kinematic design with a cartesian positioning base stage. The final insertion joint is excluded since it is used for needle insertion once reaching the target pose. The end-effector pose, and the overall robot's collision state (either self or environmental) are recorded for each point. In-collision points are removed. End-effector poses within a 5mm radius of each vertex of the Polygon File Format (.PLY file) robot model of the dummy are binned and counted. The percentage of the populated cell are translated to the plots shown in Fig. 2.6. Manual analysis of the lung region, which resides in the dark red region of Fig. 2.6 further highlights the dexterity of the robot. The two cones represent two extremes of the reachable workspace.

2.3.2 Precision

We tested system precision through a repeatability test. This illustrates the system's mechanical repeatability and tolerances. The robot repeated a sequence of 64 unique end-effector points, equally spaced through the robot's joint space, five times. At each point, the pose of the end-effector is recorded using an OptiTrack V120-Trio. The l2 deviation from the mean position

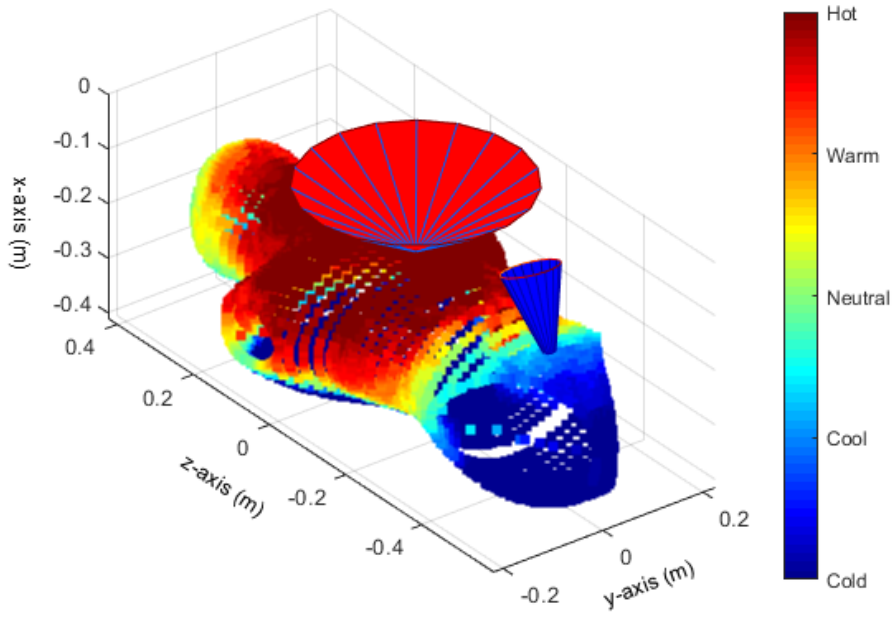

Figure 2.6: Heat map of the reachable workspace on an adult human in a CT bore. Hotter colors corresponds to higher dexterity. The cones show the angles of needle insertion possible for the example vertices.

and orientation (roll, pitch, yaw) for every configuration results in a standard deviation of 2.43mm and 2.95 degrees for position and orientation respectively. The contributed video illustrates this test.

2.3.3 Teleoperated Accuracy

Using the needle and visual feedback from the endoscopic camera, the operator controls the robot to puncture 16 bull's eyes on a four by four grid. The punctured paper target was scanned, and puncture distance from the bull's eye center is measured using the measuring tool within the GNU Image Manipulation Program [Gim19]. The target is shown in Fig. 2.7. The mean positional error from the center of the bull's eye is 0.73mm with a standard deviation of 0.30mm.

2.3.4 Teleoperated CT-guided Needle Insertion

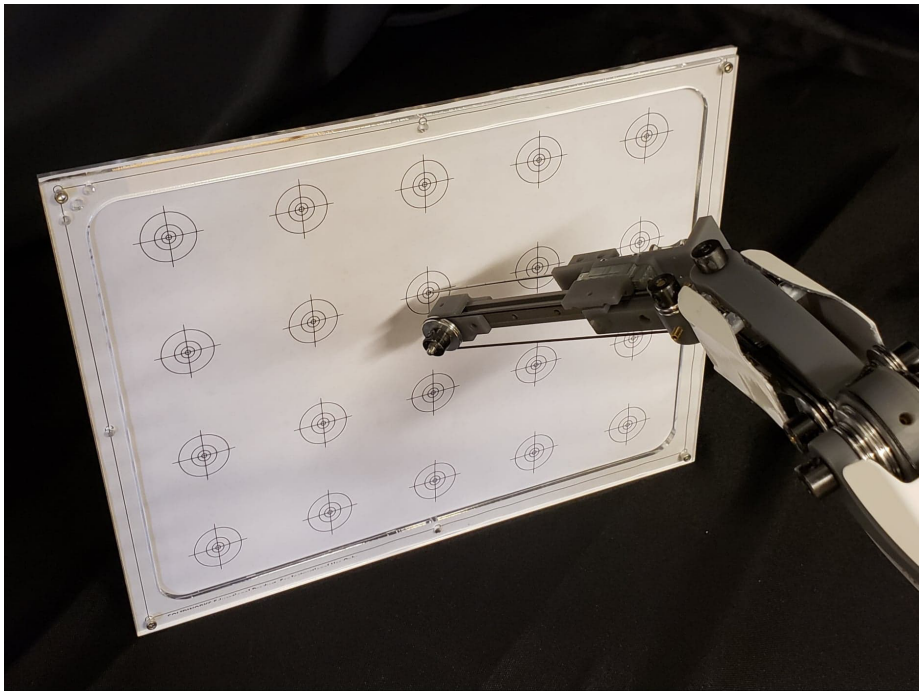

Figure 2.7: Test set up for the paper puncture target tests to verify teleoperational accuracy.

The biopsy task was conducted inside a sliding stage CT scanner (GE 750HD) at the University of California San Diego's Thornton Hospital. Scan settings of 120 kVp, 40 mAs per slice, 0.4-second rotation time and a $CTDI_{vol}$ of 0.89 (similar to numbers reported in [TTC^{+}09]) were used. Testing was performed on a custom lung phantom, based on the design presented in [SK92a]. The lung phantom consisted of a 7.25" $\times$ 5.25" $\times$ 2" synthetic foam sponge placed inside a sheet-aluminum ribcage. Two nodules were emulated with 1cm diameter clay balls and placed into the sponge. Targets were marked on top of the sponge to give rough position estimates for the nodules. Agar was cast in place over the ribcage and sponge. The entire lung phantom is held inside a 12" $\times$ 12.5" $\times$ 6" acrylic box.

An experienced radiologist teleoperated the robot using the 3DConnexion SpaceMouse to the target point (Fig. 2.8).For visual feedback, a combination of CT image data, an external webcam viewing the robot, the needle mounted endoscopic camera (Fig. 2.8), and the kinematic

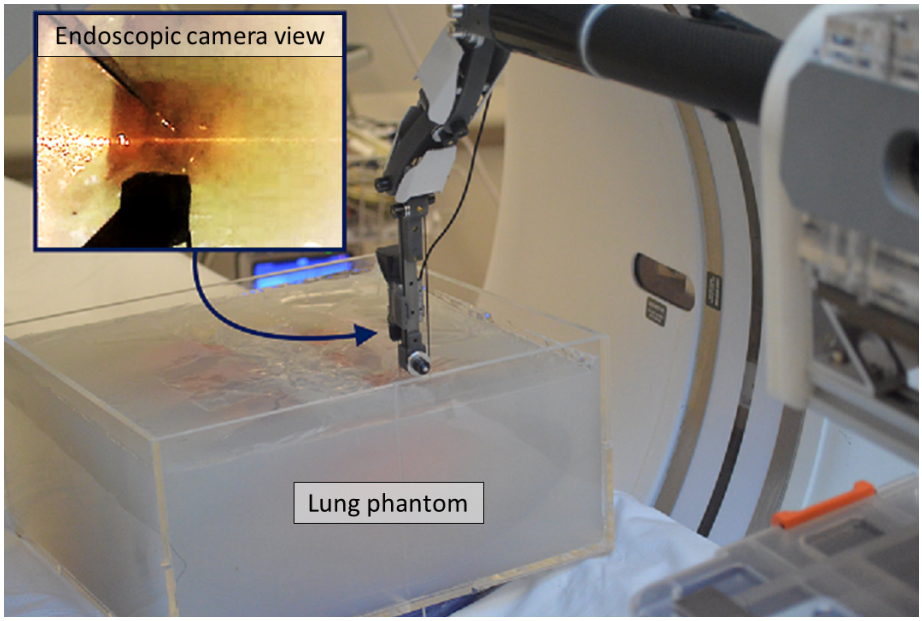

Figure 2.8: Photo showing a biopsy task where the robot was operated by a radiologist. The endoscopic camera view (inset) gives an additional perspective for the radiologist to ensure a precise needle insertion.

rendering provided in V-REP were used. Both targets were successfully reached on the first puncture attempt. The contributed video illustrates this test.

2.3.5 CT Image Interference

CT scans were performed to check for artifacts in the CT images due to metal in the end-effector. Sample images are shown in Fig. 2.9a and 2.9b where the needle was positioned vertically to show it on an transverse slice, showing no significant artifacts coming from the

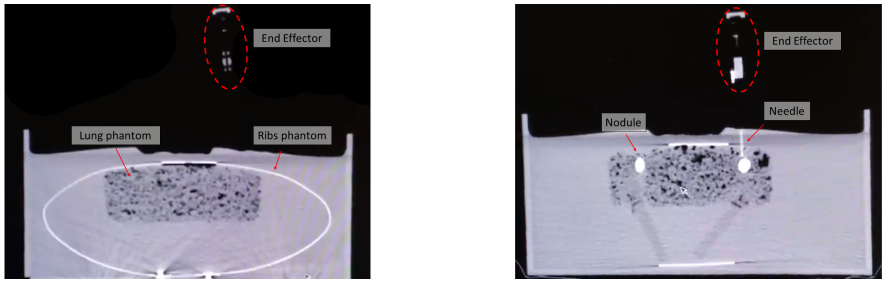

(a) (b)

Figure 2.9: CT scans from the teleoperated experiment. In (a), the phantom where the ribs and lungs are made from aluminum and sponge, respectively. In (b), the approach towards a needle biopsy of a nodule inside the phantom lung. (a) and (b) were taken at different z-depths.

robotic system.

2.4 Discussion

This chapter presents a teleoperated 7-DoF, low-profile, and highly dexterous robotic needle placement platform for efficient and accurate needle biopsy of the lungs. The kinematic, transmission and mechatronics designs are the basis for our future system.

Through cable and belt drives, backlash is minimized. The system is designed with the flexibility and intra-bore compactness such that not only lung procedures can be performed, but most other image-guided interventional procedures may find it useful. Simulation of the platform's collision-free workspace illustrated full access to the lungs from multiple orientations, repeatability with a standard deviation of less than 2.5mm and 3 degrees, and minimal shadowing and artifacts in the CT scanner. Under teleoperation, where the human closed-the-loop, mean position error of less than 0.75mm was achieved. Finally, the system is provided fully open-source to reduce the considerable development time for other researchers to engage in CT-guided robot biopsy research. Complete and detailed mechanical analysis, electrical design, user interface and systems design are available at `https://github.com/ucsdarclab/Open-Source-CT-Biopsy-Robot`.

While the kinematic design promises excellent dexterity and the cable-driven design has low backlash, the existing design has several limitations. Mechanically, the lack of a Z-axis requires manual adjustment of the device's setup height relative to the phantom. Additionally, the in-bore rotary joint's cable routing limits significant angulation adjustments. The short needle insertion axis defines the maximum depth for needle insertion. However, a more extended depth with a dedicated insertion axis would limit space within the imaging bore. This limits needle insertion accuracy. The existing actuators have a high gear ratio resulting in high reflected inertia and a non-backdriveable system, resulting in difficult device removal in the case of failure and low maximum speed. Finally, accuracy and stiffness at the tip are relatively low due to the lack of

end-effector and joint sensing and control.

The next chapter presents an improved device design and controller to address these limitations. A Z-axis is included to improve device setup and control. Cable routing is optimized for greater in-bore joint travel ranges and design dexterity. A novel needle gripper is developed to enable deep needle insertions with a limited travel insertion axis. Additionally, low gear ratio motors and passive gravity counterbalance supports a highly dynamic system that is passively safe, easy to set up, and manually removable in the case of failure. Finally, joint and end-effector position sensors are included in the hardware design and used for multi-level closed-loop control, providing high accuracy.

2.5 Acknowledgments

Chapter 2 is, in-part, a reprint of material from D. Schreiber, D. Shak, A. Norbash, M. Yip, "An Open-Source 7-Axis, Robotic Platform to Enable Dexterous Procedures within CT Scanners," in 2019 IEEE/RSJ International Conference on Intelligent Robots and Systems (IROS). The dissertation author is the primary author of this paper.

Chapter 3

Large-workspace Dexterous Robot

Within the field of Image Guided Surgery, Intraoperative CT guidance is used to guide the physician to both diagnose and treat numerous diseases, primarily where there are complex 3D anatomical constraints and small, deep, target nodules that reside typically 10 cm or more below the surface of the skin [TTC+09, RACF+18]. Three of the procedures most frequently treated via this approach are biopsies and ablations of lung, liver, and kidney tumors: all in the abdominal area.

During an intraoperative CT-guided procedure, the physician must localize and successfully insert a needle-like probe into a target. Typically, the physician alternates between advancing the needle a fractional distance to the target, stepping away, and scanning the patient to receive an update on the needle and tumor's position. When advancing the needle, the patient is withdrawn from the scanner bore to allow the physician to place the needle ergonomically. The combination of the non-real-time nature of CT scans, the lack of tool tracking, and the freehand adjustments result in the physician needing to cognitively visualize the 3D trajectory and estimate the amount of fine needle adjustment required to hit the target, all without visual feedback. This results in an increased number of scans needed to hit the target precisely, greater variability in and lengthier procedure times, and a potentially need to withdraw and re-insert the needle. These factors result

in decreased safety with clinically relevant side effects [HDBd$^+$17, AWB$^+$15], decreased positive predictive value [WJTT16] and increased radiation dose [Tea13]. Furthermore, small, deep lesions are especially difficult to reach as slight angulation errors result in significant tip positioning errors [TWL$^+$17]. Robotics offers a potential solution to these issues by providing increased accuracy for needle trajectories and removing the tedious back-and-forth procedure flow, allowing physicians to precisely insert the percutaneous devices along more cranial-caudal trajectories rather than the in-plane trajectories currently selected [KK15]. Existing robotic platforms have dexterity, workspace, accuracy, device setup, or instrument compatibility limitations.

This chapter introduces the CT Robot and Needle Emplacer, CRANE (Fig. 3.1), a needle-manipulation system design providing dexterity, workspace, and accuracy within an imaging bore of a scanner. CRANE's novel design demonstrates a fully active, serially linked, redundant kinematic approach with closed-loop tip pose control with a new needle-grasper which allows for large dexterity within imaging bores with high accuracy while accommodating insertion and retraction of a variety of needle-like surgical tools.

We provide the following technical contributions:

1. Low profile, redundant, and dynamic serial link design with high dexterity and actuator bandwidth.

2. High tip accuracy achieved through multi-level control to compensate for errors in individual system components. An analysis of errors is presented.

3. Development of a novel disposable and sterilizable clutching needle driver using an SMA actuator providing a simple needle grasping mechanism.

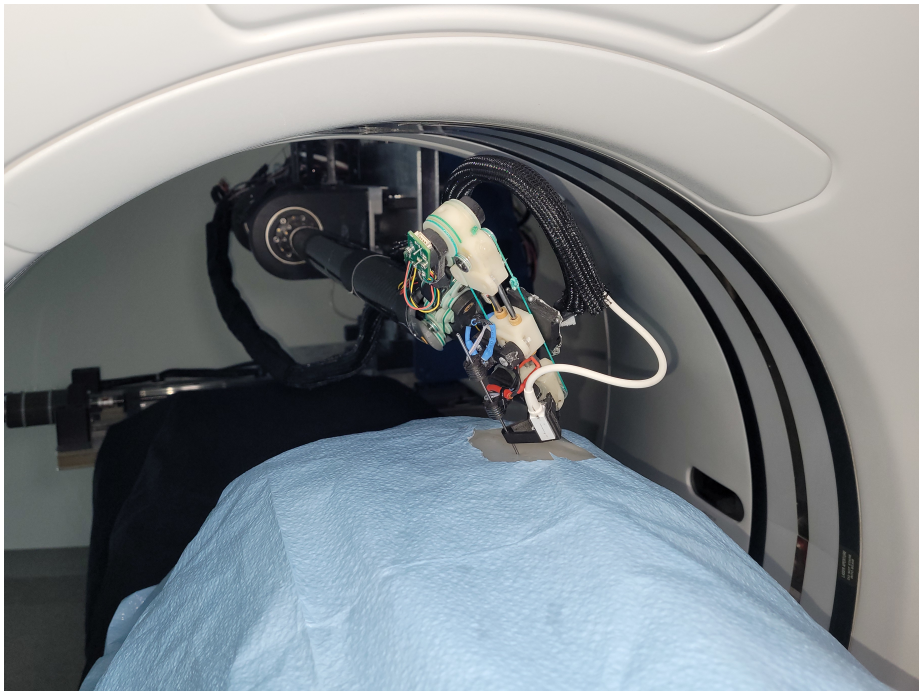

Figure 3.1: Needle insertion within imaging bores provides direct volumetric visualization of the anatomy and tool, improving the accuracy of needle insertion procedures such as retroperitoneal biopsy and lumbosacral spine nerve block. However, this enclosed environment limits the space for manipulation and line-of-site visibility for devices. CRANE overcomes these challenges with its cable-driven serial link design and integrated planning-control method to enable fully in-bore dexterous needle manipulation without requiring manual setup.

3.1 Related Works

Needle insertion robotic platforms for use within imaging bores have been developed for a wide range of applications across the human body, ranging from leg-bone biopsy to brain surgery. Of these applications and platforms, this overview focuses on systems applied to the torso and chest region, frequently the most restrictive of anatomy with regards to in-bore space as patient chest and abdomens are the largest area of the anatomy. Additionally, procedures performed within this region have a large number of anatomical obstacles, including the rib cage and large blood vessels, and face significant anatomical motion due to lung motion, large blood vessel pulsating, and the digestive system.

Needle insertion platforms for use around patient torsos within imaging bores can be broadly grouped into two clusters based on if they are mounted to the patient or mounted to the

floor and scanner bed. Within each of these categories, systems can be fully active or rely on passive setup and joints.

Patient-mounted systems are typically smaller, and under-actuated [WHS+08a,GMGH+18b, HKM+17, MBG+06, YJY+17, WLP+19b]; however, a select few are fully actuated [BZJ+08b, HBCF16c, xac]. These systems naturally move with the patient, which provides benefits through inherent system motion with patient respiration. Bore mounted systems [SWA+98, KFP+, SES+, SCD+97, MFP+01b] with passive setup joints or a mixture of passive and active joints provide a compromise between the challenges of patient setup while maintaining a fairly low bore profile and retaining high system stiffness. However, they have limited ability to compensate for gross patient motion due to pain or coughing and target motion within the body due to physiological motion. Additionally, for both patient-mounted systems and those utilizing passive setup joints, the manual positioning and attachment to the patient or manual understanding and positioning of the setup joint can be challenging, add time and complexity to a procedure, and preclude certain superior needle insertion trajectories if a setup pose can not be found.

Fully active systems (either floor [YWQ+10, HKM+17, TATPO+11b, KKF+04, FDP+02, JWNKGBKJBSHK17] or table mounted [MvK+17, SHOM15b, SCP+03b, MGR+08b, FIS+21, BZJ+08b]) provide numerous advantages, both in resolving the aforementioned issues (decreased setup complexity, ability to regulate tip stiffness decreasing tissue damage due to respiratory motion) with patient-mounted systems and those utilizing passive setup joints and beyond, including the ability to minimize physical contact with the patient decreasing a rising concern with the COVID-19 pandemic. Systems using large industrial arms with a custom end-effector [TATPO+11b] provide high stiffness at the cost of a larger system size with less intra-bore dexterity and workspace available and limited ability to remove the system in case of a system failure manually. These systems operate outside the bore rather than within due to space considerations.

These aforementioned systems use a variety of methods of interacting with the needle,

ranging from passive needle guides [SWA+98, KFP+, KKF+04, SES+, SWA+98, MFP+01b, FDP+02, SCP+03b, MGR+08b, BZJ+08b] to a variety of active mechanisms including fixed travel insertion [YWQ+10, SKD+08b, SSNY19], rollers [SPB+02], clutches [FIS+21, FKP+20], graspers [GMGH+18b], and one-time use gear-wrapper guides [xac]. These designs have limitations in their compatibility with needles and probes, high complexity, potentially challenging sterilization procedures, and have demonstrated damage to fragile ablation probes [SPB+02]. A fully active and low-profile system presented in [SSNY19] demonstrated large workspace, high dexterity, and high physician-in-loop accuracy. This design focused on moving actuators outside of the bore via a cable-drive transmission coupled into the scanner via a thin carbon-fiber tube. However, due to the long kinematic chains, long travels of cable-driven joints with numerous pulleys, and lack of joint and tip sensing, robot state estimation and system accuracy are low. Additionally, the joint ranges are limited due to non-optimal cable routing, and the maximum active needle insertion depth is only 50mm.

CRANE supersedes this design with an entirely re-engineered system which greatly increases the workspace by adding a vertical axis, optimized cable routing providing over 40% higher cable-driven joint travels, and unlimited needle insertion length via a clutching needle grasper. These previous travel and insertion length values were limited upon physician-user evaluation. Furthermore, this new system provides high end-effector accuracy through multi-loop controllers and multi-level joint and end-effector sensors and improves safety.

3.2 Methods

The CRANE platform design focuses on dexterity, accuracy, and safety through its fully active design with precise transmissions, redundant sensors, and a fail-passive design (illustrated in Fig. 3.2 and with system specifications in Table. 3.1). In the following sections, we will describe the analysis and modeling of the mechanics of the design, as well as supporting electrical

and software system architecture.

Table 3.1: CRANE's design specifications highlighting the dexterity, accuracy, and safety

Specifications	Category	Values
Degree of Freedom	Positioning Joints	8 Dof
	Needle Gripper	2 Dof
Needle Insertion Mechanism	Length	180mm
Accuracy	Positional	$< 1mm$
	Angular	$< 1^{\circ}$
Communication	Embedded	UDP
	Desktop	TCP/IP
Sensing	Motors	Opt. encoder
	In-bore joints	Magn. encoder
	End effector	Magn. tracker
Sensor resolution	Opt. encoder	$< 0.01^{\circ}$
	Magn. encoder	$< 0.1^{\circ}$
	Magn. tracker	$< 0.1mm$
Backdriving force	Needle	$< 1.0N$
	Trunnion joint	$< 0.91Nm$
	In-bore joints	$< 0.35Nm$
	Linear joints	$< 60N$

3.2.1 Clinical Requirements

CT-compatible biopsy robots need to follow certain clinical requirements, guiding the design of these systems:

- *Forces*: a maximum of 10N needle insertion force with 0.06Nm torques to adjust needle orientation while moving through tissue [PSV^{+}16, Wal10, WHS^{+}08a]. This requirement is achieved through the use of a rigid base structure, high strength plastic in-bore joints with high strength synthetic cables and a strong needle grasping mechanism.

- *Workspace*: the system should be able to insert needles across the human body in different

configurations without colliding with the patient's body or the scanner bore. This requirement is achieved by having low profile in-bore components for the system with large travels outside the bore. This design significantly improves robot dexterity over previous robotic systems [SSNY19].

- *Precision*: Abdominal needle insertion procedures typically require $< 2mm$ position and $< 2^{\circ}$ angular accuracy. Here, this requirement is achieved through a low-backlash transmission with joint level encoders, closed loop end-effector control, and validated via trajectory tracking tests.

- *Needle Interface*: Physicians use a variety of needle-like probes during their practice, and these needles should be quick to attache and remove. This requirement is achieved through a novel, disposable, removable, and sterilizable mechanical needle interface using helically wrapped Shape Memory Alloy actuators

- *Image Artifacts*: the system should not cause major imaging artifacts. This is achieved through the use of plastics, composites, and ceramics in the bore with minimal use of high-density materials within the scanning area.

3.2.2 Mechanical Design and Analysis

Needle insertion requires manipulation with three Cartesian position constraints and two Cartesian orientation constraints (excluding roll around the needle's primary axis). Therefore, the device must have at least 5 degrees of freedom (DoF). Additionally, the robot's joints and links must avoid obstacles (e.g., scanner gantry, patient, self-collision) while inserting and manipulating the needle. In total, CRANE has 8-actuated joints for a 5-DoF problem space with three redundant joints. This enables CRANE to reach around the patient's body to insert a needle while avoiding collisions and singularities.

The mechanical design maximizes in-bore dexterity and active workspace while retaining a low profile with a smooth and low backlash transmission. The system accomplishes this by splitting the mechanics into two subsystems shown in Fig. 3.2: a large workspace out-of-bore base and a small intra-bore end-effector. The gross positioning stage is active, resides outside the scanner bore, and provides large-scale linear motion enabling automated device setup. The end-effector provides orientation control and final needle insertion within the tightly constrained space between the scanner bore and patient. Highly efficient transmissions with low gear-ratio motors enable precise motion and backdriveability. The in-bore joints are cable driven for a low profile within the scanner driven by remote low gear-ratio low-backlash coreless motors outside the bore.

Gross Positioning Stage

The gross positioning stage comprises serially linked linear stages providing X-Y-Z cartesian motion with a large workspace (400*mm* in each axis), high precision, low friction, and low inertia with constant-force spring for Z-axis gravity compensation. The linear stages utilize ballscrews (Misumi BSST1204 with 4mm pitch, Misumi C-BSS1210 with 10mm pitch), coreless motors (Maxon 2260.886-51.216-200) with high-resolution encoders (US Digital E5-5000), and recirculating ball linear rails (Misumi SSXW33) with a composite foam-aluminum sandwich structure providing high stiffness and damping. The gross positioning stage's Z-axis (joint 2) is gravity counterbalanced via constant force springs (McMaster 9293K69). The first three joints can achieve linear velocities of 0.166 m/s, 0.166 m/s, and 0.332 m/s, respectively. Stiffness and backlash are measured at $>$ 100N/mm and $<$ 0.1mm using a dial indicator (Shars, 0.0005") and Z-style load cell (500N range). These values far out-perform clinical requirements for target procedures. Therefore, the base motion stage is neglected from the system stiffness analysis.

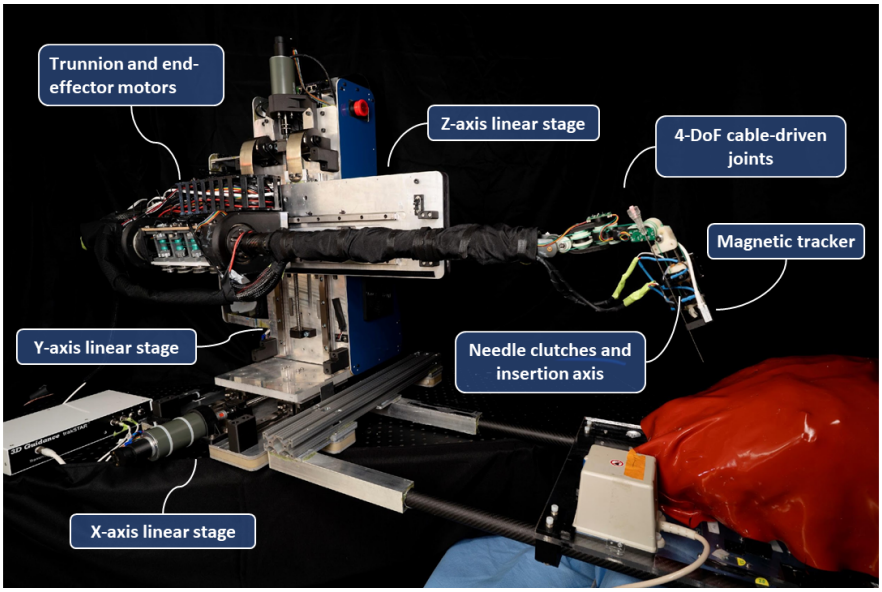

Figure 3.2: Experimental setup for bench-top system evaluation, highlighting the robot platform: the gross positioning stage enables the platform's large workspace and houses the actuators for the in-bore joints, and the redundant cable-driven in-bore joints enable orientation control and reaching around obstacles. The clutching needle insertion axis allows deep needle insertion with a short robot stroke. Together, this provides CRANE with a large workspace and the capability to perform dynamic motions while remaining backdriveable and having a minimal in-bore cross-section.

End-effector

The distal end-effector enables dexterous needle manipulation within the tightly constrained space between the scanner bore and the patient. The end-effector has 5-DoF: 4 revolute joints for orientation control and a final needle insertion mechanism (described below) with a prismatic joint. $2N$ cable transmissions couple the proximally located motors to the distal 4-DoF in-bore joints through a thin tube. The 4-DoF in-bore joints comprise three revolute joints and the prismatic needle insertion joints. Through a series of cable-driven joints, the motor volume and weight for the last DoF are isolated from the joints themselves, enabling a more compact design and thus greater workspace coverage, while low-gear-ratio motors can then be used to provide low reflected inertia to enhance backdriveability. The motors for the in-bore joints of the end-effector are housed within a rotating trunnion. The trunnion provides the end-effector's 5th-DoF and is actuated via a belt drive coupling with a hollow shaft for electrical wire pass-through. Idler pulleys (Fig. 3.5) are placed coaxially with actuated joints to reroute cables to further distal actuated joints

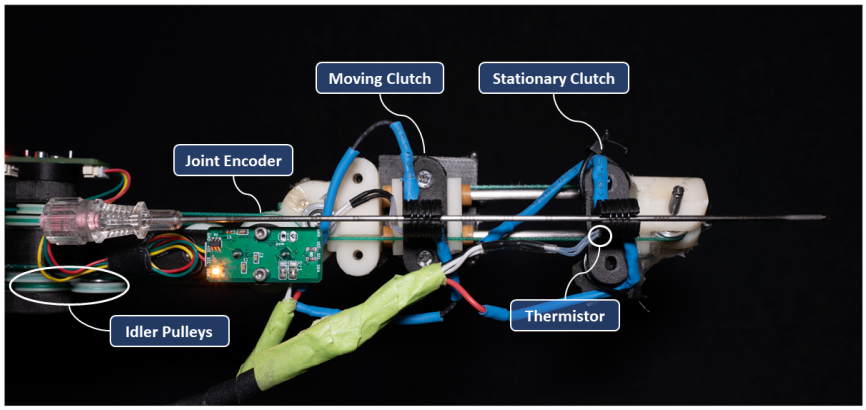

Figure 3.3: The robot end-effector is cable-driven. While cable drives provide low hysteresis and friction, they have limited stiffness, resulting in tracking errors. Joint mounted encoders enable direct sensing of the joints' position allowing controller compensation for cable stretch. The SMA actuated clutches temperature is sensed via thermistor, enabling closed-loop temperature control. The two moving and station clutches enable long travel active insertion or passive needle insertion with a simple and fail-passive mechanism which can be easily replaced for sterility and different size tools.

to maintain pulley-cable contact and minimize cable loop length change throughout the joint range. Gravity torques are minimal ($\sim 0.01Nm$) due to the link's low masses. Fiber reinforced plastics and synthetic cables are utilized for the in-bore components to minimize deflection and artifacts in the scanner images.

The joints are manufactured with Carbon Fiber Reinforced Plastic, ZrO_2 ceramic bearings, bushings, 1.25mm diameter Dyneema SK99 synthetic cables, and minimal metallic components to prevent imaging artifacts. Through optimized cable routing, including decreased pulley-to-pulley clearances and improved pulley positioning, the cable-driven revolute joint travels reach 200 degrees and are limited by self-collision with neighboring links. Capstan drive pulleys are connected to a 44:1 geared Maxon motors via GT2 timing belts with a final drive reduction of 219.7:1. The capstan to joint drive ratio reduction is 2.27:1, providing a final drive line reduction of 219.7:1 and resulting in a maximum independent joint velocity of $5.16\text{rad}/s$. Such velocity greatly exceeding the requirement for a needle manipulation robot to compensate for anatomical motion; the 3.36N/m joint torque provides sufficient end-effector force in all configurations.

Needle Insertion Mechanism

Humans perform needle insertion stepwise, iteratively performing short insertions and grasping the needle. On CRANE, the needle insertion mechanism mechanically imitates this insertion strategy. The needle linear-insertion joint's length is short to allow operation in tight space between the scanner bore and patient who has large body habitus. Although the insertion joint's length is shorter, the maximum needle insertion length is increased from the addition of a novel needle insertion clutching mechanism. Together, this enables deep insertion within a constrained space. The needle insertion mechanism includes the cable-driven prismatic insertion axis, two-needle grippers, and a guide bushing for precise long-travel needle insertion with a limited travel prismatic axis. The two-needle grippers (Fig. 3.3) are placed coaxially within the needle insertion mechanism. One functions as a stationary brake to prevent needle motion, and the other on the final prismatic needle insertion link. The guide bushing additionally serves as a mount for the Ascension trakSTAR magnetic tracker and the CT alignment marker used for end-effector pose sensing (described in Sect. 4.1.1).

The needle grippers use a Shape Memory Alloy (SMA) wire helically wrapped around a flexure and actuated via Joule heating. Temperature is measured with a thermistor bonded in place with thermal-epoxy in direct contact with the SMA wire for clutching status. When room temperature, the gripper is deactivated and acts as a guide. When heated, the wire contracts due to a crystalline structure change in the Nitinol from Martensite to Austenite. This length change applies a compressing the flexure into the needle. Experiments for measurements of slipping force, activation and cooling times, and lifespan were empirically tested (discussed in Sect. 3.3.1).

Statics Analysis

Because of the long and thin arm section required to reach the patient within the scanner bore, stiffness analysis is performed. The EE's links are constructed from carbon fiber reinforced plastic (CFRP). FEA analysis, illustrated in Fig. 3.4, shows $K_{\text{link}} = 2.77N/mm$ of tip deflection

due to link deflection in a nominal configuration and a minimum $2\times$ factor of safety for all links. This configuration is used for both linkage and transmission analysis due to maximal loading, both for the links and the cable transmission, with minimal passive joint loading.

Additionally, the cable transmission for the in-bore joints can exhibit deflection due to external forces and internal non-idealities, including friction, creep, and hysteresis. Static cable stretch is evaluated to determine its effect on system accuracy and stiffness. Cable stretch [Miy17] can be modeled as:

$$\Delta L = \frac{F L_0}{AE} \tag{3.1}$$

where ΔL is the cable length change, E is the cable's Young's Modulus, L_0 is the cable's nominal length, F applied force to the cable, and A is the cable's cross-sectional area. From this, angular deflection on cable-driven revolute joints can be calculated as:

$$\Delta\theta = \frac{\Delta L}{2\pi r} \tag{3.2}$$

where $\Delta\theta$ is the joint angle change due to cable stretch and r is the terminating capstan pulley's diameter. Transmission deflection due to cable-stretch results in $K_{\text{cable}} = 1.55N/mm$ end-effector stiffness when evaluated at the configuration shown in Fig. 3.4.

Modeling these two components as series springs, the combined system stiffness at the given configuration is:

$$K_{\text{system}} = \frac{K_{\text{linkage}} K_{\text{cable}}}{K_{\text{linkage}} + K_{\text{cable}}} = 0.99N/mm \tag{3.3}$$

The end-effector deflection resulting from linkage and transmission deflection due to needle insertion forces motivate the addition of sensors to directly track robot end-effector and joint state. Magnetic tracking of the end-effector enables the detection of link deflection, and joint-mounted magnetic encoders enable the detection of true joint position despite cable stretch. Feedback controllers (described in Sect. 3.2.5) are applied to compensate for these errors.

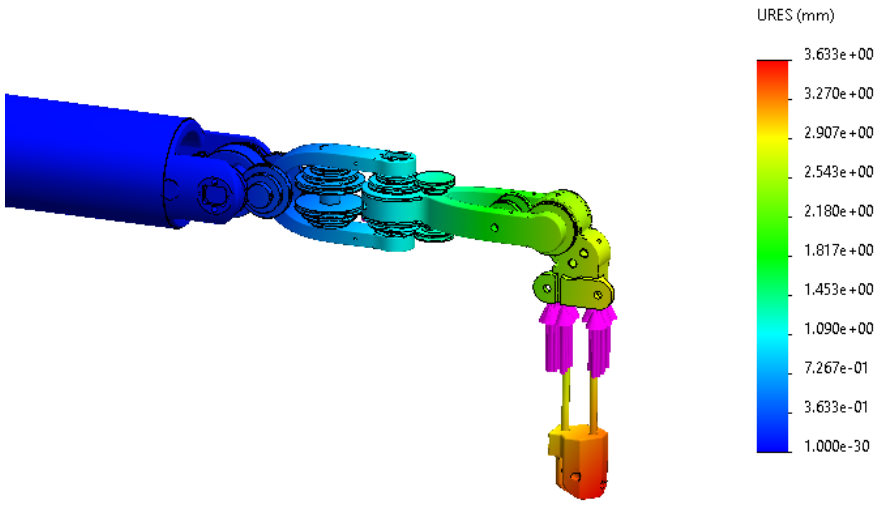

Figure 3.4: The long cantilevered tube for in-bore joints causes deflection illustrated by FEA modeling. This error, not observed by the joint encoders, is tracked and compensated for using a 6-DoF magnetic tracker and end-effector feedback control.

The transmission's static load rating is also analyzed to evaluate the design's ability to exert the forces required for needle insertion and provide sufficient stiffness. The end-effector's idler pulleys are the weakest component. Pulley wrap angles and the associated transmission load ratings change depending on the robot configuration. Configuration-dependent pulley load can be calculated as

$$F_{\mathrm{N}} = F_{\mathrm{c}} \sin\left(\frac{\theta}{2}\right) \tag{3.4}$$

where F_{N} is the normal force on the idler pulley's bearings, F_{c} is the cable tension, and θ is the pulley's wrap angle. The pulley wrap angle is represented as $\theta = \theta_{\mathrm{joint}} + \theta_{\mathrm{offset}}$ where θ_{joint} is the current joint angle and θ_{offset} is the cable wrap angle at the robot's nominal configuration which is varies based on the idler due to the robot design. At a configuration, a joint transmission's load rating is modeled as $\tau = r_{\mathrm{jp}} F_{\mathrm{min}}$ if a revolute joint or directly as F_{min} if a prismatic joint. r_{jp} is the

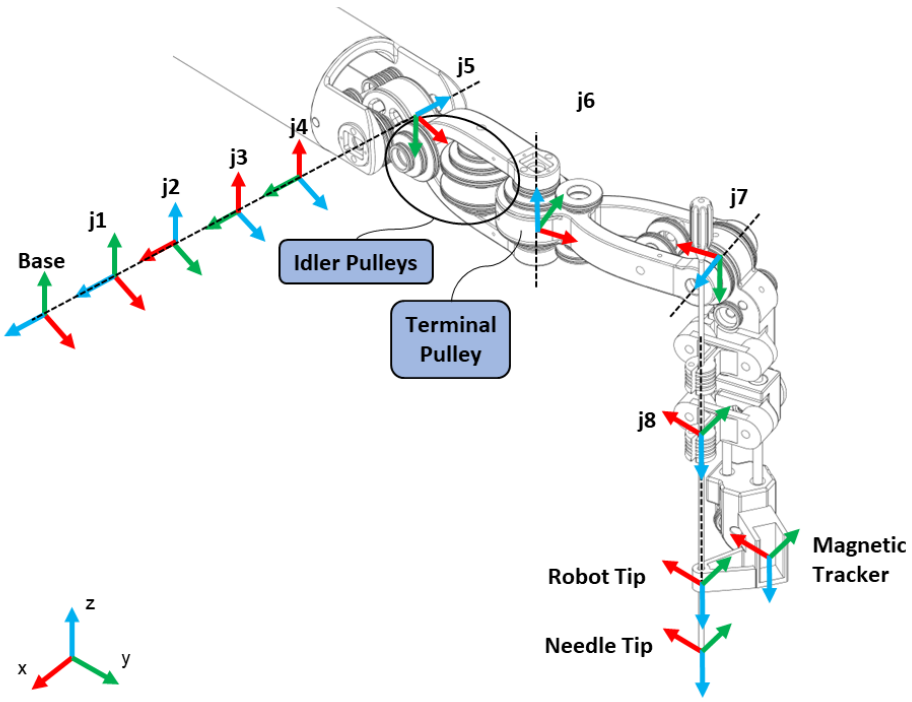

Figure 3.5: Kinematics diagram for the in-bore joints of CRANE. The base joints (outside of the image) are modeled as virtual-joints coinciding at the first in-bore joint and provide gross positioning providing cartesian linear motion. The idler pulleys enable cable pass-throughs and are located on all intermediate joints and links. The pulleys labeled on link 5 provide support for the drive cables for joints 6, 7, and 8.

joint pulley radius and F_{min} is defined as:

$$F_{\text{min}} = \min_{q \varepsilon Q, i \varepsilon N} \frac{F_{\text{r}}}{\sin\left(\frac{q_i}{2}\right)} \tag{3.5}$$

for each joint angle, q, in the joint's range, Q, and every joint, i, in the cable-driven end-effector's joints, $N = 4$. F_{r} is the rated pulley load. The pulley load rating was evaluated throughout the joint range using the idler pulley's bearing load ratings (R2-5 bearing, $117N$ static radial load). The transmission is rated for $2.5Nm$, $1.25Nm$, $1.25Nm$, and $50N$ for the revolute and prismatic cable-driven joints from proximal to the distal end.

3.2.3 System and Software Architecture

The system architecture (Fig. 3.6) focuses on safety and extensibility. Real-time Embedded Computers (FPGAs and microcontrollers) run high frequency and jitter-sensitive control, allowing for independent development and upgrade of the high-level control system. The Desktop Computer hosts the user interface and high-level robot control, including kinematics and path planning.

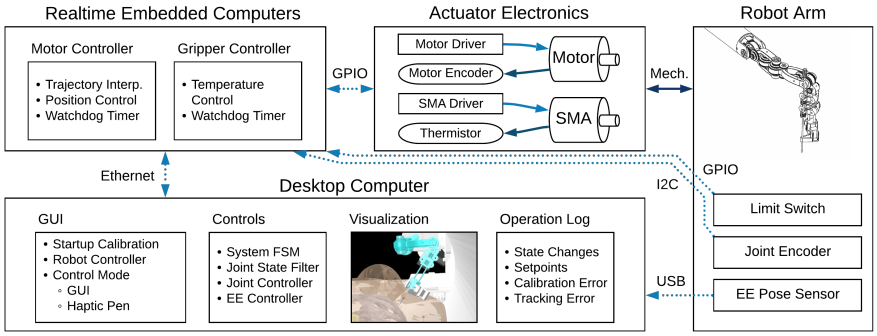

Figure 3.6: The Desktop Computer provides the User Interface and high-level intelligent high-level trajectory planning. Embedded Computers provide hardware sensing and control for safety-critical features and interfacing with the high-level control computer. The system is set up in a distributed architecture providing hard-real time control for higher rate components with more relaxed constraints for high-level interfacing to ease development and algorithm evaluation while retaining system safety.

User Datagram Protocol (UDP) over Ethernet with a dedicated network switch provides an extensible interface between computers. There are two primary electronic subsystems: Motor Controller and Gripper Controller. These components interface with the primary control computer, which performs high-level system coordination and user interface. The centralized motor control motherboard, system power supplies, a network switch, and external interfaces, including emergency stop, power switch, AC input, and RJ-45 ethernet connection, are housed in the robot's base. Watchdog timers and error detection algorithms are implemented on the real-time embedded computers and automatically disable power to the motors and needle grippers in case of significant tracking errors or low update rates, for instance, due to disconnection or software failure from the Desktop Computer. When combined with the mechanical safeties, this makes the system

fail-passive. Redundant position sensors, including magnetic joint encoders and limit switches, are located on all axis and connected to the Desktop Computer via an ARM Cortex M7. A custom ARM Cortex M3-based control board manages the needle clutches. Shaft-mounted magnetic encoders directly sense joint positions. An Ascension trakSTAR magnetic tracker provides direct tip position and orientation sensing for the robot's end-effector's tip near the needle insertion point on the human and directly interfaces with the Desktop Computer over USB.The Realtime Embedded Computer's Motor Controller runs $1khz$ synchronized motor position control with synchronized velocity and acceleration limited trajectory interpolation.

Robot Operating System (ROS) forms the basis for the multiple processes on the Desktop Computer via a standard messaging system. The Desktop Computer runs the less-jitter sensitive software, including robot kinematics and planning, image guidance, and user interaction. The device's multiple user interface options provide flexibility depending on the situation and physician's preference. Control methods range from full automation given their Target Needle Insertion transform to manual joint control. The primary User Interface interface is a Qt5-based graphical user interface that handles system initialization and setup, direct joint level control, and end-effector control. The joint control node GUI allows the user direct joint control via on-screen buttons and visual monitoring through plots of each joint motor; both the end effector (EE) control node GUI and Touch Haptic Control node allows the user to set a desired EE position and orientation via button press or hand motion.

3.2.4 Kinematics

The robot's kinematics chain is described using the Modified Denavit-Hartenberg (DH) parameters, shown in Table 3.2. The DH parameters define the position of the next frame relative to the previous frame

$$c_{n+1} = c_n + ax_n + dz_{n+1} \tag{3.6}$$

and orientation relative to the previous frame

$$R_{n+1} = R_n \begin{bmatrix} 1 & 0 & 0 \\ 0 & \cos\alpha & -\sin\alpha \\ 0 & \sin\alpha & \cos\alpha \end{bmatrix} \begin{bmatrix} \cos\theta & -\sin\theta & 0 \\ \sin\theta & \cos\theta & 0 \\ 0 & 0 & 1 \end{bmatrix} \tag{3.7}$$

where R_n is the orientation and c_n is the position of the nth frame relative to the robot's base frame, B and q_n is the position of the nth joint. For this robot with 8 revolute and prismatic axes, $n \in \{1,...,9\}$ with $n = 9$ as the robot's end-effector frame and $n = 1$ as the robot's base frame. The robot base to tip, also referred to as end-effector (EE), transform is defined as

$${}^{\mathrm{B}}T^{\mathrm{B}}_{\mathrm{Tp}} = fk(q) \quad \text{for} \quad q \in \mathbb{R}^8 \tag{3.8}$$

define the joint positions, $fk(q)$ is defined by chaining together the link transforms described by the DH convention, B is the robot base coordinate frame and the default coordinate frame for transforms if unlisted, and ${}^{A}T^{C}_{B}$ describes a 4×4 homogenous transform $\in$ SE(3) from coordinate from A to coordinate frame B relative to base frame C.

The motor and joint positions, $\theta, q \in \mathbb{R}^8$, are related as

$$q = L\theta \tag{3.9}$$

where L is the 8×8 coupling matrix. In the case of joint mounted actuators or an uncoupled transmission, L is diagonal and corresponds to the simple gear-ratio of the transmission, as in

Table 3.2: Modified DH parameters for CRANE where p is a prismatic joint and r is a revolute joint

Frame	Type	a (meters)	α (rad)	D (meters)	θ (rad)
1	p	0	$-\frac{\pi}{2}$	q_1	0
2	p	0	$-\frac{\pi}{2}$	q_2	$-\frac{\pi}{2}$
3	p	0	$-\frac{\pi}{2}$	q_3	$-\frac{\pi}{2}$
4	r	0	0	0	q_4
5	r	0	$\frac{\pi}{2}$	0	$q_5 + \frac{\pi}{2}$
6	r	7e-2	$\frac{\pi}{2}$	0	q_6
7	r	7e-2	$\frac{\pi}{2}$	3e-2	$q_7 - \frac{\pi}{2}$
8	p	1e-2	$-\frac{\pi}{2}$	q_8	0
9	-	0	0	6e-2	$\frac{\pi}{2}$

our $q \in \{1, ..., 4\}$. In coupled situations, L is upper triangular. Due to manufacturing tolerances, L is constructed during a calibration step from data row-wise and calculated as a least-squares linear-regression problem as

$$L_{i,*} = q_{i,*}\theta^{\dagger} \quad \text{where} \quad \theta^{\dagger} = \theta^{T}\left(\theta\theta^{T}\right)^{-1} \tag{3.10}$$

for each row i of L with $q_{i,*}$ being a time series of m samples a single joint's angle and $\theta \in \mathbb{R}^{8\times m}$ being a time series of all motor angles being used as inputs for the coupling matrix for 8 output joints. Here, joint $q \in \{1, ..., 4\}$ are calibrated individually as scalar terms and $q \in \{5, .., 8\}$ are calibrated together as a matrix.This matrix can be calculated analytically from the system design or empirically off observed data, but by doing it empirically, errors between ideal and actual kinematic parameters are reduced.

3.2.5 End-effector and Joint Control

The estimated joint state, q_{est}, is constructed via a complementary filter between the motor's velocity, $\dot{\theta}$, and the magnetic joint encoders position, q_{meas}, as

$$q_{\text{est}} = \alpha L\dot{\theta}_{\text{meas}}\Delta T + (1-\alpha)q_{\text{meas}} \tag{3.11}$$

for a sampling time, ΔT, and weighting parameter, α, corresponding to the changeover frequency of the filter between the two sensors. The complementary filter helps to reduce errors resulting from high frequency noise in magnetic joint encoder readings and the coupling matrix equation's errors due to the cable-transmission's spring-stiffness.

This joint angle estimate, q_{est} is used to update the motor set-point position, θ_{set} following

a PD control law in the joint space

$$\theta_{\text{set}} \leftarrow \theta_{\text{set}} + \Delta\theta \quad \text{for} \quad \Delta\theta = L^{-1}\left(K_p e_q + K_d \frac{de_q}{dt}\right) \tag{3.12}$$

where $e_q = q_{\text{set}} - q_{\text{est}}$, q_{set} is the joint angle setpoint, and K_p, K_d are the proportional and derivative gains. EE pose errors are calculated for position and orientation as

$$\begin{aligned} e_{\text{pos}} &= x_{\text{targ}} - x_{\text{meas}}, \text{ and} \\ e_{\text{ori}} &= \angle(z_{\text{targ}} z_{\text{meas}})(z_{\text{targ}} \times z_{\text{meas}}) \end{aligned} \tag{3.13}$$

where

$$\angle(z_{\text{targ}}, z_{\text{meas}}) = \cos^{-1}\left(\frac{z_{\text{targ}}^T z_{\text{meas}}}{\|z_{\text{targ}}\|_2 \|z_{\text{meas}}\|_2}\right). \tag{3.14}$$

x_{targ} and x_{meas} are target and measured translation vectors of the target tip transform, ${}^{\text{B}}T_{\text{Tpt}}$, and measured tip transform, ${}^{\text{B}}T_{\text{Tpm}}$. z_{targ} and z_{meas} are the Z axis vectors of the rotation sub-matrix of ${}^{\text{B}}T_{\text{Tpt}}$ and ${}^{\text{B}}T_{\text{Tpm}}$. The target transform described by ${}^{\text{B}}T_{\text{Tpt}}$ is provided from the User Interface. The measured tip transform in the robot base frame is calculated as ${}^{\text{B}}T_{\text{Tpm}} = {}^{\text{B}}T_{\text{Tr}}\,{}^{\text{Tr}}T_{\text{Tp}}$ where ${}^{\text{Tr}}T_{\text{Tp}}$ is the magnetic tip tracker's pose in the tracker's base frame. The transform from the robot's base frame to the tracker's base frame, ${}^{\text{B}}T_{\text{Tr}}$, is found by solving a least squares transform between ${}^{\text{Tr}}T_{\text{Tpm}}$ and ${}^{\text{B}}T_{\text{Tp}}$ based on a initialization sequence. As needles are symmetric, the orientation error does not include rotation around the EE's z-axis.

The joint angle update is calculated as

$$\begin{aligned} q_{\text{set}} &\leftarrow q_{\text{est}} + \Delta q \quad \text{where} \\ \Delta q &= K_{\text{pos}} J_{\text{pos}}^{\dagger} e_{\text{pos}} + K_{\text{ori}} J_{\text{ori}}^{\dagger} e_{\text{ori}} \end{aligned} \tag{3.15}$$

where the current end-effector position and orientation Jacobians, $J_{\text{pos}} \in \mathbb{R}^{3\times 8}$ and $J_{\text{ori}} \in \mathbb{R}^{3\times 8}$, come from the forward kinematics and is evaluated near the current joint angles q_{est} and $J^{\dagger}$

is the psuedoinverse calculated via the Levenberg-Marquardt algorithm. K_{pos} and K_{ori} are the proportionality control constants for the end-effector controller.

3.3 Experiments

3.3.1 Trajectory Tracking

The system's accuracy was evaluated by performing a virtual Remote Center of Motion trajectory where the robot revolved around a virtual needle tip location using the experimental setup shown in Fig. 3.2. Here, the robot's end-effector follows a cone trajectory simulating the workspace a physician would use during an actual procedure. The Ascension TrackStar magnetic tracker was used for accuracy measurement. The mean resulting accuracy, shown as a time series in Fig. 3.7, across the trajectory was $0.27mm$ and 0.71°.

Two evaluations of the system's trajectory tracking accuracy were performed. In the open-loop test, all joint and end-effector controllers were disabled. Joint angles were purely calculated off the ideal coupling matrix, $\boldsymbol{M}$, without compensation for cable stretch and hysteresis in the in-bore transmission. EE measurements were replaced for the J^{-1} controller with predicted EE positions based on the forward kinematics of the calculated joint angles from the motor. With controllers disabled, position and orientation errors are increased due to the mixture of joint tracking errors, system deflection, and manufacturing errors. Closed loop control using direct end-effector tracking enables the system to accurately reach targets despite these challenges. Of note, errors during open-loop motions are surprisingly low given the long serial kinematic chain.

Needle Gripper: Slipping Force and Speed

Performance regarding clutching force, cycle time, insertion force, and thermal transfer to the needle are evaluated. The needle clutch is 3D printed in a nylon-carbon composite material on a Markforged 3D printer. The two clutches are designed to grip a 15-gauge needle. Slipping

forces were measured using spring scales ($0-50N$ and $0-5N$ ranges). Activated slipping forces are $18N$ and $20N$. Deactivated slipping forces are at $1N$ and $2.25N$.

Additionally, a step-response test was performed. The results, reported in Fig. 3.8, show short on and off times, implying the possibility for rapid clutching for deep needle insertion and clutch deactivation for safety.

3.3.2 Teleoperated CT-guided Needle Insertion

The biopsy task was conducted inside a sliding stage CT scanner (GE Revolution) at the University of California San Diego's Thornton Hospital. Scan settings of 120 kVp, 300mAs per slice, 0.5-second rotation time were used. Testing was performed on a custom lung phantom, similar to the designs presented in [SK92b]. The lung phantom consists a plastic resin rib cage with a volume of 12" x 11" x 7" containing a dry preserved pig lung. The remaining space in the rib cage is filled with gel-candle wax to simulate fat and wrapped with two durometers of silicone sheet to simulate muscle and skin. Several different size silicone nodules are planted into the lung to simulate tumors.

An experienced radiologist teleoperated the robot using from the control room (note their silhouettes behind the glass) using our EE control GUI to guide needle to the nodules with CT image data, external camera and Coppeliasim simulation of the robot were used for visual guidance. The needle insertion vector had less than 1.2° error from nominal. Interference was not observed between the robot, magnetic tracker, and scanner. Streaking artifacts within the CT image due to the robot's end-effector are minor.

3.4 Discussion

This chapter presents a teleoperated 10-DoF, low-profile and highly dexterous robotic needle placement platform for efficient and accurate needle insertion across the human abdominal

region.

System backlash is low and through closed-loop control. End-effector error is greatly decreased providing the performance required for effective needle insertion in robotic applications. Repeatability with a trajectory tracking positional accuracy of $0.27mm$ and orientation accuracy of $0.7°$. Minimal shadowing and artifacts are visible in the CT image. A novel clutching mechanism is included which enables long-needle insertions in an easy-to-manufacture and sterilizable assembly.

The control scheme presented in this chapter requires the physician to manually set up and control the device within its coordinate system. The following chapter explores collision-free path planning within the CT scanner for automatic device setup and alignment between the CT scanner and the robot's coordinate systems to support direct image-guided robot control.

3.5 Acknowledgments

Chapter 3 is, in part, a reprint of material from D. Schreiber, Z. Yu, H. Jiang, T. Henderson, G. Li, J. Yu, R. Zhu, A. Norbash, M. Yip, "CRANE: a 10 Degree-of-Freedom, Tele-surgical System for Dexterous Manipulation within Imaging Bores" in 2022 IEEE International Conference on Robotics and Automation (ICRA) and, in part, has been submitted for publication of the material as it may appear in IEEE Transactions on Robotics, 2023, D. Schreiber, Z. Yu, T. Henderson, A. Norbash, M. Yip. The dissertation author is the primary author of these papers.

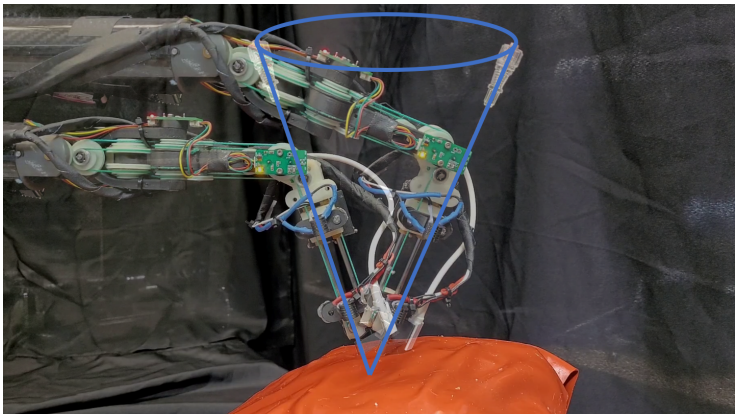

(a) Illustration of RCM trajectory

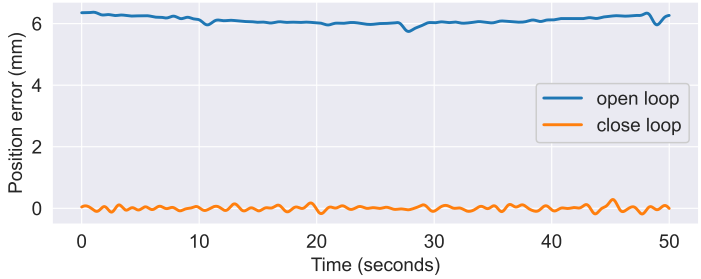

(b) Position Error Plot for RCM trajectory

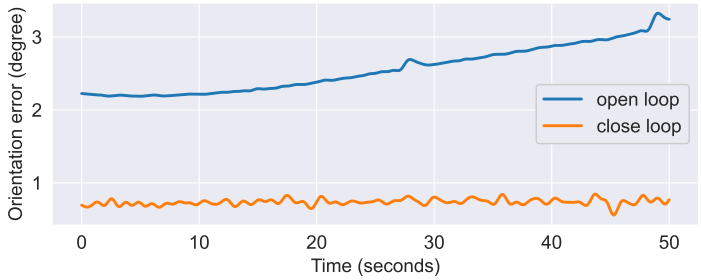

(c) Orientation Error Plot for RCM Trajectory

Figure 3.7: Open-loop evaluation is performed using motor position control without feedback from joint encoders or end-effector controller. Close-loop control runs position control using joint encoders for feedback and direct end-effector position measurement from a magnetic 6D tracker, matching the accuracy of the tracker itself. Open-loop accuracy is surprisingly good given CRANE's long and low profile kinematic chain. Closed loop control provides far higher accuracy, partially enabled by the low backlash, friction, and hysteresis transmission.

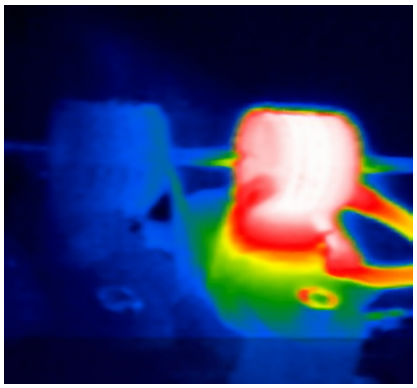

(a) Thermal image

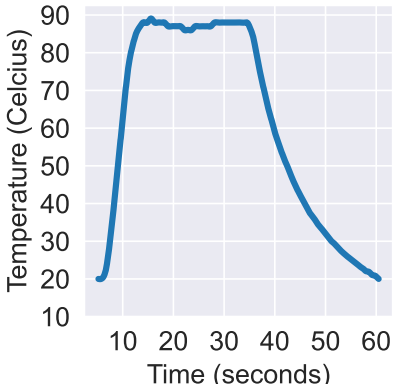

(b) Step response

Figure 3.8: (a) shows a thermal image of a clutching needle driver on the robot end-effector with one clutch activated. (b) shows step response collected from the clutch with Joule heating and air-blast assisted cooling. The clutch is able to be rapidly activated and deactivated, enabling rapid insertion resetting during a procedure and quick passive removal in case of emergency shutdown.

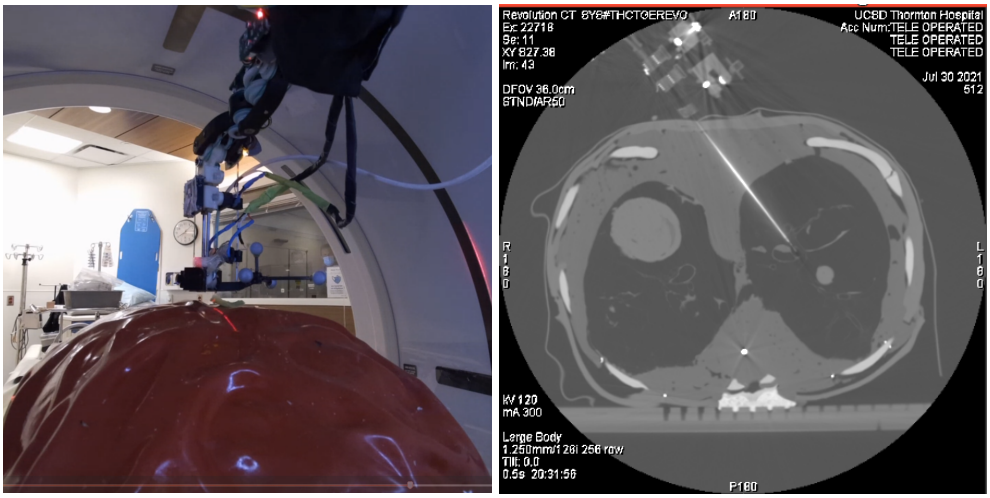

Figure 3.9: Left: CRANE within a CT scanner, remotely teleoperated by an experienced radiologist and technician, visible behind the glass window. Right: CT image of robot being teleoperated to reach lesion in the central right lung of the phantom.

Chapter 4

Automated Needle Alignment

Robots can eliminate the multiple punctures and procedures required while enabling physicians to treat small early-stage cancer via a minimally invasive approach. However, existing robotic platforms have a complex and lengthy setup, limited applicability and large size, imaging artifacts, insufficient accuracy, and limited needle compatibility have limited their clinical application. Our robotic platform, CRANE (introduced in Chapter 3), tackles these main limiting issues via its novel mechanical design coupled with planning method while retaining the accuracy of previous systems. However, the method used for device control requires manual physician setup. This can be incredibly challenging, given the system's redundant joints.

This chapter presents an automated method for in-bore robot planning and control, enabling physicians to use the device without requiring innate knowledge of the device's kinematic structure. For this to work, the device must have a sufficient dexterity to place needles across the patient's body. Therefore, the device's dexterity is additionally evaluated. The contributions of this chapter are as follows:

1. *In-bore planning and control of redundant robot* – clinically focused metrics for workspace and dexterity are utilized within a unified framework incorporating physician-specified task prioritizing for control of a redundant robot. This framework enables fully hands-free

device operation and is used for simulated design evaluation and control synthesis during in-situ experiments.

2. *Design evaluation of needle insertion robots* – the robot's ability to perform a generalized synthetic cases load is tested. Synthetic cases cover a variety of human body shapes and sizes and are created based on observed clinical cases. This method can be used to help improve robot design to maximize the possible needle insertion trajectories in patients, resulting in improved safety, ease of use, and a more considerable breadth of possible procedures with a single platform.

3. *Closed loop robot control from CT images* – method for automatically tracking and closed-loop control to align a robot to a target pose based on CT-scan feedback. This method improves the robot's end-effector pose tracking and needle placement accuracy and is tested in-situ.

4.1 Dexterous Trajectory Planning and Control

This section describes a method enabling the robot to safely and dexterously manipulate a needle within a scanner while avoiding collisions with the environment, enabling the physician to be hands-off during device setup. This is accomplished via a hierarchical planning and control scheme for two phases of the procedure: Automated Device Setup to $\boldsymbol{T}_{\text{tn}}^{\text{b}}$ during *Procedure Planning Phase* and fine adjustment of the robot's configuration around $\boldsymbol{T}_{\text{tn}}^{\text{b}}$ during *Procedure Execution Phase*. For device setup, an optimal Dexterous Device Setup Configuration, $\boldsymbol{q}^*$, for $\boldsymbol{T}_{\text{tn}}^{\text{b}}$ is determined. Then, a collision-free configuration space trajectory, $\boldsymbol{Q} : \left\{\boldsymbol{q}_0, \boldsymbol{q}_1, \ldots, \boldsymbol{q}_{n-1}, \boldsymbol{q}^*\right\}$, is determined using a sampling-based motion planner (BIRRT implemented in OMPL [SMK12]). Once $\boldsymbol{Q}$ is executed, a Local Controller is used for servoing the end-effector in the case of small adjustments of $\boldsymbol{T}_{\text{tn}}^{\text{b}}$.

Table 4.1: Mathematical symbols for Automated Robot Trajectory Planning

Symbols	Definition
$\boldsymbol{q}$, $\boldsymbol{\theta}$	joint and actuator configuration
$\boldsymbol{Q}$	trajectory of joint configurations expressed as a matrix
$\mathcal{X}$	set of poses
$\mathcal{B}$	set of obstacles
D	dimension of a configuration, i.e., the DoF of the robot
$\boldsymbol{T}$, $\boldsymbol{R}$, $\boldsymbol{t}$	transformation matrix comprising rotation matrix and translation vector with rotation sub-matrix and translation sub-vector
$\text{ROTMAT}(\boldsymbol{n}, \psi)$	rotation matrix via Rodrigues' formula around $\boldsymbol{n}$ axis an angle of ψ
$\mathcal{C}$	Configuration space (C-Space)
$d_B(\boldsymbol{q})$	distance to obstacles $\mathbb{B}$ in Workspace
$d_o(\boldsymbol{T}_{\text{tar}}, \boldsymbol{T}_{\text{cur}})$	task orientation difference between poses
$d_p(\boldsymbol{T}_{\text{tar}}, \boldsymbol{T}_{\text{cur}})$	position difference between poses
Δ_{adj}	zenith angle for conical RCM adjustability evaluation
$\text{FK}(\boldsymbol{q})$	Forward Kinematics pose
$\boldsymbol{J}(\boldsymbol{q})$, $\boldsymbol{J}^{\dagger}(\boldsymbol{q})$, λ	Jacobian matrix, damped inverse Jacobian matrix, and damping term
$\boldsymbol{f}$	wrench
ε, ε_p, ε_o	pose error tolerance consisting of position and orientation
$\boldsymbol{e}, \boldsymbol{e}_{\text{p}}, \boldsymbol{e}_{\text{o}}$	pose error vector comprising position and orientation
$c(\boldsymbol{q})$	configuration cost function
$\boldsymbol{M}$, $\boldsymbol{K}$	actuator to joint space matrix and actuator controller gains
τ	actuator torque

4.1.1 Coordinate Systems and Transforms

This system has three reference coordinate systems: the CT scanner, the magnetic tracker, and the robot. Homogeneous transforms provide relationships between coordinate frames, represented as

$$ {}^{a}\boldsymbol{T}_{\mathrm{c}}^{\mathrm{b}} = \begin{bmatrix} \boldsymbol{R} & \boldsymbol{t} \\ 0 & 1 \end{bmatrix} \in SE(3) \tag{4.1} $$

providing the transform from c to b relative to basis vectors a for rotation matrix $\boldsymbol{R} \in SO(3)$ and translation vector $\boldsymbol{t} \in \mathbb{R}^3$. Typically the basis vectors a are excluded from the transformation notation and assumed to be their system's base coordinate system. Transformation matrices represent both transforms between coordinate systems (as an operator) and poses within a coordinate system.

The CT scanner and magnetic tracker are both sensors used as inputs to our system, with the robot as the primary coordinate system used internally. The transformation matrices below define poses relative to the three fixed reference coordinate systems relevant to our system.

Key poses defined relative to the CT scanner base frame, $\boldsymbol{T}^{\mathrm{sb}}$, are:

- $\boldsymbol{T}_{\mathrm{tn}}^{\mathrm{sb}}$ defines the Target Needle Insertion pose. This is typically on the patient's skin and serves as the Remote Center of Motion (RCM) location for adjustments made after insertion. This is created based on input by the physician using the GUI.

- $\boldsymbol{T}_{\mathrm{fd}_i}^{\mathrm{sb}}$ defines the pose for the spherical CT-visible fiducials, fd_i, within the CT scanner frame and embedded in the magnetic tracker mount used for referencing the robot and scanner's coordinate system. These are located during the calibration step within the CT images (described in Sect. 4.1.1).

Key poses defined relative to the magnetic tracker base frame, $\boldsymbol{T}^{\mathrm{mb}}$, are:

- $\boldsymbol{T}_{\mathrm{mtrkt}}^{\mathrm{mb}}$, $\boldsymbol{T}_{\mathrm{mtrkb}}^{\mathrm{mb}}$ define the pose of the magnetic tracker mounted to robot tip and phantom; measured by the Ascension trackStar magnetic tracker at $100Hz$.

- $\boldsymbol{T}_{\mathrm{fd}_i}^{\mathrm{mtrkb}}$, is the static transform to each CT-visible fiducials relative to the magnetic tracker used for referencing the magnetic tracker and scanner's coordinate systems.

Key poses defined relative to the robot base frame, $\boldsymbol{T}^{b}$, are:

- $\boldsymbol{T}_{\mathrm{EE}}^{\mathrm{b}}$ defines the robot's EE pose calculated via the Forward Kinematics function (defined in Sect. 4.1.1). This pose is attached to the needle insertion mechanism's needle guide, and the Z-axis is coaxial with the needle grippers and needle guide directed distally to the robot.

- $\boldsymbol{T}_{\mathrm{trk}}^{\mathrm{EE}}$, is the static transform from the robot's EE to the magnetic tracker mounted on the robot needle guide.

The transforms between the three coordinate base frames are calculated in a pre-procedural calibration step providing $\boldsymbol{T}_{\mathrm{mb}}^{\mathrm{b}}$, between the magnetic tracker's base and the robot base, and $\boldsymbol{T}_{\mathrm{sb}}^{\mathrm{b}}$, between the scanner's base and the robot base (described in Sect. 4.1.1).

Forward Kinematics

The robot's kinematics chain is described using *Modified Denavit-Hartenberg (DH) Parameters* which attaches coordinate systems to each joint of the robot and defines the transform between these coordinate frames as $\boldsymbol{T}_{i}^{i-1}(q_i) = \boldsymbol{T}_{\mathrm{x}}(\alpha_i, a_i)\boldsymbol{T}_{\mathrm{z}}(\theta_i, d_i)$ where

$$\boldsymbol{T}_{\mathrm{x}}(\alpha_i, a_i) = \begin{bmatrix} 1 & 0 & 0 & a_i \\ 0 & \cos(\alpha_i) & -\sin(\alpha_i) & 0 \\ 0 & \sin(\alpha_i) & \cos(\alpha_i) & 0 \\ 0 & 0 & 0 & 1 \end{bmatrix} \tag{4.2}$$

$$\boldsymbol{T}_{\mathrm{z}}(\theta_i, d_i) = \begin{bmatrix} \cos(\theta_i) & -\sin(\theta_i) & 0 & 0 \\ \sin(\theta_i) & \cos(\theta_i) & 0 & 0 \\ 0 & 0 & 1 & d_i \\ 0 & 0 & 0 & 1 \end{bmatrix} \tag{4.3}$$

and q_i is substituted into d_i for prismatic joints and q_i is substituted into θ_i for revolute joints.

The forward kinematics function FK($\boldsymbol{q}$), defines the robot base to end-effector (EE) transform by chaining together the transforms described by the DH convention:

$$\mathrm{FK}(\boldsymbol{q}) = \boldsymbol{T}^{\mathrm{b}}_{\mathrm{EE}} = \boldsymbol{T}^{\mathrm{b}}_{1} \prod_{i=2}^{8} \boldsymbol{T}^{i-1}_{i}(\boldsymbol{q}_i) \tag{4.4}$$

with DH-parameters provided in Table 4.2.

Table 4.2: DH-parameters for CRANE where p is prismatic and r is revolute. All angles and distances are in radians and meters, respectively.

Frame	Type	a_{i-1}	α_{i-1}	D_i	θ_i
1	p	0	0	q_1	0
2	p	0	$-\frac{\pi}{2}$	q_2	$-\frac{\pi}{2}$
3	p	0	$-\frac{\pi}{2}$	q_3	$-\frac{\pi}{2}$
4	r	0	0	0	q_4
5	r	0	$\frac{\pi}{2}$	0	$q_5 + \frac{\pi}{2}$
6	r	7e-2	$\frac{\pi}{2}$	0	q_6
7	r	7e-2	$\frac{\pi}{2}$	3e-2	$q_7 - \frac{\pi}{2}$
8	-	1e-2	$-\frac{\pi}{2}$	2e-2 $+q_8$	0

Magnetic Tracker, Scanner, and Robot Calibration

The robot to magnetic tracker calibration, $\boldsymbol{T}^{\mathrm{b}}_{\mathrm{mb}}$, and robot to scanner calibration $\boldsymbol{T}^{\mathrm{b}}_{\mathrm{sb}}$, transforms are calculated based on a calibration procedure to minimize a least squares error.

$$\min_{\boldsymbol{T}^{\mathrm{b}}_{\mathrm{t}} \in SE(3)} \sum_{i=0}^{N} \left|\left| \hat{\boldsymbol{P}}_i - \boldsymbol{T}^{\mathrm{b}}_{\mathrm{t}} \boldsymbol{P}_i \right|\right|_2 \tag{4.5}$$

where $\boldsymbol{T}^{\mathrm{b}}_{\mathrm{t}}$ is the calibration transform between robot base frame and the target base frame. $\boldsymbol{P} = \{\boldsymbol{p}_0, \ldots, \boldsymbol{p}_N\}$ and $\hat{\boldsymbol{P}} = \{\hat{\boldsymbol{p}}_0, \ldots, \hat{\boldsymbol{p}}_N\}$ are the augmented Cartesian calibration point sets for N sample points and $\boldsymbol{p}, \hat{\boldsymbol{p}} = \begin{bmatrix} x & y & z & 1 \end{bmatrix}^\top$.

For $\boldsymbol{T}^{\mathrm{b}}_{\mathrm{mb}}$, a calibration trajectory is performed using the robot's linear base joints, $\boldsymbol{Q}_{\mathrm{b}} \in$

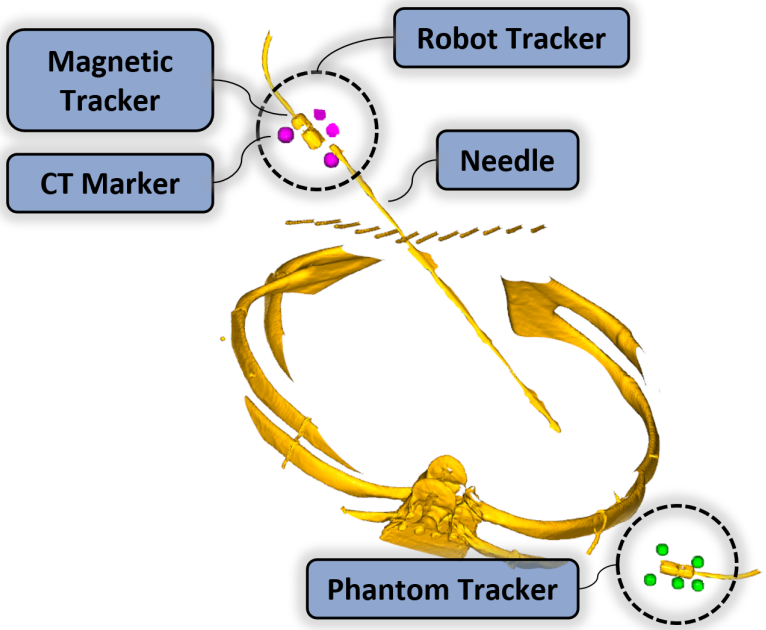

(a) Robot and Tracker Fiducials

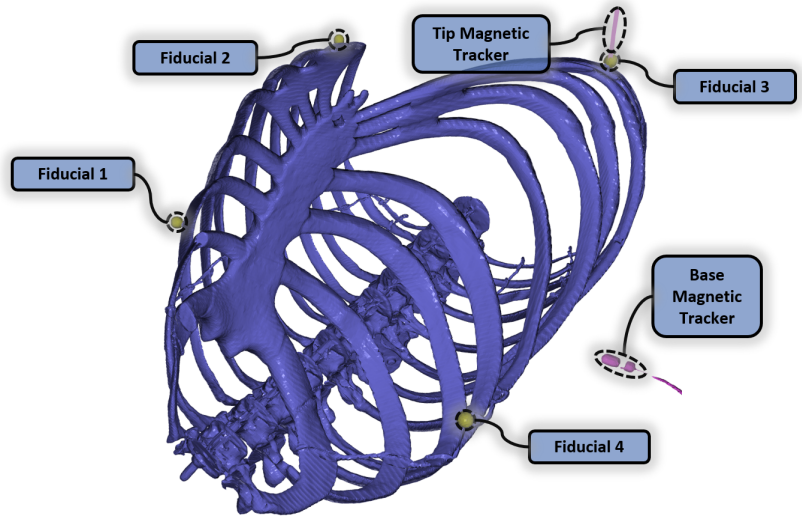

(b) Ribs Fiducials

Figure 4.1: The robot and phantom are localized within the CT scanner based on multiple rigid body fiducials, visualized here as part of the alignment process. The fiducials have a high Hounsfield Unit (HU) value of 5000HU. (a) shows an example arrangement of the fiducials and magnetic trackers mounted to the phantom and robot via a nylon container (60HU). (b) shows an arrangement of the fiducials and magnetic tracker mounted to the phantom body with the tip magnetic tracker touching a fiducial.

$\mathbb{R}^{N\times 3}$. Each sample $\boldsymbol{p}_i = \boldsymbol{t}_{\text{FK}}$ for $\boldsymbol{T}_{\text{FK}} = \text{FK}(\boldsymbol{q}_i)\boldsymbol{T}^{\text{EE}}_{\text{trk}}$ and $\hat{\boldsymbol{p}}_i = \boldsymbol{t}_{\text{mtrk}}$ for the corresponding timestep $\boldsymbol{T}^{\text{mb}}_{\text{mtrkt},i}$. For $\boldsymbol{T}^{b}_{sb}$, a single CT scan is taken and processed to localize the fiducials within the scanner's coordinate system. Each sample $\boldsymbol{p}_i = \boldsymbol{t}_{\text{fid}}$ for $\boldsymbol{T}_{\text{fid}} = \boldsymbol{T}^{\text{b}}_{\text{mb}}\boldsymbol{T}^{\text{mb}}_{\text{mtrkb}}\boldsymbol{T}^{\text{mtrkb}}_{\text{fd},i}$ for $i \in \{1..N\}$ and $\hat{\boldsymbol{p}}_i$ are the measured positions of the fiducial's centroids found within the CT image.

4.1.2 Dexterous Robot Setup Problem

A Dexterous Robot Setup Configuration is one for which the robot can feasibly insert a needle into the patient and manipulate the needle around the nominal $\boldsymbol{T}^{\text{b}}_{\text{tn}}$. This is defined based on several metrics, including joint limits, workspace singularities, and collisions with the environment, all of which affect the system's ability to perform the insertion successfully. The C-space $\mathcal{C} \subset \mathbb{R}^D$ where D is the robot's number of joints defines the possible robot configurations and contains the following important sub-spaces for our optimization problem:

1. Feasible C-space, $\mathcal{C}_{\text{feas}}$, can apply sufficient forces and moments to insert and adjust the angulation of the needle.

2. Collision-free C-space, $\mathcal{C}_{\text{goal}}$, where $\text{FK}(\mathcal{C})$ is sufficiently close to $\boldsymbol{T}^{\text{b}}_{\text{tn}}$.

3. Collision-free C-space, $\mathcal{C}_{\text{free}}$, where the robot is sufficiently far from a collision with obstacles, including environment and self-collisions.

4. Adjustable C-space, $\mathcal{C}_{\text{adj}}$, where the robot can perform an RCM adjustment around the Target Needle Insertion pose for a defined conical region.

For our needle insertion task, we define $\mathcal{C}_{\text{feas}}$ comprising non-singular configurations where the system can manipulate a needle with sufficient force. The Jacobian matrix, $\boldsymbol{J}(\boldsymbol{q}) \in \mathbb{R}^{6\times d}$ and denoted as $\boldsymbol{J}$, relates EE twists, $\mathbf{v} \in \mathbb{R}^6$ and joint velocities, $\dot{\boldsymbol{q}} \in \mathbb{R}^D$ as well as relating EE

wrenches, $\boldsymbol{f} \in \mathbb{R}^6$, and joint torques, $\boldsymbol{\tau} \in \mathbb{R}^D$:

$$\boldsymbol{v} = \boldsymbol{J}\dot{\boldsymbol{q}} \text{ and } \boldsymbol{\tau} = \boldsymbol{J}^\top \boldsymbol{f} \tag{4.6}$$

The space and body Jacobians, $\boldsymbol{J}^{\mathrm{s}}$ and $\boldsymbol{J}^{\mathrm{b}}$, represented in the robot's base coordinate system and EE coordinate systems are used throughout this section. Using these relationships, $\mathcal{C}_{\text{feas}}$ is:

$$\mathcal{C}_{\text{feas}} = \{\boldsymbol{q} \in \mathcal{C} | \boldsymbol{J}^{\mathrm{b},\top} \boldsymbol{F}_{\text{req}} < \boldsymbol{\tau}_{\max}\} \tag{4.7}$$

where $\boldsymbol{f}_{\text{req}} \in \mathbb{R}^6$ is the required force and moment to insert and manipulate the needle represented as a wrench in the EE frame and $\boldsymbol{\tau}_{\max} \in \mathbb{R}^D$ is the robot's maximum joint torques.

Furthermore, we define $\mathcal{C}_{\text{goal}}$ as configurations with the robot's EE near the Target Needle Insertion pose $\boldsymbol{T}^{\mathrm{b}}_{\mathrm{tn}}$. The function $d_p(\boldsymbol{T}_{\text{tar}}, \boldsymbol{T}_{\text{cur}})$ computes the vector difference between the position vectors of two poses and $d_o(\boldsymbol{T}_{\text{tar}}, \boldsymbol{T}_{\text{cur}})$ computes the axis-angle difference between the Z-axis of two poses:

$$d_p(\boldsymbol{T}_{\text{tar}}, \boldsymbol{T}_{\text{cur}}) = \boldsymbol{t}_{\text{tar}} - \boldsymbol{t}_{\text{cur}} \tag{4.8}$$

$$d_o(\boldsymbol{T}_{\text{tar}}, \boldsymbol{T}_{\text{cur}}) = \cos^{-1}\left(\frac{\tilde{\boldsymbol{z}}^\top \boldsymbol{z}}{\|\tilde{\boldsymbol{z}}\|_2 \|\boldsymbol{z}\|_2}\right)(\tilde{\boldsymbol{z}} \times \boldsymbol{z}) \tag{4.9}$$

where $\tilde{\boldsymbol{z}} = \boldsymbol{R}_{\text{targ},[z]}$ and $\boldsymbol{z} = \boldsymbol{R}_{\text{cur},[z]}$ are the Z-axis vectors of the rotation matrix from their corresponding poses. Using these difference functions, $\mathcal{C}_{\text{goal}}$ is:

$$\begin{aligned} \mathcal{C}_{\text{goal}} = \{\boldsymbol{q} \in \mathcal{C}_{\text{feas}} |\ & \|d_o(\mathrm{FK}(\boldsymbol{q}), \boldsymbol{T}^{\mathrm{b}}_{\mathrm{tn}})\|_2 \leq \varepsilon_o \\ & \text{and } \|d_p(\mathrm{FK}(\boldsymbol{q}), \boldsymbol{T}^{\mathrm{b}}_{\mathrm{tn}})\|_2 \leq \varepsilon_p\} \end{aligned} \tag{4.10}$$

where ε_{p} is a predefined position error tolerance and ε_{o} is a predefined orientation error tolerance.

The obstacle-free C-space is the set of robot configurations in which the robot's links are

sufficiently far from obstacles, $\mathcal{B}$, (e.g., scanner, patient, self-collisions):

$$\mathcal{C}_{\text{free}} = \{\boldsymbol{q} \in C | d_B(\boldsymbol{q}) > \varepsilon_d\} \tag{4.11}$$

where $d_B(\boldsymbol{q})$ is the minimum distance from the robot to obstacles and ε_d is a specified minimum distance to collision for environment padding.

Finally, we define $\mathcal{C}_{\text{adj}}$ comprising the region of the configuration space where the robot can perform an RCM adjustment of the needle in a conical region around the current configuration:

$$\begin{aligned} \mathcal{C}_{\text{adj}} = \{\boldsymbol{q} \in \mathcal{C}_{\text{goal}} \cap \mathcal{C}_{\text{free}} | \exists \bar{\boldsymbol{q}} \in \mathcal{C}_{\text{feas}} \text{ s.t.} \\ \text{CONNECTABLE}(\bar{\boldsymbol{q}}, \boldsymbol{q}), \\ \|d_o(\boldsymbol{T}_{\text{rcm}}, \text{FK}(\bar{\boldsymbol{q}}))\|_2 < \varepsilon_{\text{o}}, \\ \|d_p(\boldsymbol{T}_{\text{rcm}}, \text{FK}(\bar{\boldsymbol{q}}))\|_2 < \varepsilon_{\text{p}}, \\ \forall \boldsymbol{T}_{\text{rcm}} \in \mathcal{X}_{\text{rcm}}\} \end{aligned} \tag{4.12}$$

Robot configurations $\boldsymbol{q}$ and $\bar{\boldsymbol{q}}$ are CONNECTABLE if a simple Local Planner can provide a collision-free trajectory, $\boldsymbol{Q} = \{\boldsymbol{q}, .., \bar{\boldsymbol{q}}\}$, between them. Here, the Local Planner is a gradient descent IK method with a nullspace objective. $\boldsymbol{T}_{\text{rcm}}$ is a pose within $\mathcal{X}_{\text{rcm}}$ where $\mathcal{X}_{\text{rcm}} \in SE(3)$ are the space of homogeneous poses within a conical orientation adjustment of $\boldsymbol{T}^{\text{b}}_{\text{tn}}$. $\mathcal{X}_{\text{rcm}}$ is constructed using ROTMAT$(\boldsymbol{n}, \psi)$ which defines the $SO(3)$ rotation matrix from an arbitration rotation angle, ψ, around an arbitrary axis, $\boldsymbol{n}$, via Rodrigues' Formula as:

$$\begin{aligned} \mathcal{X}_{\text{rcm}} = \{\boldsymbol{T}_{\text{adj}} \boldsymbol{T}^{\text{b}}_{\text{tn}} \text{ where} \\ \boldsymbol{R}_{\text{adj}} = \text{ROTMAT}(x, \delta)\text{ROTMAT}(z, \gamma) \text{ and} \\ \boldsymbol{t}_{\text{adj}} = \boldsymbol{0}\ \forall \delta \in [0, \Delta_{\text{adj}}] \text{ and } \forall \gamma \in [0, 2\pi]\} \end{aligned} \tag{4.13}$$

where Δ_{adj} is the zenith angle of the conical region, $\boldsymbol{T}_{\text{adj}}$ is the transform used for RCM angle adjustment defined with with rotation submatrix $\boldsymbol{R}_{\text{adj}}$ and translation subvector $\boldsymbol{t}_{\text{adj}}$. ROTMAT$(x, \alpha)$

and $\text{ROTMAT}(z,\gamma)$ are the rotation matrices around the x and z axis for RCM orientation adjustment, and the translation $\boldsymbol{t}_{\text{adj}}$ is zero due to the RCM motion constraint. Only angulation adjustments are evaluated as the needle is inside the body, and translation would result in significant forces being applied to the tissue.

Using the defined C-space, $\boldsymbol{q}^*$ corresponds to minimizing a corresponding cost function:

$$\boldsymbol{q}^* = \underset{\boldsymbol{q}\in\mathcal{C}_{\text{adj}}}{\arg\min}\, c\left(\boldsymbol{q}\right) \tag{4.14}$$

where $c(\boldsymbol{q})$ can be defined arbitrarily. Our $c(\boldsymbol{q})$ focusing on maximizing dexterity and distance to collision while minimizing joint motion is defined as:

$$c\left(\boldsymbol{q}\right) = \frac{\alpha}{w(\boldsymbol{q})} + \frac{1-\beta}{d_{B\{\text{bor}\}}\left(\boldsymbol{q}\right)} + \frac{\beta}{d_{B\{\text{pat}\}}\left(\boldsymbol{q}\right)} + \frac{\gamma}{d_{\boldsymbol{q_0}}\left(\boldsymbol{q}\right)} \tag{4.15}$$

where $\alpha,\beta\gamma$ are the optimization priorities, $w\left(\boldsymbol{q}\right) = \sqrt{\left|\boldsymbol{J}^{\text{b}}_{[\alpha,\beta]}\boldsymbol{J}^{\text{b},\top}_{[\alpha,\beta]}\right|}$ is a modified version of Yoshikawa manipulability index [Yos85] for the configuration calculated using the rows of the body Jacobian corresponding to roll and pitch orientation axes. Other common dexterity indices [KB87, Asa83] can also be applied. $d_{B\{\text{bor}\}}$ is the minimum distance-to-collision between the robot and the scanner bore, $d_{B\{\text{pat}\}}$ is the minimum distance-to-collision between the robot (excluding needle insertion mechanism) and the patient, and $d_{\boldsymbol{q_0}}\left(\boldsymbol{q}\right)$ is the distance from the evaluated robot configuration to initial robot configuration.

Dexterous Robot Configuration Generator

A general-purpose global optimization algorithm [noai] with $\boldsymbol{q}\in\mathcal{C}_{\text{feas}}$ directly turned into an inequality constraint is used to determine $\boldsymbol{q}^*$. Eq. (4.14) and $\mathcal{C}_{\text{adj}}$ are directly evaluated in the main optimization function. The obstacles set for our optimization is $\mathcal{B} = \{\text{robot, scanner bore, patient body}\}$.

For a redundant robot, the joints can be partitioned as $\boldsymbol{q} = \begin{bmatrix}\tilde{\boldsymbol{q}} & \mathring{\boldsymbol{q}}\end{bmatrix}^\top$ for the non-redundant

joints, $\tilde{\boldsymbol{q}}$, and redundant joints $\mathring{\boldsymbol{q}}$ with respective non-redundant C-space $\tilde{\mathcal{C}} \subset \mathcal{C}$ and redundant C-space $\mathring{\mathcal{C}} \subset \mathcal{C}$. Correspondingly, $\boldsymbol{J}$ can be reorganized into redundant and non-redundant block matrices:

$$\boldsymbol{J} = \begin{bmatrix} \tilde{\boldsymbol{J}} & \mathring{\boldsymbol{J}} \end{bmatrix} \tag{4.16}$$

where $\tilde{\boldsymbol{J}} \in \mathbb{R}^{6\times 6}$ corresponding to the non-redundant joints and $\mathring{\boldsymbol{J}} \in \mathbb{R}^{6\times D-6}$ corresponding to the redundant joints.

The function IKCONFIGURATIONLOSS$(\boldsymbol{T}_{\text{tn}}^{\text{b}}, \boldsymbol{q}_0)$ jointly evaluates the optimization objectives $c(\boldsymbol{q})$ and if $\boldsymbol{q} \in \mathcal{C}_{\text{adj}}$. IKCONFIGURATIONLOSS$(\boldsymbol{T}_{\text{tn}}^{\text{b}}, \boldsymbol{q})$ returns $c(\boldsymbol{q})$ and $\boldsymbol{q}$ if $\boldsymbol{q} \in C_{\text{adj}}$ or otherwise returns a large cost, $c_{\text{infeasible}}$, and, initial joint configuration, $\boldsymbol{q}_0$. IKCONFIGURATIONLOSS evaluates a nominal robot configuration's dexterity. The nominal configuration is determined by fixing $\mathring{\boldsymbol{q}}$ to the configuration determined by the global optimizer to resolve redundancy and solving for $\tilde{\boldsymbol{q}}$ using $\tilde{\boldsymbol{J}}$ with a gradient-descent-based IK formulation. For CRANE, $\tilde{\boldsymbol{q}} = \{q_1, q_2, q_3, q_4, q_7\}$, $\mathring{\boldsymbol{q}} = \{q_5, q_6\}$, and q_8 is excluded.

IK is implemented following the Levenberg-Marquardt algorithm for stability near singularities $\boldsymbol{J}^{\dagger} = \left(\boldsymbol{J}^{\top}\boldsymbol{J} + \lambda \boldsymbol{I}\right)^{-1} \boldsymbol{J}^{\top}$ with damping term λ. The pose error between two $SE(3)$ poses is calculated as the cartesian position error and axis-angle orientation error between the pose's R_{z} vectors. During the *Solve IK* portion of IKCONFIGURATIONLOSS, a nominal IK solution is found for $\tilde{\boldsymbol{q}}$ with $\tilde{\boldsymbol{J}}$, providing a full robot configuration, $\boldsymbol{q}$, when combined with $\mathring{\boldsymbol{q}}$ from the general-purpose global optimization algorithm.

During *Evaluate Adjustability* of IKCONFIGURATIONLOSS, the nominal joint configuration is evaluated for RCM adjustability as defined in Eq. (4.12). CALCLOCALTARGETS$(\cdot)$ creates a set of adjustable angle target poses X_{adj} around $\boldsymbol{T}_{\text{tn}}^{\text{b}}$ satisfying the RCM constraint by rotating the nominal insertion pose. During this evaluation, the full Jacobian, $\boldsymbol{J}$, is used with a nullspace objective to remain near the previously determined nominal robot configuration. For each step of the gradient-descent, $\boldsymbol{q}_{\text{local}}$ is evaluated for if it remains within $\mathcal{C}_{\text{feas}}$. This evaluation implicitly checks the path between $\boldsymbol{T}_{\text{target}}$ and $\boldsymbol{T}_{\text{local}}$ is collision-free due to the limited step

size of the gradient step. $c_{\text{infeasible}}$ specified as a large value for in-collision configurations and is selected sufficiently large that it is greater than any cost from $c(\boldsymbol{q})$. Depending on the cost function weighting, different robot configurations are optimal (Fig. 4.2).

Algorithm 1: IKConfigurationLoss

Input: $\boldsymbol{T}_{tar}$: Target Needle Insertion transform, $\boldsymbol{q}_0$: initial oint configuration

Parameters: $c(\cdot)$: cost function for a configuration; FK$(\cdot)$: forward kinematics function; $\boldsymbol{J}(\cdot)$: space Jacobian ; $\tilde{\boldsymbol{J}}(\cdot)$: non-redundant space Jacobian; ε_p: position error tolerance for IK solution; ε_o: orientation error tolerance for IK solution; $\boldsymbol{K}_{\text{e}}$ end-effector task gain matrix; $\boldsymbol{K}_{\text{c}}$ null-space task gain matrix

Output: IK configuration loss $c(\boldsymbol{q})$, IK configuration $\boldsymbol{q}$

// Solve IK

$\boldsymbol{q} \leftarrow \boldsymbol{q}_0$

do

  $\boldsymbol{e} \leftarrow \begin{bmatrix} \boldsymbol{d}_{\text{p}}(\boldsymbol{T}_{tar}, \text{FK}(\boldsymbol{q})) & \boldsymbol{d}_{\text{o}}(\boldsymbol{T}_{tar}, \text{FK}(\boldsymbol{q})) \end{bmatrix}^{\top}$

  $\tilde{\boldsymbol{q}} \leftarrow \tilde{\boldsymbol{q}} + \tilde{\boldsymbol{J}}^{\dagger} \boldsymbol{K}_{\text{e}} \boldsymbol{e}$

while $\left\| e_p \right\|_2 > \varepsilon_p$ *and* $\| e_o \|_2 > \varepsilon_o$

// Evaluate adjustability

if $\boldsymbol{q} \notin C_{free}$ **then return** $c_{infeasible}$, $\boldsymbol{q}_0$

$X_{adj} \leftarrow$ CALCLOCALTARGETS$(\boldsymbol{T}_{tar})$

foreach $\boldsymbol{T}_{local} \in X_{adj}$ **do**

  $\boldsymbol{q}_{local} \leftarrow \boldsymbol{q}$

  do

    $\boldsymbol{e} \leftarrow \begin{bmatrix} \boldsymbol{d}_{\text{p}}(\boldsymbol{T}_{local}, \text{FK}(\boldsymbol{q})) & \boldsymbol{d}_{\text{o}}(\boldsymbol{T}_{local}, \text{FK}(\boldsymbol{q})) \end{bmatrix}^{\top}$

    $\boldsymbol{q}_{local} \leftarrow \boldsymbol{q}_{local} + \boldsymbol{J}^{\dagger} \boldsymbol{K}_{\text{e}} \boldsymbol{e} + (I - \boldsymbol{J}^{\dagger} \boldsymbol{J}) \boldsymbol{K}_{\text{c}} (\boldsymbol{q} - \boldsymbol{q}_{local})$

    if $\boldsymbol{q}_{local} \notin C_{feas}$ **then return** $c_{infeasible}$, $\boldsymbol{q}_0$

  while $\left\| \boldsymbol{e}_p \right\|_2 > \varepsilon_p$ *and* $\| \boldsymbol{e}_o \|_2 > \varepsilon_o$

return $c(\boldsymbol{q})$, $\boldsymbol{q}$

Local Controller

The local controller minimizes the distance between $\boldsymbol{T}_{\text{tn}}^{\text{b}}$ and estimated EE pose, $\hat{\boldsymbol{T}}_{\text{EE}}^{\text{b}}$, calculated from the measured tip-mounted magnetic tracker's pose for feedback to compensate

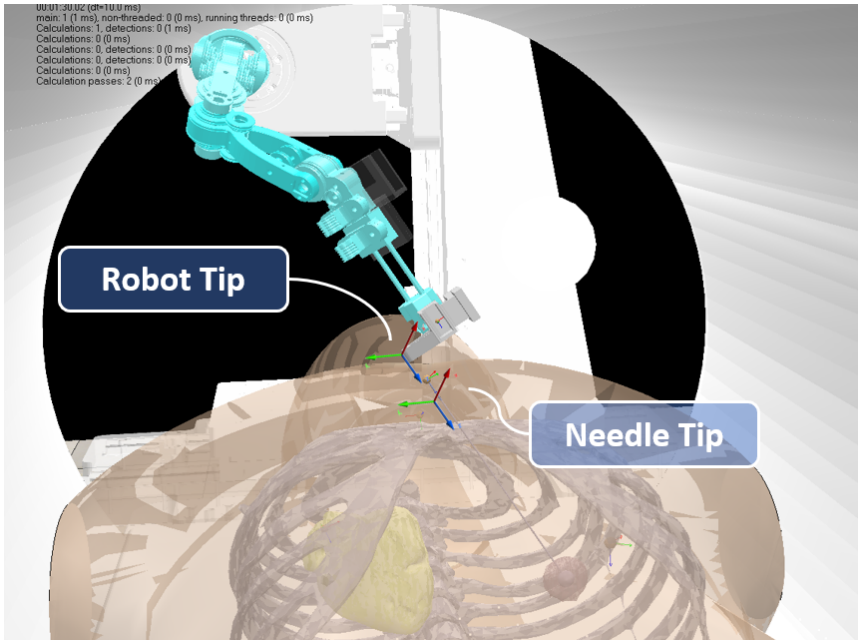

(a) Prioritized patient avoidance, $\beta < 0.5$

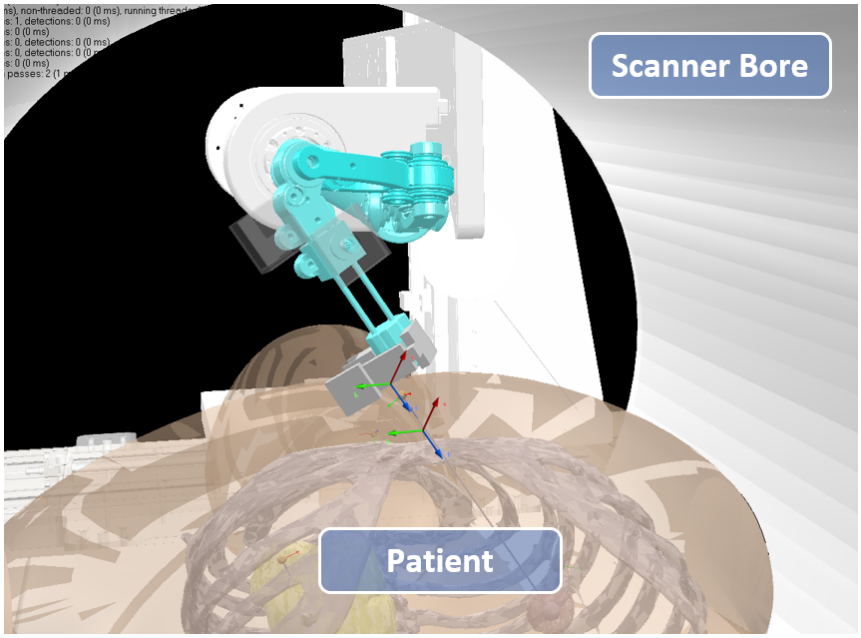

(b) Equal priority patient and scanner avoidance, $\beta \approxeq 0.5$

Figure 4.2: Solution of multiple joint configurations for a $\boldsymbol{T}^{\mathrm{b}}_{\mathrm{tn}}$ based on optimization weights and utilizing CRANE's redundant in-bore joints. CRANE provides multiple solutions for a Target Needle Insertion pose, considering physician preferences on obstacle avoidance while ensuring a well-conditioned dexterous solution.

for system mechanical deflection (described in Sect. 3.2.2). This is calculated as:

$$\hat{\boldsymbol{T}}^{\mathrm{b}}_{\mathrm{EE}} = \boldsymbol{T}^{\mathrm{b}}_{\mathrm{mb}} \boldsymbol{T}^{\mathrm{mb}}_{\mathrm{mtrkt}} \boldsymbol{T}^{\mathrm{trk}}_{\mathrm{EE}} \tag{4.17}$$

Algorithm 2: calcLocalTargets

Input: $\boldsymbol{T}_{\text{nom}}$: nominal transform $\in SE(3)$

Parameters: Δ_{zenith}: max zenith angle off nominal insertion axis for adjustability evaluation; N: number of target vectors to evaluate in radial direction; M: number of target vectors to evaluate in the zenith direction

Output: $\boldsymbol{X}_{\text{adj}} \in SE(3) \times NM$: target poses for adjustability evaluation

$\Delta\boldsymbol{R}_{zenith} \leftarrow \text{ROTMAT}(x, \Delta_{\text{zenith}}/M)$
$\Delta\boldsymbol{R}_{radial} \leftarrow \text{ROTMAT}(z, 2\pi/N)$
$\boldsymbol{X}_{\text{adj}} \leftarrow \emptyset$
$\boldsymbol{T}_{\text{local}} \leftarrow T_{\text{nom}}$ **for** $i = 1$ *to* N **do**
    $\boldsymbol{R}_{\text{local}} \leftarrow \Delta\boldsymbol{R}_{zenith}\boldsymbol{R}_{\text{local}}$
    $\boldsymbol{X}_{\text{adj}} \leftarrow \boldsymbol{X}_{\text{adj}} \cup \{\boldsymbol{T}_{\text{local}}\}$
    for $j = 1$ *to* M **do**
        $\boldsymbol{R}_{\text{local}} \leftarrow \Delta\boldsymbol{R}_{radial}\boldsymbol{R}_{\text{local}}$
        $\boldsymbol{X}_{\text{adj}} \leftarrow \boldsymbol{X}_{\text{adj}} \cup \{\boldsymbol{T}_{\text{local}}\}$
return $\boldsymbol{X}_{\text{adj}}$

Additionally, the local controller minimizes the distance between the estimated joint configuration, $\hat{\boldsymbol{q}}$, and $\boldsymbol{q}^*$ via a nullspace controller. Specifically, the joint configuration setpoint, $\boldsymbol{q}_{set}$, is updated following:

$$\boldsymbol{e} \leftarrow \begin{bmatrix} \boldsymbol{d}_{\text{p}}(\boldsymbol{T}^{\text{b}}_{\text{tn}}, \hat{\boldsymbol{T}}^{\text{b}}_{\text{EE}}) & \boldsymbol{d}_{\text{o}}(\boldsymbol{T}^{\text{b}}_{\text{tn}}, \hat{\boldsymbol{T}}^{\text{b}}_{\text{EE}}) \end{bmatrix}^{\top} \tag{4.18}$$

$$\boldsymbol{q}_{\text{set}} \leftarrow \hat{\boldsymbol{q}} + \boldsymbol{J}^{\dagger}\boldsymbol{K}_{\text{e}}\boldsymbol{e} + (\boldsymbol{I} - \boldsymbol{J}^{\dagger}\boldsymbol{J})\boldsymbol{K}_{\text{c}}(\boldsymbol{q}^* - \hat{\boldsymbol{q}}) \tag{4.19}$$

where $\boldsymbol{J}^{\dagger} = \left(\boldsymbol{J}^{\top}\boldsymbol{J} + \lambda\boldsymbol{I}\right)^{-1}\boldsymbol{J}^{\top}$ with damping term λ evaluated at the estimated joint configuration, $\boldsymbol{K}_{\text{c}}$ and $\boldsymbol{K}_{\text{c}}$ are end-effector and null-space task gain matrices, $\hat{\boldsymbol{q}}$, the target pose described by $\boldsymbol{T}^{\text{b}}_{\text{EE}}$ defined above and with $\boldsymbol{T}^{\text{b}}_{\text{tn}}$ provided from the User Interface. The estimated joint configuration, $\hat{\boldsymbol{q}}$, is described in the following section.

Robot Joint Control

The robots joint configuration estimate, $\hat{\boldsymbol{q}} = \begin{bmatrix} \hat{\boldsymbol{q}}_\mathrm{b} & \hat{\boldsymbol{q}}_\mathrm{c} \end{bmatrix}^\top$, is calculated as:

$$\hat{\boldsymbol{q}} \leftarrow \begin{bmatrix} \boldsymbol{M}_\mathrm{b}\boldsymbol{\theta}_\mathrm{b} \\ \alpha \boldsymbol{M}_\mathrm{c}\dot{\boldsymbol{\theta}}_\mathrm{c}\Delta T + (1-a)\tilde{\boldsymbol{q}}_\mathrm{c} \end{bmatrix} \tag{4.20}$$

for motor position, $\boldsymbol{\theta}$, motor velocity $\dot{\boldsymbol{\theta}}$, sampling time, ΔT, and weighting parameter, α, setting the complementary filter's changeover frequency. The base joint positions $\boldsymbol{q}_\mathrm{b}$ are calculated based on the gear ratios and can be directly used for control due to the transmission's high stiffness. The in-bore cable-driven joint configuration, $\hat{\boldsymbol{q}}_\mathrm{c}$, is estimated using a complementary filter between the joint mounted magnetic encoders (AMS AS5048B), $\tilde{\boldsymbol{q}}_\mathrm{c}$, and motor's velocity, $\dot{\boldsymbol{\theta}}_\mathrm{c}$, (Maxon ENX encoder, Maxon ESCON 50/5) to compensate for errors in the coupling relations $\boldsymbol{M}_\mathrm{c}$ due to the cable transmission's stretch and hysteresis, and the joint encoder's noisy readings.

Motor torque setpoints, $\boldsymbol{\tau}_\mathrm{set}$, are calculated based on the error between the target joint configuration, $\boldsymbol{q}_\mathrm{set}$, and the current joint configuration estimate, $\hat{\boldsymbol{q}}$, as:

$$\boldsymbol{\tau}_{set} = \left(\boldsymbol{K}_\mathrm{p} + \boldsymbol{K}_\mathrm{d}\frac{d}{dt} \right) \boldsymbol{M}^{-1} \left(\boldsymbol{q}_\mathrm{set} - \hat{\boldsymbol{q}} \right) \tag{4.21}$$

where $\boldsymbol{K}_\mathrm{p}$ and $\boldsymbol{K}_\mathrm{d}$ are the actuator-space proportional and derivative gains.

4.1.3 Experiments

Simulated Dexterity Analysis

CRANE's kinematic and static dexterity is evaluated across several simulated environments. This analysis enables the evaluation of kinematic designs for in-bore surgical manipulation considering the limited space and variety of patient body habitus and insertion points that may be encountered clinically. Two environment styles are tested: retrospective clinical cases for

needle biopsy in a scanner and comprehensive simulated cases. CoppelliaSim [RSF13b] with PyRep [JFD19] bindings provides distance-to-collision, $d_B(\cdot)$, calculations.

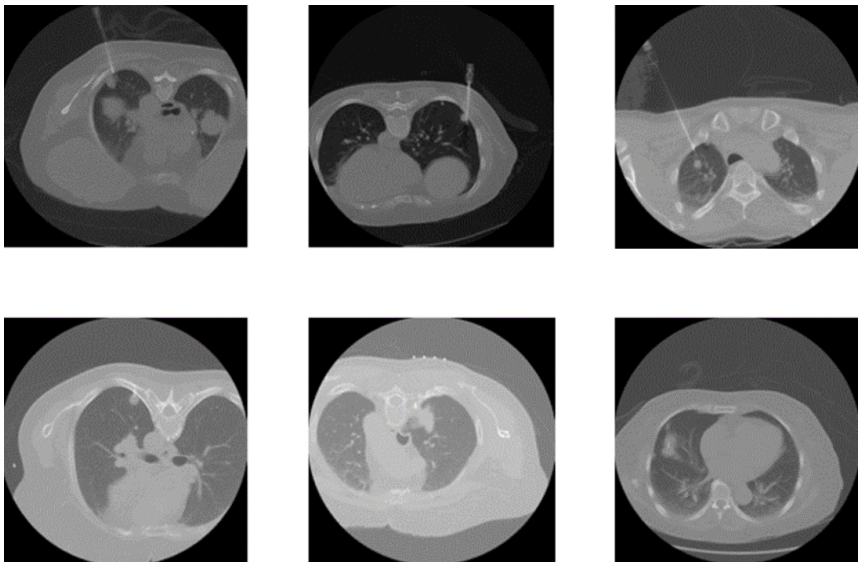

(a) CT scans of clinical cases

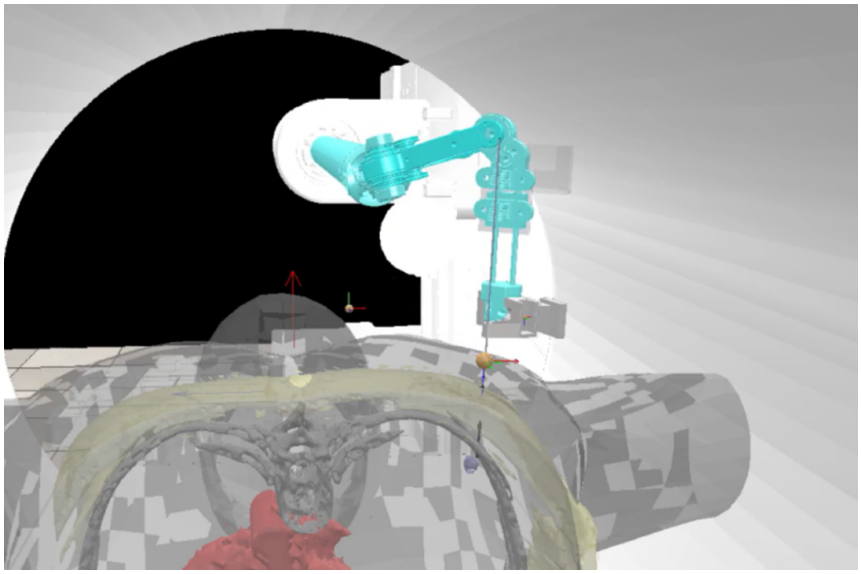

(b) Simulated Case Environment

Figure 4.3: Six clinical cases DICOM scans are used for retrospective dexterity analysis by creating a virtual reconstruction of the procedures within a virtual environment. (a) shows single axial CT slices of each clinical case with needle inserted. Several needle insertion trajectories are out-of-plane providing limited visability in the slice. (b) shows a single representative setup of 3D CT scanner room with the patient placed in bore and robot reaching the target needle insertion pose performed by the physician and determined from the CT scan. The patient body is filled in based on height and weight information combined with direct mesh matching. CRANE has sufficient workspace and dexterity to perform these clinical cases matching the needle insertion performed by a physician.

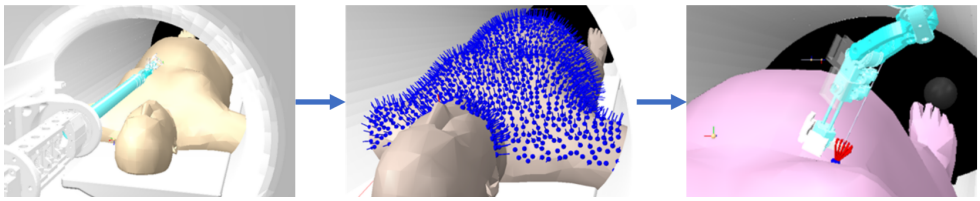

(a) Workflow for comprehensive evaluation

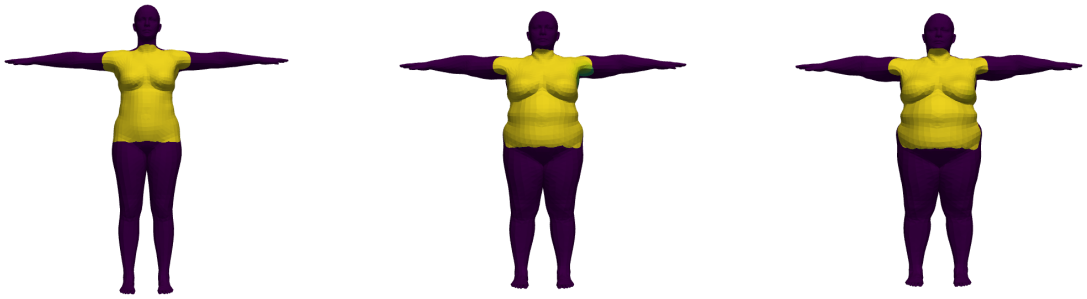

(b) Female, +0σ (c) Female, +1.5σ (d) Female, +3σ

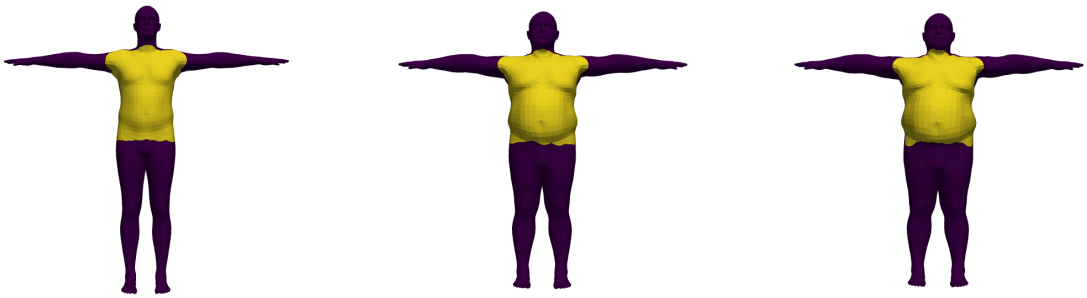

(e) Male, +0σ (f) Male, +1.5σ (g) Male, +3σ

Figure 4.4: (a) shows the evaluation workflow. An environment (including the robot, an imaging bore, and a target patient) is setup. Visible vertices areas are selected as candidate needle insertion positions with the nominal trajectory specified as the vertex normal and additional nearby orientations around the nominal normal vector. (b-g) show results of evaluation of robot dexterity across multiple generated human morphologies. Bright areas denote high dexterity, while darker areas denote low dexterity. CRANE provides high dexterity across a wide variety of patient sizes and is able to reach across the abdominal and thoracic regions even in substantial body habitus patients.

Retrospective Clinical Cases The volumetric CT scans (DICOM format) of six transthoracic CT lung biopsy cases (Fig. 4.3) from UCSD Health were segmented and integrated into a CoppeliaSim environment. The environment consists of collision meshes, $\mathcal{B} = \{\text{robot, scanner bore, patient body}\}$, and $\boldsymbol{T}_{\text{tn}}^{\text{sb}}$. Furthermore, a synthetic patient body is generated using STAR [OBB20] based on the patient's body habitus to fill in the portion of the patient's body not visible in the clinical scan.

This experiment evaluates the system's ability to reach $\boldsymbol{T}_{\text{tn}}^{\text{sb}}$ for the Automated Device Setup method, while satisfying the prerequisite optimization constraints. $\boldsymbol{T}_{\text{tn}}^{\text{sb}}$ is attached to the

segmented patient body which is placed within the scanner such the the DICOM's isocenter aligns with the scanner bore's isocenter. An individual $\boldsymbol{T}_{\text{tn}}^{\text{sb}} \in \mathcal{X}_{\text{adj}}$ is REACHABLE if a dexterous configuration was found by the Automated Device Setup method and determined by $c(\boldsymbol{q}^*) < c_{\text{infeasible}}$. All six retrospective cases were reachable. This illustrates CRANE's ability to automatically setup for dexterous needle insertion within a clinical environment.

Comprehensive Simulated Clinical Cases Motivated by the retrospective clinical cases, a comprehensive test was created to enable the general purpose evaluation of an in-bore needle insertion robot's dexterity. Different sizes of human bodies were generated using STAR [OBB20] to $+3/-0\sigma$ BMI for U.S. males and females. Larger patients result in less in-bore space and a more challenging environment. These human bodies are placed within the scanner bore following the procedure described above in Sect. 4.1.3. This test results in visual plots of a robot's ability to dexterously insert needles across a variety of patient bodies at various angles.

For each environment's human body mesh $\in \mathcal{B}$, a set of $\boldsymbol{T}_{\text{tn}}^{\text{sb}}$, $\mathcal{X}$, is created from the mesh vertices and surface normals, $\{\mathbb{V},\ \mathbb{N}\}$, of the simulated patient; defined as:

$$\begin{aligned} \mathcal{X} = \{\boldsymbol{T} | \boldsymbol{t} = \mathbb{v},\ \boldsymbol{R} = \text{ROTMAT}(\delta, \xi) \\ \forall \{\mathbb{v},\ \mathbb{n}\} \in \{\mathbb{V},\ \mathbb{N}\} \end{aligned} \tag{4.22}$$

where $\delta = \mathbb{n} \times z$ and $\xi = \cos^{-1}\left(\frac{\mathbb{n}^\top z}{\|\mathbb{n}\|_2 \|z\|_2}\right)$ and z is the Z-axis unit vector. Physicians typically insert needles in an orthogonal fashion to the patient's skin to prevent slipping and needle bending from tissue boundary layers. Therefore, the surface normal vector is used as a the nominal insertion vector. However, off-normal insertions are also performed clinically. Therefore, off-normal insertion angles are additionally evaluated around the nominal surface normal (shown in Fig. 4.4), providing a set of insertion poses for an individual vertex connected pose $\boldsymbol{T} \in \mathcal{X}$ as:

$$\mathcal{X}_{\text{adj}} = \text{CALCLOCALTARGETS}(\boldsymbol{T},\ 15^\circ,\ 15,\ 15) \tag{4.23}$$

Given this set of Target Needle Insertion points for a single vertex, $\mathbb{v}$, the robot's ability to perform the insertion dexterously is evaluated using the Automated Device Setup method (described in Sect. 4.1) and returning $\boldsymbol{q}$. An individual $\boldsymbol{T}_{\text{tn}}^{\text{sb}} \in \mathcal{X}_{\text{adj}}$ is REACHABLE if a dexterous configuration was found by the Automated Device Setup method and determined by $c(\boldsymbol{q}^*) < c_{\text{infeasible}}$.

As shown in Fig. 4.4, CRANE can dexterously insert needles across patients with a wide variety of body sizes and morphology. Large patients decrease the accessible dexterous region and are primarily limited by the length of the robot's final EE insertion axis, shorter than many needles used during clinical procedures and therefore not a significant limitation. This test shows that CRANE's low profile design and the redundant kinematic chain enable the dexterous insertion of a needle for clinical cases.

Needle Insertion Experiment

Multiple needle insertions were performed using CRANE on a custom lung phantom based on a preoperative CT scan from which $\boldsymbol{T}_{\text{tn}}^{\text{sb}}$ and environment obstacles, $\mathbb{B}$ are constructed. The custom lung phantom comprises a resin plastic rib cage, a preserved and dry pig lung, and multiple flexible polymers approximating skin, fat, and tumors. The experimental setup is shown in Fig. 3.2. A preoperative scan is performed from which $\boldsymbol{T}_{\text{tn}}^{\text{sb}}$ and environment obstacles, $\mathbb{B}$ are created, and a collision-free motion plan, $\boldsymbol{Q}$, from the initial robot configuration $\boldsymbol{q}_{\text{start}}$ to $\boldsymbol{q}^*$ is calculated and executed within a virtual imaging bore (70cm diameter). The needle is inserted to the tumor, and a post-operative scan is performed. The phantom body segmentation is determined using the Marching Cubes algorithm [LC87a] with a threshold of $-200HU$ and a model of the CT scanner bore. Three tests were performed using different $\boldsymbol{T}_{\text{tn}}^{\text{sb}}$ towards a single tumor within the phantom (resulting scans shown in Fig. 4.5). Table 4.3 shows the results from this experiment which achieved high accuracy. The Position Error and Angle Error are calculated as the L2 norm of the position and orientation components of the position and orientation error between between the $\boldsymbol{T}_{\text{tn}}^{\text{sb}}$ and $\boldsymbol{T}_{\text{EE}}^{\text{sb}}$ as defined in Eq. 4.18. $\boldsymbol{T}_{\text{EE}}^{\text{sb}}$ is manually determined from the post-operative scan

using 3DSlicer [FBKC+12].

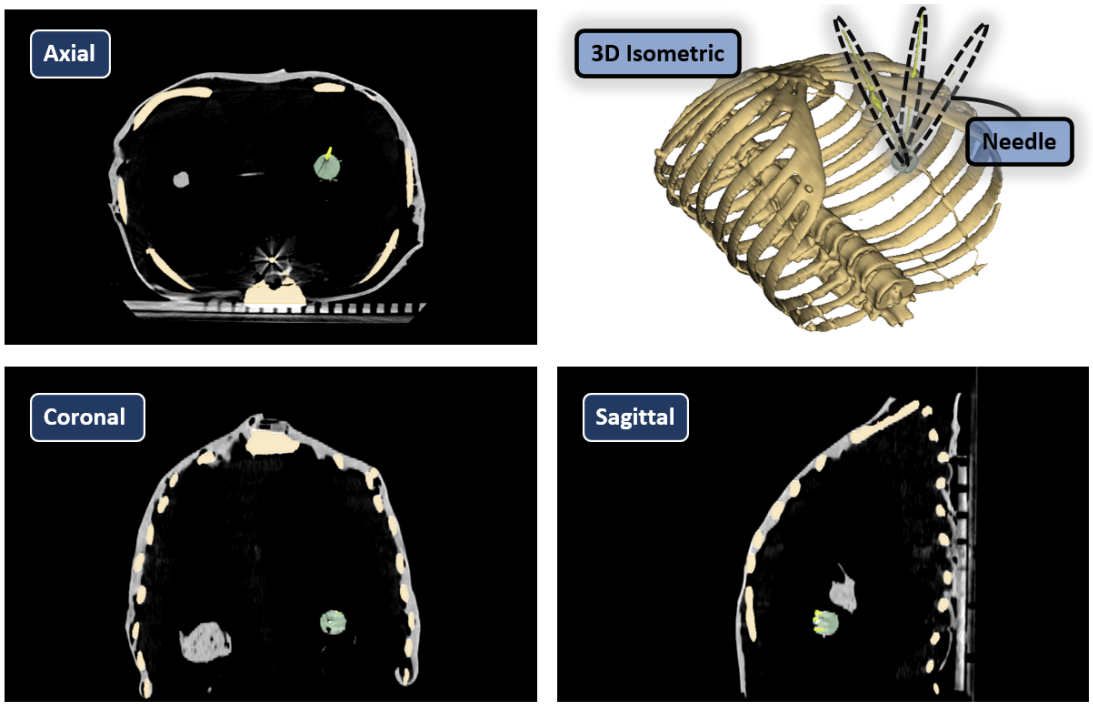

Figure 4.5: This figure shows multiple visualizations of a post-operative CT scan of the phantom following the "single-shot" needle insertion to evaluate the system and automatic setup technique's accuracy and efficacy without intermediate control scans. The scan was segmented to highlight the bone (dark yellow), tumor (green), and needle (light yellow). All three needles intersect the target, demonstrating the feasibility of the single-shot approach.

Table 4.3: Accuracy results from automated single-shot needle insertion illustrating high accuracy for a full depth needle insertion with single planning scan

	Trajectory 1	Trajectory 2	Trajectory 3
Angle RMSE (deg)	2.0	1.8	1.9
Position RMSE (mm)	3.4	2.4	3.8

4.2 Image Feedback Control

When performing image-guided surgery, physicians determine the trajectory in image space, then relate the trajectory to the physical space in which they manipulate the needle. Physicians typically alternate between scanning the patient and advancing the needle. They may

adjust the needle's pose between scans to improve targeting. There are two main components: image-world registration and control law for adjusting the needle.

Here, we perform tracking and closed-loop control within a Computed Tomography (CT) scanner's image frame on our CT needle insertion robot [SYJ+22]. The needle is incrementally advanced with intermediate CT control scans and robot adjustments to minimize the needle base pose error determined with image-space tracking. This section consists of the following primary components:

1. Closed-loop robot end-effector control based on CT image frame error determined from automatically tracked Coordinate Reference Frames (CRFs) attached to the robot

2. Experiments evaluating guidance method and system level performance in-situ

Our previous work uses a manual pre-operative scanner-device calibration, automatically creates a dexterous path plan, and then performs a "single-shot" full-depth insertion without incremental control scans. The closed-loop approach resolves the potential pre-operative alignment and robot end-effector tracking error, and automated fiducial tracing improves accuracy while decreasing procedure time and the likelihood of human errors [ŠŠJ+17, Ins, LCP+14]. This tracking method, procedure setup, and closed-loop control method are described in the following sub-sections.

4.2.1 Tracking Method

CRFs are sets of fiducials attached to a rigid body that enable pose tracking. A CRF is attached to the robot base and another CRF is attached to the robot's EE (labeled in Fig. 4.7). Both CRFs are automatically localized within the CT scanner. Each of our CRFs comprises four high Hounsfield Unit (HU) spherical fiducials (Beekley CT-SPOT 120) attached to a rigid body with known geometry. The fiducials have a high Hounsfield Unit (HU) value of $5000HU$, allowing thresholding-based segmentation from the environment.The CT tracking method uses a

CT scan as input and provides the CRF's pose in the scanner frame, $\hat{\boldsymbol{T}}^{\text{sb}}_{\text{marker}} \in SE(3)$, as output. The method comprises three steps (corresponding to Fig. 4.6):

1. Surface Extraction
2. Fiducial Recognition
3. Marker Transform Calculation

The rigid body CRF tracking algorithm is implemented in Python using SimpleITK [LCIB13, YLJB18], scikit-image [Sci], and Open3D [ZPK18] libraries.

Given a CT scan volume in DICOM format, a mesh, $\boldsymbol{B}$, is created via the Marching Cubes algorithm [LC87b] with a threshold of $HU3000$. The Marching Cubes algorithm provides direct 3D segmentation of the environment with sub-pixel localization. The $3000HU$ threshold is selected to provide separability between fiducials and the environment. $\boldsymbol{B}$ comprises vertices, $\boldsymbol{V}$, and edges, $\boldsymbol{E}$. $\boldsymbol{B}$ is clustered into sub-meshes $\boldsymbol{B}_i$ based on edge-connectivity via Open3D's CLUSTER_CONNECTED_TRIANGLES. For each sub-mesh $\boldsymbol{B}_i \in \boldsymbol{B}$, a sphere is fit to its vertices $\boldsymbol{V}_i$ to minimize the least-squares error (shown in Fig. 4.6d), defined as:

$$\text{FIDUCIALFITRMSE} = \min_{\boldsymbol{x},r} \sum_{j=0}^{N} \left| r - \left|\left| \boldsymbol{x} - \boldsymbol{V}_{i,j} \right|\right|_2 \right| \tag{4.24}$$

where $\boldsymbol{x}$ and r respectively denote the center and radius of the of the fit sphere, and $\boldsymbol{V}_{i,j} = \begin{bmatrix} x & y & z \end{bmatrix}$ are the vertices from the sub-mesh [Coo93]. Sub-meshes within a diameter tolerance, $|\boldsymbol{d} - \boldsymbol{d}_{\text{nom}} < \varepsilon_{\text{d}}|$, and of sufficient fit quality, $\text{FIDUCIALFITRMSE} < \varepsilon_{\text{s}}$ are recognized as candidate fiducials. The $3000HU$ segmentation with our fiducial threshold results in a $\boldsymbol{d}_{\text{nom}} = 3mm$, $\varepsilon_{\text{d}} = 0.5mm$ and $\varepsilon_{\text{s}} = 0.25mm$. The center coordinates of these candidate fiducials are stored as a set, $\boldsymbol{F}_{\text{candidate}} \in \mathbb{R}^{N\times 3}$, for transform calculation, where N is the total number of candidate fiducials found in the CT volume. Each CRF's pose, $\hat{\boldsymbol{T}}^{\text{sb}}_{\text{EE}}$ and $\hat{\boldsymbol{T}}^{\text{sb}}_{\text{b}}$, is determined by solving the simultaneous pose and correspondence point-set registration problem to determine a rigid body

transform and correspondence from the known CRF geometry $\boldsymbol{F}_{\text{known}} \in \mathbb{R}^{M\times 3}$ to the tracked locations $\boldsymbol{F}_{\text{candidate}}$ which minimizes a least squares error. $\boldsymbol{F}_{\text{known}}$ are the coordinates of the spheres within the marker based on its design. M is the number of fiducials in a rigid body marker. This transform is determined using the random sample consensus (RANSAC) algorithm [FB81] and the Fiducial Registration Error (FRE) [Fit10, FWM98, Fit09] quality-of-fit metric. RANSAC provides robust fitting with tolerance to outliers. Within each iteration of the RANSAC algorithm, several candidate fiducial center coordinates are randomly sampled $\boldsymbol{F}_{\text{sample}}$ from $\boldsymbol{F}_{\text{known}}$. The transform $\boldsymbol{T}_{\text{t}}^{\text{b}}$ which minimizes the FRE is determined between $\boldsymbol{F}_{\text{known}}$ and $\boldsymbol{F}_{\text{sample}}$ [AHB87]:

$$\min_{\boldsymbol{T}_{\text{t}}^{\text{b}} \in SE(3)} \frac{1}{M} \sum_{i=0}^{M} \left|\left| \hat{\boldsymbol{P}}_i - \boldsymbol{T}_{\text{t}}^{\text{b}} \boldsymbol{P}_i \right|\right|_2 \tag{4.25}$$

where $\boldsymbol{T}_{\text{t}}^{\text{b}}$ is the transform between robot base frame and the target base frame. $\boldsymbol{P} = \{\boldsymbol{p}_0, \ldots, \boldsymbol{p}_M\}$ and $\hat{\boldsymbol{P}} = \{\hat{\boldsymbol{p}}_0, \ldots, \hat{\boldsymbol{p}}_M\}$ are the augmented Cartesian coordinates from $\boldsymbol{F}_{\text{known}}$ and $\boldsymbol{F}_{\text{sample}}$ and $\boldsymbol{p}, \hat{\boldsymbol{p}} = \begin{bmatrix} x & y & z & 1 \end{bmatrix}^\top$. RANSAC terminates after $10e4$ iterations or if FRE $< 0.25mm$.

4.2.2 Procedure Setup

We perform an initial preoperative scan CT scan for the robot to scanner calibration and environment understanding. The CT scanner provides volumetric images of the environment and is used for tracking the robot. From this scan, the robot base pose, $\hat{\boldsymbol{T}}_{\text{b}}^{\text{sb}}$, and the robot end-effector pose, $\hat{\boldsymbol{T}}_{\text{EE}}^{\text{sb}}$, are directly tracked based in the scanner frame using CRFs following the procedure described Section 4.2.1. Using this initial scan, the user provides the Target Needle Insertion pose $\boldsymbol{T}_{\text{tn}}^{\text{sb}}$. We calculate the Target Needle Insertion pose relative to the robot's base frame $\boldsymbol{T}_{\text{tn}}^{\text{b}}$ as:

$$\boldsymbol{T}_{\text{tn}}^{\text{b}} = \left(\hat{\boldsymbol{T}}_{\text{b}}^{\text{sb}}\right)^{\text{-1}} \boldsymbol{T}_{\text{tn}}^{\text{sb}} \tag{4.26}$$

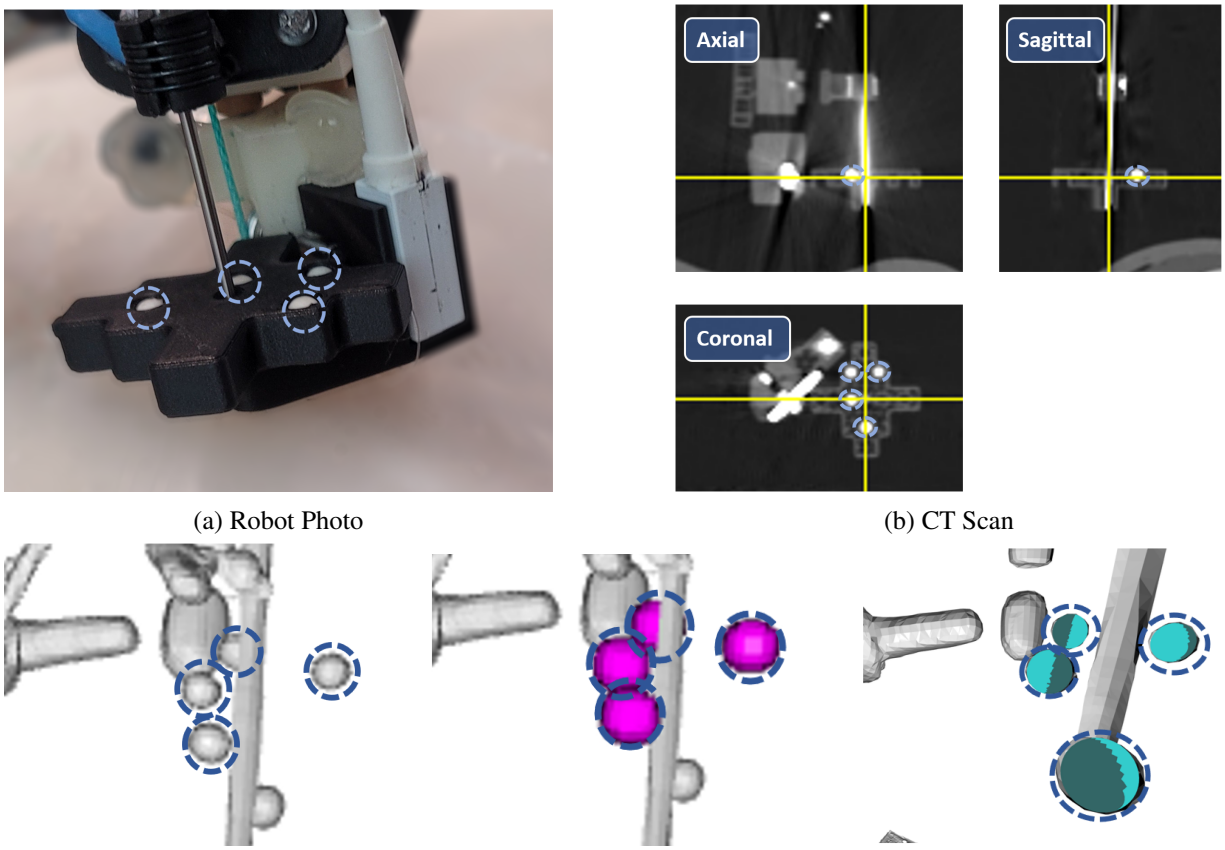

(a) Robot Photo (b) CT Scan

(c) Surface Extraction (d) Fiducial Recognition (e) Marker Transform Calculation

Figure 4.6: CT fiducial tracking enables robot control within the image space. An example workflow with the intermediate steps for tracking CRF attached to the robot end-effector is shown here. (a) shows the physical CRF, while (b) shows a CT scan view of the CRF. The CT scan includes coverage of the fiducial marker from which the (c) surfaces are extracted. The fiducials candidates are individually recognized using a sphere fitting algorithm (d) from which fiducials are clustered, and the marker is tracked (e). (e) shows the tracked and reprojected fiducials (in light and dark blue) with significant overlap demonstrating minimal FRE. The fiducials are highlighted in each sub-figure with dashed blue circles.

This defines the initial target EE pose for the robot's internal EE controller, $\boldsymbol{T}^{\mathrm{b}}_{\mathrm{tEE}}$:

$$\boldsymbol{T}^{\mathrm{b}}_{\mathrm{tEE}} \leftarrow \hat{\boldsymbol{T}}^{\mathrm{b}}_{\mathrm{tn}} \tag{4.27}$$

The robot is setup to $\boldsymbol{T}^{\mathrm{b}}_{\mathrm{tEE}}$. This defines the robot's initial end-effector target within its coordinate system.

4.2.3 Closed-loop Control

The closed-loop control method minimizes the distance between $\hat{\boldsymbol{T}}^{\mathrm{b}}_{\mathrm{tn}}$ and $\hat{\boldsymbol{T}}^{\mathrm{b}}_{\mathrm{EE}}$ by updating $\boldsymbol{T}^{\mathrm{b}}_{\mathrm{tEE}}$. For each step of the closed-loop method, a CT scan is performed. From this scan, $\hat{\boldsymbol{T}}^{\mathrm{sb}}_{\mathrm{b}}$ and $\hat{\boldsymbol{T}}^{\mathrm{sb}}_{\mathrm{EE}}$ are directly tracked using robot mounted rigid body fiducials. The tracked EE pose relative to the robot's base frame $\hat{\boldsymbol{T}}^{\mathrm{b}}_{\mathrm{EE}}$ is calculated:

$$\hat{\boldsymbol{T}}^{\mathrm{b}}_{\mathrm{EE}} = \left(\hat{\boldsymbol{T}}^{\mathrm{sb}}_{\mathrm{b}}\right)^{-1} \hat{\boldsymbol{T}}^{\mathrm{sb}}_{\mathrm{EE}} \tag{4.28}$$

The end-effector pose error transform ${}^{\mathrm{b}}\hat{\boldsymbol{T}}^{\mathrm{EE}}_{\mathrm{tn}}$ in the robots base frame is calculated:

$${}^{\mathrm{b}}\hat{\boldsymbol{T}}^{\mathrm{EE}}_{\mathrm{tn}} = \left(\hat{\boldsymbol{T}}^{\mathrm{b}}_{\mathrm{EE}}\right)^{-1} \hat{\boldsymbol{T}}^{\mathrm{b}}_{\mathrm{tn}} \tag{4.29}$$

From this, the robot's internal end-effector controller's target pose is updated:

$$\hat{\boldsymbol{T}}^{\mathrm{b}}_{\mathrm{tEE}} \leftarrow \boldsymbol{T}^{\mathrm{b}}_{\mathrm{tEE}} \hat{\boldsymbol{T}}^{\mathrm{EE}}_{\mathrm{tn}} \tag{4.30}$$

The user determines whether to perform another iteration of the closed-loop method or conclude the needle insertion. If they perform another iteration, this method is repeated.

4.2.4 Experiments

Testing is performed to evaluate image tracking performance and closed-loop control system performance. The experimental setup (e.g., robotic platform, scanner settings, and interfacing), evaluation metrics, and results are presented below.

We used scan settings of 120 kVp, 200mA, and 0.5-second rotation time on a GE Revolution scanner at UC San Diego's Thornton Pavilion. CT scans in DICOM format are uploaded to our PACS server [WTE+07] and downloaded via the Secure File Transfer Protocol (SFTP). Scan

processing is performed utilizing SimpleITK [YLJB18,LCIB13], Open3D [ZPK18], Numpy [Arr], and scikit-image [Sci] with user interaction through a Jupyter Notebook [KRP+16] following the procedure described in Sect. 4.2.1.

Testing is performed using the multi-DoF CRANE robot (described in Chapter 3) to insert needles into a static lung phantom comprising a plastic rib cage, a preserved and dried pig lung, and multiple tissue layers. High-rate EE feedback control using the Ascension Trackstar magnetic tracker was disabled. An open-loop and closed-loop needle insertion was performed. For both experiments, an initial pre-operative CT scan was performed with the base and EE CRFs in-field. For the open-loop experiment, a single-step of the image-feedback is performed given the calculated EE pose error. Following the initial alignment, the needle is incrementally inserted with intermediate scans to monitor the needle's progression. However, the robot is not controlled to minimize the CRF pose error. For the closed-loop experiment, several steps of the closed-loop image feedback method (described in Sect. 4.2.3) are performed to align $\hat{\boldsymbol{T}}^{\mathrm{b}}_{\mathrm{EE}}$ with $\hat{\boldsymbol{T}}^{\mathrm{b}}_{\mathrm{tn}}$, in free-space prior to insertion. Control is not applied once the needle is inserted into the phantom to prevent the application of torsion and shear on the tissue. For both open-loop and closed-loop approaches, CRANE is controlled such that $\hat{\boldsymbol{T}}^{\mathrm{b}}_{\mathrm{tEE}}$ matches $\hat{\boldsymbol{T}}^{\mathrm{b}}_{\mathrm{tn}}$ (defined in Eq. 4.27). FRE and EE Pose Error [TTP+11,ISO00] are evaluated for each scan. FRE is calculated following Eq. 4.25. EE position and orientation error are calculated as $d_p(\hat{\boldsymbol{T}}^{\mathrm{b}}_{\mathrm{tn}}, \hat{\boldsymbol{T}}^{\mathrm{b}}_{\mathrm{tEE}})$ and $d_o(\hat{\boldsymbol{T}}^{\mathrm{b}}_{\mathrm{tn}}, \hat{\boldsymbol{T}}^{\mathrm{b}}_{\mathrm{tEE}})$ (defined in Eq. 4.8 and Eq. 4.8), respectively.

FRE results for all scans are presented in Fig. 4.8, showing low error and variance. All FRE errors are below scan voxel resolution, demonstrating sub-voxel localization accuracy for the tracking method and accurate manufacturing of the CRF. During the open-loop insertion, a single adjustment based on the image error is applied as the EE CRF is visible in frame. During closed-loop control (following Sect. 4.2.3), the end-effector error (Eq. 4.29) decreased when image-based feedback control was applied (shown in Table 4.4). During insertion, CRF error increase is minor. Fig. 4.9 shows final CT scan slices highlighting the needle tip for both the

closed-loop and open-loop insertion. The needle tip deviation from the tumor's center is 7.2*mm* and 24.2*mm* for the closed-loop and open-loop insertions. However, as $\boldsymbol{T}_{\text{tn}}^{\text{sb}}$ was not specified to intersect the tumor's center, this is may not be a true representation of the methods accuracy. It is noteworthy that the error increases during the needle insertion when control is not applied. This also is a potential source of needle tip positioning error at full insertion depth. The closed-loop control method decreased needle-base pose error prior to and during insertion into the phantom.

Table 4.4: EE pose error, calculated from image-space tracking of CRFs, is significantly lower with the closed-loop method compared with open-loop.

Method	Scan	Description	Position (mm)	Orientation (deg)
Open-loop	0	Setup	102.4	96.9
-	1	Control	17.0	6.5
-	2	Partial Insertion	17.0	6.2
-	3	Full Insertion	17.0	6.4
Closed-loop	0	Setup	100.1	96.8
-	1	Control 1	16.3	6.8
-	2	Control 2	0.3	1.1
-	3	Control 3	0.4	0.3
-	4	Partial Insertion 1	0.7	0.6
-	5	Partial Insertion 2	1.5	0.8
-	6	Full Insertion	2.0	1.0

4.3 Discussion

This chapter presents a framework for automating device setup and control within in-bore image-guided needle insertion procedures. Metrics and requirements for dexterous in-bore needle insertion are defined and applied for device planning, control, and design evaluation. The framework is designed for use with and tested on the CRANE device. This contrasts with previous works in this space and our previous chapters relying on the user to set up and teleoperate the device manually. The presented metrics and method for planning and redundant robot control within an imaging bore can be applied more broadly to other system designs, contributing several

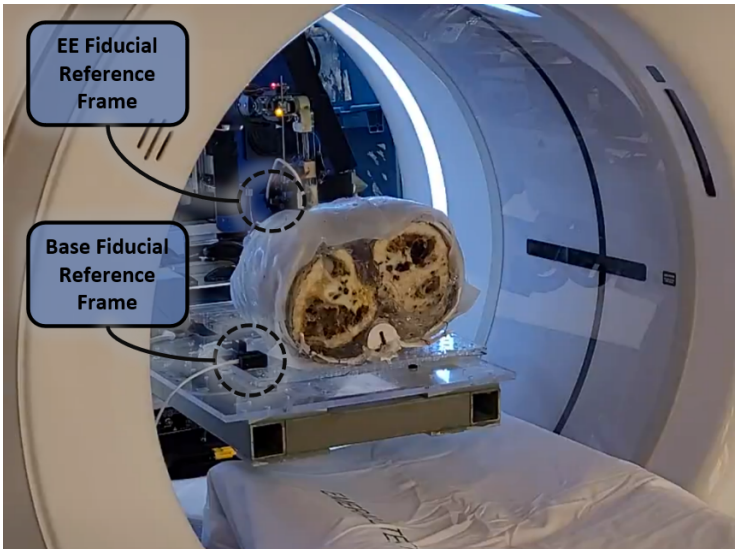

(a) Test setup

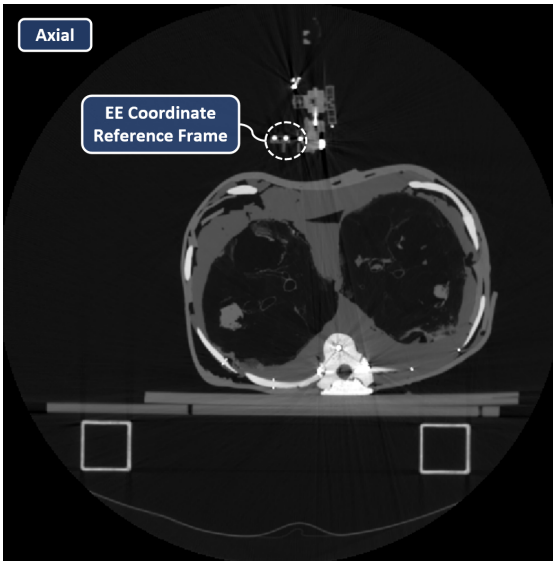

(b) Marker slice

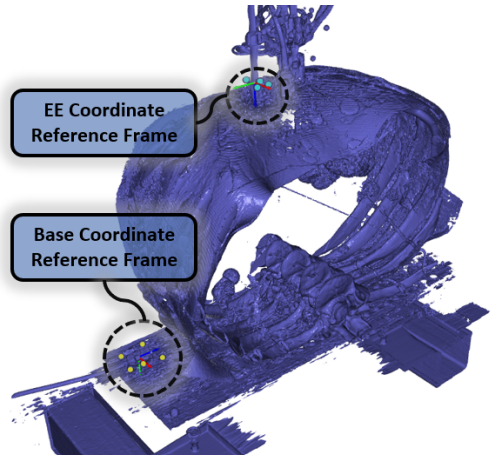

(c) 3D tracking

Figure 4.7: The CT tracking and control method is evaluated in-situ using the CRANE robot. This figure highlights the Base and EE CRFs used for tracking and control within the (a) physical world, (b) CT scanner image, and (c) 3D environment representation. In (b), the Base CRF is not shown as it is within a different axial slice than the EE CRF.

critical considerations for image-guided in-bore robot design. Additionally, a closed-loop CT image-feedback control method is developed and tested in-situ on the CRANE robot. The closed-loop image-feedback method automatically tracks and calculates end-effector pose angles to adjust the robot based on scanner feedback. The method demonstrated minimal image-space

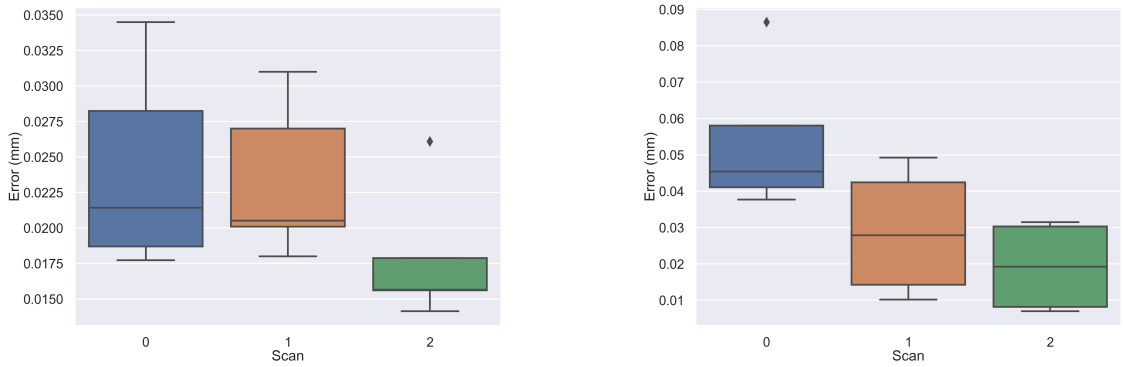

(a) Base Marker, Open Loop

(b) EE Marker, Open Loop

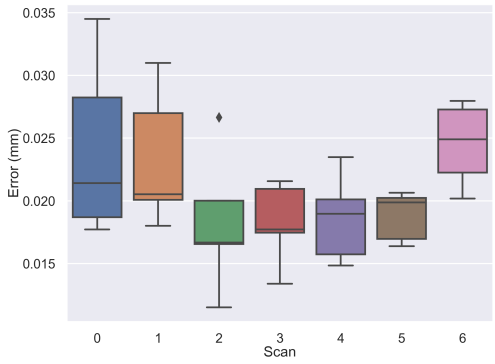

(c) Base Marker, Closed Loop

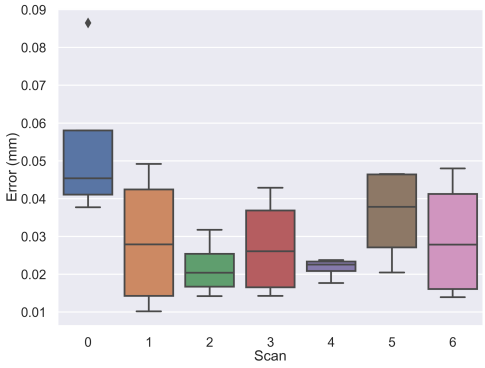

(d) EE Marker, Closed Loop

Figure 4.8: FRE provides an understanding of the tracking accuracy for a CRF. This figure shows FRE for all scans in the open-loop and closed-loop needle insertion experiments. FRE is consistently low at each control scan. This demonstrates that the CRFs are accurately tracked within the scanner throughout our experiments.

fiducial tracking and robot control errors during in-situ evaluation while significantly improving the CRANE system's in-bore accuracy.

4.4 Acknowledgments

Chapter 4, in part, has been submitted for publication of the material as it may appear in IEEE Transactions on Robotics, 2023, D. Schreiber, Z. Yu, T. Henderson, A. Norbash, M. Yip. The dissertation author is the primary author of this paper.

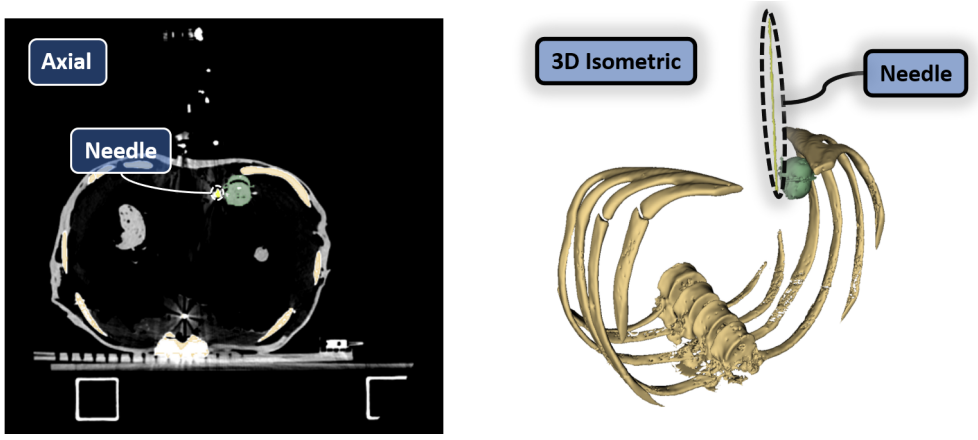

(a) Open-loop

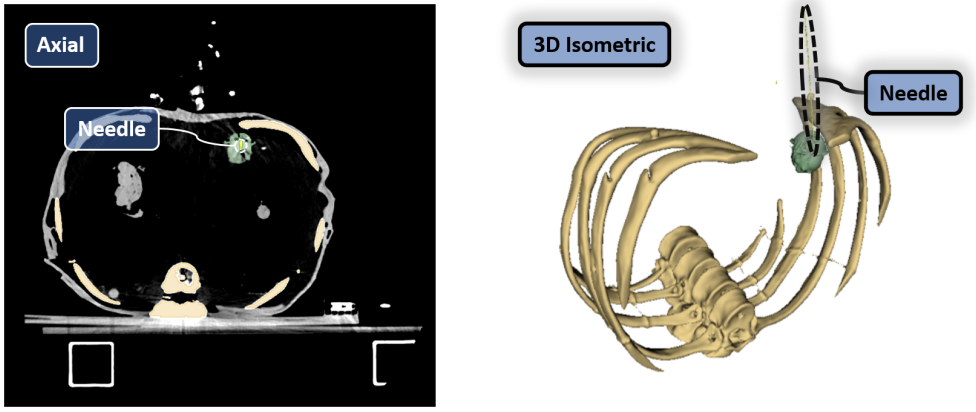

(b) Closed-loop

Figure 4.9: Comparison of needle insertion accuracy using (a) open-loop single-shot insertion without EE pose corrections versus (b) closed-loop EE control. The bone, needle, and tumor are segmented in each slice as dark yellow, bright yellow, and green. The closed-loop method improves device image-space accuracy and enables the needle to reach the tumor. This demonstrates that the closed-loop CT guidance method can correct errors unresolved by the device's underlying controller.

Chapter 5

Conclusion and Future Directions

Computed Tomography (CT) guided biopsies and ablations frequently require multiple needle insertions and repeat procedures, increasing patient risks, costs, and hospital stay lengths. Robots can eliminate the numerous punctures and procedures required while enabling physicians to treat small early-stage cancer via a minimally invasive approach. However, prior robotic platforms have a complex and lengthy setup, limited applicability and large size, imaging artifacts, insufficient accuracy, and limited needle compatibility, limiting their clinical application.

This thesis explored the design and development of systems for robotic in-bore needle procedures. The component technologies for an entirely hands-off in-bore needle insertion are demonstrated.

A kinematic architecture and cable-driven transmission design is introduced for dexterous in-bore needle insertion. Using this design, two generations of device design are presented and evaluated both on-benchtop and in-situ. The initial device design focused on CT-guided lung biopsy and served as a proof-of-concept for the transmission design and complete system architecture. Benchtop testing demonstrated low backlash, the device performed well under teleoperation, and the kinematic design with minimal in-bore cross-section afforded a great working range. In-situ testing revealed the design minimized imaging artifacts due to the remotely

placed actuators. The small size and scanner couch mounting also afforded simple device setup and transport. However, it also brought to light several limitations with the prototype: the limited joint ranges and lack of a Z-axis resulted in challenging device setup, the limited travel insertion axis prevented deep needle insertion, and that high accuracy in addition to precision is important to limit the number of scans required for device control.

Based on the lessons-learned, a second-generation device, CRANE, was developed with a broader application goal: general purpose needle-insertion within the abdominal and thoracic region inside a CT scanner. This design provided more extensive joint and axis travel through a scaled and optimized transmission design, the addition of a Z-axis, multi-level closed-loop control to provide high device accuracy, and an infinite travel insertion mechanism achieved via clutching needle insertion. When tested in situ, this resulted in far easier device use. However, a primary limitation is that while the device is fully actuated, setup is still a manual process with the user specifying the nominal configuration and teleoperating the device in robot rather than image space. This is incredibly challenging given the device's redundant joints, requiring user expertise of how to setup the joint to provide a large workspace while avoiding workspace singularities and collision.

Therefore, a planning and control method was introduced to automate device setup and nominal robot configuration for needle insertion to provide high dexterity for clinically relevant metrics. These metrics and this method were applied to both simulated device design evaluation and real-world needle insertion experiments. This approach relied on manual image to robot alignment, which is time-consuming and error prone. Finally, a closed-loop image guidance method was proposed and tested for high image-space accuracy with automatic robot tracking using the scanner and tested in-situ.

The presented approach shows significant promise for future clinical testing, which must be performed. Despite the potential, several critical limitations of the existing robot design and testing must be addressed before clinical use. Limitations of the current robot design include high

system complexity due to parallel electronic interfacing and a large base platform that requires mounting to the floor rather than the scanner couch. Additionally, a more traditional UI for DICOM viewing should be incorporated. Limitations of the current in-situ evaluation include a small study size with a single user and testing within a static environment. Future work will focus on translating this system to clinical testing (e.g., statistical user studies and animal testing) and resolving the above-mentioned limitations.

The work presented in this thesis investigates several points for automated device setup and control for in-bore needle insertion. It will hopefully support the development of more accessible and accurate clinical robotic systems for interventional image-guided surgery.

Bibliography

[AAP+15a] Michele Anzidei, Renato Argirò, Andrea Porfiri, Fabrizio Boni, Marco Anile, Fulvio Zaccagna, Domenico Vitolo, Luca Saba, Alessandro Napoli, Andrea Leonardi, Flavia Longo, Federico Venuta, Mario Bezzi, and Carlo Catalano. Preliminary clinical experience with a dedicated interventional robotic system for CT-guided biopsies of lung lesions: a comparison with the conventional manual technique. *European Radiology*, 25(5):1310–1316, 2015.

[AAP+15b] Michele Anzidei, Renato Argirò, Andrea Porfiri, Fabrizio Boni, Marco Anile, Fulvio Zaccagna, Domenico Vitolo, Luca Saba, Alessandro Napoli, Andrea Leonardi, others, Flavia Longo, Federico Venuta, Mario Bezzi, and Carlo Catalano. Preliminary clinical experience with a dedicated interventional robotic system for CT-guided biopsies of lung lesions: A comparison with the conventional manual technique. *European Radiology*, 25(5):1310–1316, May 2015.

[ABG08] Ron Alterovitz, Michael Branicky, and Ken Goldberg. Constant-Curvature Motion Planning Under Uncertainty with Applications in Image-Guided Medical Needle Steering. In Srinivas Akella, Nancy M. Amato, Wesley H. Huang, and Bud Mishra, editors, *Algorithmic Foundation of Robotics VII: Selected Contributions of the Seventh International Workshop on the Algorithmic Foundations of Robotics*, Springer Tracts in Advanced Robotics, pages 319–334. Springer, Berlin, Heidelberg, 2008.

[Aer16] Joachim G. Aerts. Transthoracic Needle Biopsies: It's More than Just Hitting the Bull's-eye. *Clinical Cancer Research*, 22(2):273–274, January 2016.

[Age] Ageing and health. https://www.who.int/news-room/fact-sheets/detail/ageing-and-health.

[AGS+13] Nastaran Aghakhani, Milad Geravand, Navid Shahriari, Marilena Vendittelli, and Giuseppe Oriolo. Task control with remote center of motion

constraint for minimally invasive robotic surgery. In *2013 IEEE International Conference on Robotics and Automation*, pages 5807–5812, May 2013. ISSN: 1050-4729.

[AHB87] K. S. Arun, T. S. Huang, and S. D. Blostein. Least-Squares Fitting of Two 3-D Point Sets. *IEEE Transactions on Pattern Analysis and Machine Intelligence*, PAMI-9(5):698–700, September 1987.

[AHF+15] Maarten M. Arnolli, Nevan C. Hanumara, Michel Franken, Dannis M. Brouwer, and Ivo A. M. J. Broeders. An overview of systems for CT- and MRI-guided percutaneous needle placement in the thorax and abdomen. *The International Journal of Medical Robotics and Computer Assisted Surgery*, 11(4):458–475, 2015. _eprint: https://onlinelibrary.wiley.com/doi/pdf/10.1002/rcs.1630.

[AKS+13] S Farokh Atashzar, Iman Khalaji, Mahya Shahbazi, Ali Talasaz, Rajni V Patel, and Michael D Naish. Robot-assisted lung motion compensation during needle insertion. *Proceedings - IEEE International Conference on Robotics and Automation*, pages 1682–1687, 2013.

[Ame19] American Cancer Society. Key Statistics for Lung Cancer, 2019.

[Arr] Array programming with NumPy — Nature. https://www.nature.com/articles/s41586-020-2649-2.

[Asa83] Haruhiko Asada. A Geometrical Representation of Manipulator Dynamics and Its Application to Arm Design. *Journal of Dynamic Systems, Measurement, and Control*, 105(3):131–142, September 1983.

[Aur19] Auris Health, Inc. Monarch Platform - Endoscopy Transformed, 2019.

[AWB+15] Melissa K. Accordino, Jason D. Wright, Donna Buono, Alfred I. Neugut, and Dawn L. Hershman. Trends in use and safety of image-guided transthoracic needle biopsies in patients with cancer. *Journal of Oncology Practice*, 11(3):e351–e359, January 2015.

[BB98] P. Baerlocher and R. Boulic. Task-priority formulations for the kinematic control of highly redundant articulated structures. In *Proceedings. 1998 IEEE/RSJ International Conference on Intelligent Robots and Systems. Innovations in Theory, Practice and Applications (Cat. No.98CH36190)*, volume 1, pages 323–329 vol.1, October 1998.

[BDSR+18a] Eliel Ben-David, Moran Shochat, Ido Roth, Isaac Nissenbaum, Jacob Sosna, and S. Nahum Goldberg. Evaluation of a CT-Guided Robotic System for Precise Percutaneous Needle Insertion. *Journal of Vascular and Interventional Radiology*, 29(10):1440–1446, October 2018. Publisher: Elsevier.

[BDSR+18b] Eliel Ben-David, Moran Shochat, Ido Roth, Isaac Nissenbaum, Jacob Sosna, and S. Nahum Goldberg. Evaluation of a CT-guided robotic system for precise percutaneous needle insertion. *Journal of Vascular and Interventional Radiology*, 29(10):1440–1446, October 2018. Publisher: Elsevier.

[BGBE18] Esia Belbachir, Ehsan Golkar, Bernard Bayle, and Caroline Essert. Automatic planning of needle placement for robot-assisted percutaneous procedures. *International Journal of Computer Assisted Radiology and Surgery*, 13(9):1429–1438, September 2018.

[BGT+21] Felix Boehm, Rene Graesslin, Marie-Nicole Theodoraki, Leon Schild, Jens Greve, Thomas K. Hoffmann, and Patrick J. Schuler. Current Advances in Robotics for Head and Neck Surgery-A Systematic Review. *Cancers*, 13(6):1398, March 2021.

[BLE+18] Marie Beermann, Johan Lindeberg, Jennie Engstrand, Karolina Galmén, Silja Karlgren, David Stillström, Henrik Nilsson, Piotr Harbut, and Jacob Freedman. 1000 consecutive ablation sessions in the era of computer assisted image guidance – Lessons learned. *European Journal of Radiology Open*, 6:1–8, December 2018.

[BSE+19] Reto Bale, Peter Schullian, Gernot Eberle, Daniel Putzer, Heinz Zoller, Stefan Schneeberger, Claudia Manzl, Patrizia Moser, and Georg Oberhuber. Stereotactic Radiofrequency Ablation of Hepatocellular Carcinoma: a Histopathological Study in Explanted Livers. *Hepatology*, 70(3):840–850, 2019. _eprint: https://onlinelibrary.wiley.com/doi/pdf/10.1002/hep.30406.

[BSK18] Maryam Barkhordari, Hamid Sadeghian, and Mehdi Keshmiri. Robot Assisted Needle Insertion Using CT-Scan Images. In *2018 6th RSI International Conference on Robotics and Mechatronics (IcRoM)*, pages 566–571, October 2018. ISSN: 2572-6889.

[BWM+03] Emad M. Boctor, Robert J. Webster, Herve Mathieu, Allison M. Okamura, and Gabor Fichtinger. Virtual remote center of motion control for needle placement robots. *Lecture Notes in Computer Science (including subseries Lecture Notes in Artificial Intelligence and Lecture Notes in Bioinformatics)*, 2878:157–164, November 2003.

[BWM+04] Emad M. Boctor, Robert J. Webster, Herve Mathieu, Allison M. Okamura, and Gabor Fichtinger. Virtual Remote Center of Motion control for needle placement robots. *Computer Aided Surgery*, 9(5):175–183, January 2004. Publisher: Informa UK Limited.

[BZJ+08a] Ivan Bricault, Nabil Zemiti, Emilie Jouniaux, Celine Fouard, Elise Taillant, Frederic Dorandeu, and Philippe Cinquin. Light Puncture Robot for CT and MRI Interventions. *IEEE Engineering in Medicine and Biology Magazine*, 27(3):42–50, May 2008. Conference Name: IEEE Engineering in Medicine and Biology Magazine.

[BZJ+08b] Ivan Bricault, Nabil Zemiti, Emilie Jouniaux, Céline Fouard, Élise Taillant, Frederic Dorandeu, and Philippe Cinquin. Light puncture robot for CT and MRI interventions. In *IEEE Engineering in Medicine and Biology Magazine*, volume 27, pages 42–50. Institute of Electrical and Electronics Engineers Inc., 2008. Issue: 3 ISSN: 07395175.

[Can22] Cancer Data and Statistics — CDC. https://www.cdc.gov/cancer/dcpc/data/index.htm, June 2022.

[CAO+07] Eftychios Christoforou, Erbil Akbudak, Alpay Ozcan, Menelaos Karanikolas, and Nikolaos V. Tsekos. Performance of interventions with manipulator-driven real-time MR guidance: implementation and initial in vitro tests. *Magnetic Resonance Imaging*, 25(1):69–77, January 2007.

[CBCV15] Monzer A. Chehab, Waleed Brinjikji, Alexander Copelan, and Aradhana M. Venkatesan. Navigational Tools for Interventional Radiology and Interventional Oncology Applications. *Seminars in Interventional Radiology*, 32(4):416–427, December 2015.

[CBG22] Ryan D. Chow, Elizabeth H. Bradley, and Cary P. Gross. Comparison of Cancer-Related Spending and Mortality Rates in the US vs 21 High-Income Countries. *JAMA Health Forum*, 3(5):e221229, May 2022.

[CHGS19] Yue Chen, Joseph Howard, Isuru Godage, and Saikat Sengupta. Closed Loop Control of an MR-Conditional Robot with Wireless Tracking Coil Feedback. *Annals of Biomedical Engineering*, 47(11):2322–2333, November 2019.

[CIV] CIVCO - Fusion & Tracking Technology. https://www.civco.com/products/fusion-tracking-technology/.

[CKS+21] Yu-Wen Chiu, Yu-Hsiang Kao, Michael J Simoff, David E Ost, Oliver Wagner, James Lavin, Richard A Culbertson, and Dean G Smith. Costs of Biopsy and Complications in Patients with Lung Cancer. *ClinicoEconomics and Outcomes Research: CEOR*, 13:191–200, March 2021.

[CMG09] Chun-Cheng R. Chen, Michael I. Miga, and Robert L. Galloway. Optimizing Electrode Placement Using Finite-Element Models in Radiofrequency Ablation Treatment Planning. *IEEE Transactions on Biomedical*

Engineering, 56(2):237–245, February 2009. Conference Name: IEEE Transactions on Biomedical Engineering.

[Coo93] I. D. Coope. Circle fitting by linear and nonlinear least squares. *Journal of Optimization Theory and Applications*, 76(2):381–388, February 1993.

[CPG+05] Ben Challacombe, Alexandru Patriciu, Jonathan Glass, Monish Aron, Tom Jarrett, Fernando Kim, Peter Pinto, Dan Stoianovici, Nigel Smeeton, Richard Tiptaft, Louis Kavoussi, and Prokar Dasgupta. A randomized controlled trial of human versus robotic and telerobotic access to the kidney as the first step in percutaneous nephrolithotomy. *Computer Aided Surgery*, 2005.

[CSA+14] Eftychios G. Christoforou, Ioannis Seimenis, Eleni Andreou, Eleni Eracleous, and Nikolaos V. Tsekos. A novel, general-purpose, MR-compatible, manually actuated robotic manipulation system for minimally invasive interventions under direct MRI guidance. *The International Journal of Medical Robotics and Computer Assisted Surgery*, 10(1):22–34, March 2014.

[CTL+15] F. Cornelis, H. Takaki, M. Laskhmanan, J. C. Durack, J. P. Erinjeri, G. I. Getrajdman, M. Maybody, C. T. Sofocleous, S. B. Solomon, and G. Srimathveeravalli. Comparison of CT Fluoroscopy-Guided Manual and CT-Guided Robotic Positioning System for In Vivo Needle Placements in Swine Liver. *CardioVascular and Interventional Radiology*, 38(5):1252–1260, October 2015.

[CWL+05] K. Cleary, V. Watson, D. Lindisch, R. H. Taylor, G. Fichtinger, S. Xu, C. S. White, J. Donlon, M. Taylor, A. Patriciu, D. Mazilu, and D. Stoianovici. Precision placement of instruments for minimally invasive procedures using a "needle driver" robot. *The International Journal of Medical Robotics and Computer Assisted Surgery*, 1(2):40–47, January 2005. Publisher: John Wiley & Sons, Ltd.

[DJY+17] Huaisu Dou, Shan Jiang, Zhiyong Yang, Luqing Sun, Xiaodong Ma, and Bin Huo. Design and validation of a CT-guided robotic system for lung cancer brachytherapy:. *Medical Physics*, 44(9):4828–4837, September 2017.

[DLJ+98] Stoianovici D, Whitcomb L, Anderson J, Taylor R, and Delp S. A modular surgical robotic system for image guided percutaneous procedures. *Medical Image Computing and Computer-Assisted Intervention -MICCAI'98*, 1496:404–410, 1998. Publisher: Springer.

[DMGS+17] Pierre Durand, Alexandre Moreau-Gaudry, Anne-Sophie Silvent, Julien Frandon, Emilie Chipon, Maud Médici, and Ivan Bricault. Computer assisted electromagnetic navigation improves accuracy in computed tomography guided interventions: A prospective randomized clinical trial. *PLOS ONE*, 12(3):e0173751, March 2017. Publisher: Public Library of Science.

[DNMK08] Christophe Doignon, Florent Nageotte, Benjamin Maurin, and Alexandre Krupa. Pose Estimation and Feature Tracking for Robot Assisted Surgery with Medical Imaging. In Danica Kragic and Ville Kyrki, editors, *Unifying Perspectives in Computational and Robot Vision*, Lecture Notes in Electrical Engineering, pages 79–101. Springer US, Boston, MA, 2008.

[DTSD+19] Luca Di Tommaso, Marco Spadaccini, Matteo Donadon, Nicola Personeni, Abubaker Elamin, Alessio Aghemo, and Ana Lleo. Role of liver biopsy in hepatocellular carcinoma. *World Journal of Gastroenterology*, 25(40):6041–6052, October 2019.

[DXA+10] Vincent Duindam, Jijie Xu, Ron Alterovitz, Shankar Sastry, and Ken Goldberg. 3D Motion Planning Algorithms for Steerable Needles Using Inverse Kinematics. In Gregory S. Chirikjian, Howie Choset, Marco Morales, and Todd Murphey, editors, *Algorithmic Foundation of Robotics VIII: Selected Contributions of the Eight International Workshop on the Algorithmic Foundations of Robotics*, Springer Tracts in Advanced Robotics, pages 535–549. Springer, Berlin, Heidelberg, 2010.

[EFP+16] Lars C. Ebert, Martin Fürst, Wolfgang Ptacek, Thomas D. Ruder, Dominic Gascho, Wolf Schweitzer, Michael J. Thali, and Patricia M. Flach. Automatic entry point planning for robotic post-mortem CT-based needle placement. *Forensic Science, Medicine, and Pathology*, 12(3):336–342, September 2016.

[EPB+14] Lars Christian Ebert, Wolfgang Ptacek, Robert Breitbeck, Martin Fürst, Gernot Kronreif, Rosa Maria Martinez, Michael Thali, and Patricia M. Flach. Virtobot 2.0: the future of automated surface documentation and CT-guided needle placement in forensic medicine. *Forensic Science, Medicine, and Pathology*, 10(2):179–186, June 2014.

[EPN+10] Lars Christian Ebert, Wolfgang Ptacek, Silvio Naether, Martin Fürst, Steffen Ross, Ursula Buck, Stefan Weber, and Michael Thali. Virtobot–a multi-functional robotic system for 3D surface scanning and automatic post mortem biopsy. *The International Journal of Medical Robotics and Computer Assisted Surgery*, 6(1):18–27, 2010. _eprint: https://onlinelibrary.wiley.com/doi/pdf/10.1002/rcs.285.

[FB81] Martin A. Fischler and Robert C. Bolles. Random sample consensus: A paradigm for model fitting with applications to image analysis and automated cartography. *Communications of the ACM*, 24(6):381–395, June 1981.

[FBKC+12] Andriy Fedorov, Reinhard Beichel, Jayashree Kalpathy-Cramer, Julien Finet, Jean-Christophe Fillion-Robin, Sonia Pujol, Christian Bauer, Dominique Jennings, Fiona Fennessy, Milan Sonka, and others. 3D Slicer as an image computing platform for the Quantitative Imaging Network. *Magnetic resonance imaging*, 30(9):1323–1341, 2012. Publisher: Elsevier.

[FBS+17] David Fielding, Farzad Bashirzadeh, Jung Hua Son, Maryann Todman, Hau Tan, Adrian Chin, Karin Steinke, and Morgan Windsor. First human use of a new robotic-assisted navigation system for small peripheral pulmonary nodules demonstrates good safety profile and high diagnostic yield. *Chest*, 152(4):A858, October 2017.

[FDP+02] Gabor Fichtinger, Theodore L. DeWeese, Alexandru Patriciu, Attila Tanacs, Dumitru Mazilu, James H. Anderson, Ken Masamune, Russell H. Taylor, and Dan Stoianovici. System for Robotically Assisted Prostate Biopsy and Therapy with Intraoperative CT Guidance. *Academic Radiology*, 9(1):60–74, January 2002.

[FIS+21] Samuel Frishman, Robert D. Ings, Vipul Sheth, Bruce L. Daniel, and Mark R. Cutkosky. Extending Reach Inside the MRI Bore: A 7-DOF, Low-Friction, Hydrostatic Teleoperator. *IEEE Transactions on Medical Robotics and Bionics*, 3(3):701–713, August 2021.

[Fit09] J. Michael Fitzpatrick. Fiducial registration error and target registration error are uncorrelated. In *Medical Imaging 2009: Visualization, Image-Guided Procedures, and Modeling*, volume 7261, pages 21–32. SPIE, March 2009.

[Fit10] J. Michael Fitzpatrick. The Role of Registration in Accurate Surgical Guidance. *Proceedings of the Institution of Mechanical Engineers. Part H, Journal of engineering in medicine*, 224(5):607–622, 2010.

[FJM+21] Christian Fiedler, Paul-Philipp Jacobs, Marcel Müller, Silke Kolbig, Ronny Grunert, Jürgen Meixensberger, and Dirk Winkler. A Comparative Study of Automatic Localization Algorithms for Spherical Markers within 3D MRI Data. *Brain Sciences*, 11(7):876, July 2021.

[FKP+20] Samuel Frishman, Ali Kight, Ileana Pirozzi, Mela C. Coffey, Bruce L. Daniel, and Mark R. Cutkosky. Enabling In-Bore MRI-Guided Biopsies

with Force Feedback. *IEEE Transactions on Haptics*, 13(1):159–166, January 2020.

[FRD+12] Giovanni Fattori, Marco Riboldi, Maxime Desplanques, Barbara Tagaste, Andrea Pella, Roberto Orecchia, and Guido Baroni. Automated Fiducial Localization in CT Images Based on Surface Processing and Geometrical Prior Knowledge for Radiotherapy Applications. *IEEE Transactions on Biomedical Engineering*, 59(8):2191–2199, August 2012.

[FS67] William R. Ferrell and Thomas B. Sheridan. Supervisory control of remote manipulation. *IEEE Spectrum*, 4(10):81–88, October 1967. Conference Name: IEEE Spectrum.

[FTH22] Gabor Fichtinger, Jocelyne Troccaz, and Tamas Haidegger. Image-Guided Interventional Robotics: Lost in Translation? *Proceedings of the IEEE*, 110(7):932–950, July 2022. Conference Name: Proceedings of the IEEE.

[FWM98] J.M. Fitzpatrick, J.B. West, and C.R. Maurer. Predicting error in rigid-body point-based registration. *IEEE Transactions on Medical Imaging*, 17(5):694–702, October 1998.

[GAO+14] Christopher Gilbert, Jason Akulian, Ricardo Ortiz, Hans Lee, and Lonny Yarmus. Novel bronchoscopic strategies for the diagnosis of peripheral lung lesions: Present techniques and future directions. *Respirology*, 19(5):636–644, 2014.

[GBL+18] Evalyn I. George, Timothy C. Brand, Anthony LaPorta, Jacques Marescaux, and Richard M. Satava. Origins of Robotic Surgery: From Skepticism to Standard of Care. *JSLS : Journal of the Society of Laparoendoscopic Surgeons*, 22(4):e2018.00039, 2018.

[GDBNR21] Boris Guiu, Thierry De Baère, Guillaume Noel, and Maxime Ronot. Feasibility, safety and accuracy of a CT-guided robotic assistance for percutaneous needle placement in a swine liver model. *Scientific Reports*, 11(1):5218, December 2021.

[GHT+22] Bogdan Gherman, Nadim Al Hajjar, Paul Tucan, Corina Radu, Calin Vaida, Emil Mois, Alin Burz, and Doina Pisla. Risk Assessment-Oriented Design of a Needle Insertion Robotic System for Non-Resectable Liver Tumors. *Healthcare*, 10(2):389, February 2022. Number: 2 Publisher: Multidisciplinary Digital Publishing Institute.

[Gim19] Gimp. *GNU Image Manipulation Program*, 2019. `https://www.gimp.org/`, Accessed: 2019-02-04.

[GMGH+18a] Julien Ghelfi, Alexandre Moreau-Gaudry, Nikolai Hungr, Céline Fouard, Baptiste Véron, Maud Medici, Emilie Chipon, Philippe Cinquin, and Ivan Bricault. Evaluation of the Needle Positioning Accuracy of a Light Puncture Robot Under MRI Guidance: Results of a Clinical Trial on Healthy Volunteers. *CardioVascular and Interventional Radiology*, 41(9):1428–1435, September 2018.

[GMGH+18b] Julien Ghelfi, Alexandre Moreau-Gaudry, Nikolai Hungr, Céline Fouard, Baptiste Véron, Maud Medici, Emilie Chipon, Philippe Cinquin, and Ivan Bricault. Evaluation of the Needle Positioning Accuracy of a Light Puncture Robot Under MRI Guidance: Results of a Clinical Trial on Healthy Volunteers. *CardioVascular and Interventional Radiology*, 41(9):1428–1435, September 2018. Publisher: Springer New York LLC.

[GSS20] Vincent Groenhuis, Françoise J. Siepel, and Stefano Stramigioli. 22 - Sunram 5: A Magnetic Resonance-Safe Robotic System for Breast Biopsy, Driven by Pneumatic Stepper Motors. In Mohammad H. Abedin-Nasab, editor, *Handbook of Robotic and Image-Guided Surgery*, pages 375–396. Elsevier, January 2020.

[GSY+14] Animesh Garg, Timmy Siauw, Guang Yang, Sachin Patil, J. Adam M. Cunha, I-Chow Hsu, Jean Pouliot, Alper Atamtürk, and Ken Goldberg. Exact reachability analysis for planning skew-line needle arrangements for automated brachytherapy. In *2014 IEEE International Conference on Automation Science and Engineering (CASE)*, pages 524–531, August 2014. ISSN: 2161-8089.

[HBCF16a] Nikolai Hungr, Ivan Bricault, Philippe Cinquin, and Céline Fouard. Design and Validation of a CT- and MRI-Guided Robot for Percutaneous Needle Procedures. *IEEE Transactions on Robotics*, 32(4):973–987, August 2016. Conference Name: IEEE Transactions on Robotics.

[HBCF16b] Nikolai Hungr, Ivan Bricault, Philippe Cinquin, and Celine Fouard. Design and Validation of a CT-and MRI-Guided Robot for Percutaneous Needle Procedures. *IEEE Transactions on Robotics*, 32(4):973–987, 2016.

[HBCF16c] Nikolai Hungr, Ivan Bricault, Philippe Cinquin, and Celine Fouard. Design and Validation of a CT-and MRI-Guided Robot for Percutaneous Needle Procedures. *IEEE Transactions on Robotics*, 32(4):973–987, 2016. Publisher: IEEE.

[HC21] Jesse Haviland and Peter Corke. NEO: A Novel Expeditious Optimisation Algorithm for Reactive Motion Control of Manipulators. *IEEE*

Robotics and Automation Letters, 6(2):1043–1050, April 2021. Conference Name: IEEE Robotics and Automation Letters.

[HCE17] Noura Hamze, Pierre Collet, and Caroline Essert. Evolutionary approaches for surgical path planning: A quantitative study on Deep Brain Stimulation. In *2017 IEEE Congress on Evolutionary Computation (CEC)*, pages 1087–1094, June 2017.

[HDBd+17] W. J. Heerink, G. H. De Bock, G. J. de Jonge, H. J.M. M Groen, & R Vliegenthart, & M Oudkerk, R. Vliegenthart, and M. Oudkerk. Complication rates of CT-guided transthoracic lung biopsy: Meta-analysis. *European radiology*, 27(1):138–148, January 2017.

[HFG+03] Eckhard Hempel, Harald Fischer, Lothar Gumb, Thomas Höhn, Holger Krause, Udo Voges, Helmut Breitwieser, Bernd Gutmann, Jürgen Durke, Michael Bock, and Andreas Melzer. An MRI-Compatible Surgical Robot for Precise Radiological Interventions. *Computer Aided Surgery*, 8(4):180–191, January 2003. Publisher: Taylor & Francis _eprint: https://doi.org/10.3109/10929080309146052.

[HKK+18] Yeji Han, Hyun Jung Kim, Kyoung Ae Kong, Soo Jung Kim, Su Hwan Lee, Yon Ju Ryu, Jin Hwa Lee, Yookyoung Kim, Sung Shine Shim, and Jung Hyun Chang. Diagnosis of small pulmonary lesions by transbronchial lung biopsy with radial endobronchial ultrasound and virtual bronchoscopic navigation versus CT-guided transthoracic needle biopsy: A systematic review and meta-analysis. *PloS one*, 13(1):e0191590, 2018.

[HKM+17] Takao Hiraki, Tetsushi Kamegawa, Takayuki Matsuno, Jun Sakurai, Yasuzo Kirita, Ryutaro Matsuura, Takuya Yamaguchi, Takanori Sasaki, Toshiharu Mitsuhashi, Toshiyuki Komaki, Yoshihisa Masaoka, Yusuke Matsui, Hiroyasu Fujiwara, Toshihiro Iguchi, Hideo Gobara, and Susumu Kanazawa. Robotically driven CT-guided needle insertion: Preliminary results in phantom and animal experiments. *Radiology*, 285(2):454–461, November 2017. Publisher: Radiological Society of North America Inc.

[HMK+18] Takao Hiraki, Takayuki Matsuno, Tetsushi Kamegawa, Toshiyuki Komaki, Jun Sakurai, Ryutaro Matsuura, Takuya Yamaguchi, Takanori Sasaki, Toshihiro Iguchi, Yusuke Matsui, Hideo Gobara, and Susumu Kanazawa. Robotic Insertion of Various Ablation Needles Under Computed Tomography Guidance: Accuracy in Animal Experiments. *European Journal of Radiology*, 105:162–167, August 2018.

[HS87] John M Hollerbach and Ki Suh. Redundancy resolution of manipulators through torque optimization. *IEEE Journal on Robotics and Automation*, 3(4):308–316, 1987.

[HTV+21] Meng Huang, Tyler A. Tetreault, Avani Vaishnav, Philip J. York, and Blake N. Staub. The current state of navigation in robotic spine surgery. *Annals of Translational Medicine*, 9(1):86–86, January 2021. Number: 1 Publisher: AME Publishing Company.

[IGG+19] Francesco Izzo, Vincenza Granata, Roberto Grassi, Roberta Fusco, Raffaele Palaia, Paolo Delrio, Gianpaolo Carrafiello, Daniel Azoulay, Antonella Petrillo, and Steven A Curley. Radiofrequency Ablation and Microwave Ablation in Liver Tumors: An Update. *The Oncologist*, 24(10):e990–e1005, October 2019.

[Ins] Instrument flight to the inner ear — Science Robotics. https://www.science.org/doi/10.1126/scirobotics.aal4916.

[Int] Intuitive and efficient solution for Percutaneous Interventions. https://www.imactis.com/en/.

[Int19] Intuitive Surgical, Inc. Ion, 2019. `https://www.intuitive.com/en/products-and-services/ion`, Accessed: 2019-02-06.

[ISO00] ISO 9283:1998 - Manipulating industrial robots - Performance criteria and related test methods, 2000.

[JDC+18] A. Kyle Jones, Robert G. Dixon, Jeremy D. Collins, Eric M. Walser, and Boris Nikolic. Best Practice Guidelines for CT-Guided Interventional Procedures. *Journal of Vascular and Interventional Radiology*, 29(4):518–519, April 2018. Publisher: Elsevier.

[JFD19] Stephen James, Marc Freese, and Andrew J. Davison. PyRep: Bringing V-REP to Deep Robot Learning, June 2019. arXiv:1906.11176 [cs].

[JSF+06] L Joskowicz, R Shamir, M Freiman, M Shoham, E Zehavi, F Umansky, and Y Shoshan. Image-guided system with miniature robot for precise positioning and targeting in keyhole neurosurgery. *Computer Aided Surgery*, 11(4):181–193, January 2006.

[JWNKGBKJBSHK17] Hyung Jin Won Namkug Kim Guk Bae Kim Joon Beom Seo Hongho Kim. Validation of a CT-guided intervention robot for biopsy and radiofrequency ablation: experimental study with an abdominal phantom From the Departments of Radiology (I N T E R V E N T I O N A L R A D I O LO G Y. 2017.

[JYY+17] Shan Jiang, Wei Yuan, Yunpeng Yang, Daguang Zhang, Ningbo Liu, and Wei Wang. Modelling and analysis of a novel CT-guided puncture robot for lung brachytherapy. *Advanced Robotics*, 31(11):557–569, June 2017.

[KB87] Charles A. Klein and Bruce E. Blaho. Dexterity Measures for the Design and Control of Kinematically Redundant Manipulators. *The International Journal of Robotics Research*, 6(2):72–83, June 1987. Publisher: SAGE Publications Ltd STM.

[KBFD21] Omaditya Khanna, Ryan Beasley, Daniel Franco, and Simon DiMaio. The Path to Surgical Robotics in Neurosurgery. *Operative Neurosurgery (Hagerstown, Md.)*, 20(6):514–520, May 2021.

[KFP+] Gernot Kronreif, Martin Fürst, Wolfgang Ptacek, Martin Kornfeld, and Joachim Kettenbach. Robotic System for Image Guided Therapie-B-RobII.

[KHK+20] Toshiyuki Komaki, Takao Hiraki, Tetsushi Kamegawa, Takayuki Matsuno, Jun Sakurai, Ryutaro Matsuura, Takuya Yamaguchi, Takanori Sasaki, Toshiharu Mitsuhashi, Soichiro Okamoto, Mayu Uka, Yusuke Matsui, Toshihiro Iguchi, Hideo Gobara, and Susumu Kanazawa. Robotic CT-guided out-of-plane needle insertion: comparison of angle accuracy with manual insertion in phantom and measurement of distance accuracy in animals. *European Radiology*, 30(3):1342–1349, March 2020.

[KK15] Joachim Kettenbach and Gernot Kronreif. Robotic systems for percutaneous needle-guided interventions. *Minimally Invasive Therapy and Allied Technologies*, 24(1):45–53, 2015.

[KKF+04] Joachim Kettenbach, Gernot Kronreif, Michael Figl, Martin Furst, Wolfgang Birkfellner, Rudolf Hanel, and Helmar Bergmann. Robot-assisted biopsy using ultrasound guidance: Initial results from in vitro tests. *European Radiology 2004 15:4*, 15(4):765–771, September 2004.

[KKT+14] Joachim Kettenbach, Levent Kara, Grzegorz Toporek, Martin Fuerst, and Gernot Kronreif. A robotic needle-positioning and guidance system for CT-guided puncture: Ex vivo results. *Minimally Invasive Therapy and Allied Technologies*, 23(5):271–278, October 2014.

[KRP+16] Thomas Kluyver, Benjamin Ragan-Kelley, Fernando Pérez, Brian Granger, Matthias Bussonnier, Jonathan Frederic, Kyle Kelley, Jessica Hamrick, Jason Grout, Sylvain Corlay, Paul Ivanov, Damián Avila, Safia Abdalla, Carol Willing, and Jupyter development team. Jupyter Notebooks – a publishing format for reproducible computational workflows.

In Fernando Loizides and Birgit Scmidt, editors, *20th International Conference on Electronic Publishing (01/01/16)*, pages 87–90. IOS Press, 2016.

[KRS+11] Louis B. Kratchman, Mohammed M. Rahman, Justin R. Saunders, Philip J. Swaney, and Robert J. Webster III. Toward robotic needle steering in lung biopsy: A tendon-actuated approach. In Kenneth H. Wong and David R. Holmes III, editors, *Medical Imaging 2011: Visualization, Image-Guided Procedures, and Modeling*, volume 7964, page 79641I. SPIE, March 2011.

[KSKK17] Yeoun Jae Kim, Jong Hyun Seo, Hong Rae Kim, and Kwang Gi Kim. Impedance and admittance control for respiratory-motion compensation during robotic needle insertion - a preliminary test. *The International Journal of Medical Robotics and Computer Assisted Surgery*, 13(4):e1795, December 2017.

[KSM+16] Alan Kuntz, Philip J Swaney, A Mahoney, Richard H Feins, Yueh Z Lee, R J Webster III, and Ron Alterovitz. Toward Transoral Peripheral Lung Access: Steering Bronchoscope-deployed Needles through Porcine Lung Tissue. In *Hamlyn Symposium on Medical Robotics*, pages 9–10, 2016.

[LC87a] William E. Lorensen and Harvey E. Cline. Marching cubes: A high resolution 3D surface construction algorithm. In *Proceedings of the 14th annual conference on Computer graphics and interactive techniques*, SIGGRAPH '87, pages 163–169, New York, NY, USA, August 1987. Association for Computing Machinery.

[LC87b] William E. Lorensen and Harvey E. Cline. Marching cubes: A high resolution 3D surface construction algorithm. In *Proceedings of the 14th Annual Conference on Computer Graphics and Interactive Techniques*, SIGGRAPH '87, pages 163–169, New York, NY, USA, August 1987. Association for Computing Machinery.

[LCIB13] Bradley Lowekamp, David Chen, Luis Ibanez, and Daniel Blezek. The Design of SimpleITK. *Frontiers in Neuroinformatics*, 7, 2013.

[LCP+14] Michel Lefranc, Cyril Capel, Anne Sophie Pruvot, Anthony Fichten, Christine Desenclos, Patrick Toussaint, Daniel Le Gars, and Johan Peltier. The Impact of the Reference Imaging Modality, Registration Method and Intraoperative Flat-Panel Computed Tomography on the Accuracy of the ROSA® Stereotactic Robot. *Stereotactic and Functional Neurosurgery*, 92(4):242–250, 2014.

[Len18] Shuai Leng. Radiation Dose in CT–guided Interventional Procedures: Establishing a Benchmark. *Radiology*, 289(1):158–159, October 2018. Publisher: Radiological Society of North America.

[LGR+21] Shiran Levy, S. Nahum Goldberg, Ido Roth, Moran Shochat, Jacob Sosna, Isaac Leichter, and Sebastian Flacke. Clinical evaluation of a robotic system for precise CT-guided percutaneous procedures. *Abdominal Radiology*, 46(10):5007–5016, October 2021.

[LKKC12] Jongwon Lee, Sungmin Kim, Young Soo Kim, and Wan Kyun Chung. Optimal surgical planning guidance for lumbar spinal fusion considering operational safety and vertebra-screw interface strength. *International Journal of Medical Robotics and Computer Assisted Surgery*, 8(3):261–272, September 2012.

[LMWS11] Peng Lei, Fred Moeslein, Bradford J. Wood, and Raj Shekhar. Real-time tracking of liver motion and deformation using a flexible needle. *International Journal of Computer Assisted Radiology and Surgery*, 6(3):435–446, May 2011.

[LN00] Michael H. Loser and Nassir Navab. A New Robotic System for Visually Controlled Percutaneous Interventions under CT Fluoroscopy. In Gerhard Goos, Juris Hartmanis, Jan van Leeuwen, Scott L. Delp, Anthony M. DiGoia, and Branislav Jaramaz, editors, *Medical Image Computing and Computer-Assisted Intervention – MICCAI 2000*, volume 1935, pages 887–896. Springer Berlin Heidelberg, Berlin, Heidelberg, 2000. Series Title: Lecture Notes in Computer Science.

[LQD+19] Ping Liu, Jing Qin, Bin Duan, Qiong Wang, Xiaoyu Tan, Baoliang Zhao, Peneyra Libao Jonnathan, Chee Kong Chui, and Pheng Ann Heng. Overlapping radiofrequency ablation planning and robot-assisted needle insertion for large liver tumors. *International Journal of Medical Robotics and Computer Assisted Surgery*, 15(1), February 2019.

[LSL+19] Sunghwan Lim, Karun Sharma, Pan Li, Doru Petrisor, Stanley Fricke, Dan Stoianovici, and Kevin Cleary. Robotically assisted long bone biopsy under MRI: Cadaver study results. *International Journal of Computer Assisted Radiology and Surgery*, 14(1):147–156, January 2019.

[LSS+13] Gang Li, Hao Su, Weijian Shang, Junichi Tokuda, Nobuhiko Hata, Clare Tempany, and Gregory Fischer. A Fully Actuated Robotic Assistant for MRI-Guided Prostate Biopsy and Brachytherapy. *Proceedings - Society of Photo-Optical Instrumentation Engineers*, 8671:17–, 2013.

[LTK+06] Isador H. Lieberman, Daisuke Togawa, Mark M. Kayanja, Mary K. Reinhardt, Alon Friedlander, Nachshon Knoller, and Edward C. Benzel. Bone-mounted Miniature Robotic Guidance for Pedicle Screw and Translaminar Facet Screw Placement: Part I–Technical Development and a Test Case Result. *Neurosurgery*, 59(3):641–650, September 2006.

[LWDW19] Liang Li, Julia Wu, Hui Ding, and Guangzhi Wang. A "eye-in-body" integrated surgery robot system for stereotactic surgery. *International Journal of Computer Assisted Radiology and Surgery*, 14(12):2123–2135, December 2019.

[LXL+16] Shaoli Liu, Zeyang Xia, Jianhua Liu, Jing Xu, He Ren, Tong Lu, and Xiangdong Yang. Automatic Multiple-Needle Surgical Planning of Robotic-Assisted Microwave Coagulation in Large Liver Tumor Therapy. *PLOS ONE*, 11(3):e0149482, March 2016. Publisher: Public Library of Science.

[LYC+15] Qinyong Lin, Rongqian Yang, Ken Cai, Peifeng Guan, Weihu Xiao, and Xiaoming Wu. Strategy for accurate liver intervention by an optical tracking system. *Biomedical Optics Express*, 6(9):3287–3302, August 2015.

[MAM15] Pedro Moreira, Momen Abayazid, and Sarthak Misra. Towards physiological motion compensation for flexible needle interventions. In *IEEE International Conference on Intelligent Robots and Systems*, volume 2015-Decem, pages 831–836. Institute of Electrical and Electronics Engineers Inc., December 2015.

[MBG+06] B. Maurin, B. Bayle, J. Gangloff, P. Zanne, M. De Mathelin, and Olivier Piccin. A robotized positioning platform guided by computed tomography: Practical issues and evaluation. In *Proceedings - IEEE International Conference on Robotics and Automation*, volume 2006, pages 251–256, 2006.

[MBP+08] Benjamin Maurin, Bernard Bayle, Olivier Piccin, Jacques Gangloff, Michel de Mathelin, Christophe Doignon, Philippe Zanne, and Afshin Gangi. A Patient-Mounted Robotic Platform for CT-Scan Guided Procedures. *IEEE Transactions on Biomedical Engineering*, 55(10):2417–2425, October 2008. Conference Name: IEEE Transactions on Biomedical Engineering.

[MCS18] Reza Monfaredi, Kevin Cleary, and Karun Sharma. Mri robots for needle-based interventions: Systems and technology. *Annals of Biomedical Engineering*, 46(10):1479–1497, Oct 2018.

[MDG+05] Benjamin Maurin, Christophe Doignon, Jacques Gangloff, Bernard Bayle, Michel de Mathelin, Olivier Piccin, and Afshin Gangi. CTBot: A stereotactic-guided robotic assistant for percutaneous procedures of the abdomen. In *Medical Imaging 2005: Visualization, Image-Guided Procedures, and Display*, volume 5744, pages 241–250. SPIE, April 2005.

[MFP+01a] Ken Masamune, Gabor Fichtinger, Alexandru Patriciu, Robert C. Susil, Russell H. Taylor, Louis R. Kavoussi, James H. Anderson, Ichiro Sakuma, Takeyoshi Dohi, and Dan Stoianovici. System for Robotically Assisted Percutaneous Procedures with Computed Tomography Guidance. *Computer Aided Surgery*, 6(6):370–383, January 2001. Publisher: Taylor & Francis _eprint: https://doi.org/10.3109/10929080109146306.

[MFP+01b] Ken Masamune, Gabor Fichtinger, Alexandru Patriciu, Robert C. Susil, Russell H. Taylor, Louis R. Kavoussi, James H. Anderson, Ichiro Sakuma, Takeyoshi Dohi, and Dan Stoianovici. System for Robotically Assisted Percutaneous Procedures with Computed Tomography Guidance. *https://mc.manuscriptcentral.com/tcas*, 6(6):370–383, January 2001. Publisher: Taylor & Francis.

[MGR+08a] Andreas Melzer, Bernd Gutmann, Thomas Remmele, Renate Wolf, Andreas Lukoscheck, Michael Bock, Hubert Bardenheuer, and Harald Fischer. INNOMOTION for Percutaneous Image-Guided Interventions. *IEEE Engineering in Medicine and Biology Magazine*, 27(3):66–73, May 2008. Conference Name: IEEE Engineering in Medicine and Biology Magazine.

[MGR+08b] Andreas Melzer, Bernd Gutmann, Thomas Remmele, Renate Wolf, Andreas Lukoscheck, Michael Bock, Hubert Bardenheuer, and Harald Fischer. INNOMOTION for Percutaneous Image-Guided Interventions. *IEEE Engineering in Medicine and Biology Magazine*, 27(3):66–73, May 2008.

[Miy17] Muneaki Miyasaka. *Cable Driven Robots: Hysteretic Cable Stretch, Cable-Pulley Network Friction, Fatigue Life, and Kinematics of Two-Arm Multi Staged Flexible Manipulator*. PhD thesis, University of Washington, 2017.

[MJY+19] Xiaodong Ma, Shan Jiang, Zhiyong Yang, Guobin Zhang, Zhonghua Yu, and Shude Chai. A Real-Time Tracking and Visualization System for Robot-Assisted Template Location Method Applied to Lung Cancer Brachytherapy. *Journal of Medical Devices*, 13(1), January 2019.

[MNS12] Jessica S Wang Memoli, Paul J Nietert, and Gerard A Silvestri. Meta-analysis of guided bronchoscopy for the evaluation of the pulmonary nodule. *Chest*, 142(2):385–393, 2012.

[MPF+10] Nader N Massarweh, James O Park, Farhood Farjah, Raymond SW Yeung, Rebecca Gaston Symons, Thomas L Vaughan, Laura-Mae Baldwin, and David R Flum. Trends in the Utilization and Impact of Radiofrequency Ablation for Hepatocellular Carcinoma. *Journal of the American College of Surgeons*, 210(4):441–448, April 2010.

[MPP+06] Michael Muntener, Alexandru Patriciu, Doru Petrisor, Dumitru Mazilu, Herman Bagga, Louis Kavoussi, Kevin Cleary, and Dan Stoianovici. Magnetic resonance imaging compatible robotic system for fully automated brachytherapy seed placement. *Urology*, 68(6):1313–1317, December 2006.

[MPS+14] Rosa M. Martinez, Wolfgang Ptacek, Wolf Schweitzer, Gernot Kronreif, Martin Fürst, Michael J. Thali, and Lars C. Ebert. CT-Guided, Minimally Invasive, Postmortem Needle Biopsy Using the B-Rob II Needle-Positioning Robot. *Journal of Forensic Sciences*, 59(2):517–521, March 2014. Publisher: John Wiley & Sons, Ltd.

[MSC15] Youngjin Moon, Joon Beom Seo, and Jaesoon Choi. Development of new end-effector for proof-of-concept of fully robotic multichannel biopsy. *IEEE/ASME Transactions on Mechatronics*, 20(6):2996–3008, December 2015.

[MvK+17] Pedro Moreira, Gert van de Steeg, Thijs Krabben, Jonathan Zandman, Edsko E. G. Hekman, Ferdinand van der Heijden, Ronald Borra, and Sarthak Misra. The MIRIAM Robot: A Novel Robotic System for MR-Guided Needle Insertion in the Prostate. *Journal of Medical Robotics Research*, 02(04):1750006, December 2017.

[MWX08] W. Mao, R. D. Wiersma, and L. Xing. Fast internal marker tracking algorithm for onboard MV and kV imaging systems. *Medical Physics*, 35(5):1942–1949, May 2008.

[N21] Patel N. Body-Mounted Robotic System for MRI-Guided Shoulder Arthrography: Cadaver and Clinical Workflow Studies. *Front. Robot. AI*, 8, April 2021.

[NKS+20] Sherdil Niyaz, Alan Kuntz, Oren Salzman, Ron Alterovitz, and Siddhartha Srinivasa. Following Surgical Trajectories with Concentric Tube Robots via Nearest-Neighbor Graphs. In Jing Xiao, Torsten Kröger, and

Oussama Khatib, editors, *Proceedings of the 2018 International Symposium on Experimental Robotics*, Springer Proceedings in Advanced Robotics, pages 3–13, Cham, 2020. Springer International Publishing.

[noaa] Class 2 Device Recall Mazor X System (Mazor X Stealth Edition).

[noab] Elekta | Radiotherapy Treatment | Cancer & Brain Disorders.

[noac] The Global Burden of Low Back Pain.

[noad] Intuitive and efficient solution for Percutaneous Interventions.

[noae] Lifetime Risk of Developing or Dying From Cancer.

[noaf] Micromate™ – Interventional Systems.

[noag] Performance of a Robotic Assistance Device in Computed Tomography-Guided Percutaneous Diagnostic and Therapeutic Procedures | SpringerLink.

[noah] Quality Ablation - Standardized and Reproducible Tumour Treatments.

[noai] A simplicial homology algorithm for Lipschitz optimisation | SpringerLink.

[noa15] Cancer Statistics - NCI, April 2015. Archive Location: nciglobal,ncienterprise.

[OBB20] Ahmed A. A. Osman, Timo Bolkart, and Michael J. Black. STAR: Sparse Trained Articulated Human Body Regressor, 2020. arXiv:2008.08535 [cs].

[ORK+19] Sarah O. S. Osman, Emily Russell, Raymond B. King, Karen Crowther, Suneil Jain, Cormac McGrath, Alan R. Hounsell, Kevin M. Prise, and Conor K. McGarry. Fiducial markers visibility and artefacts in prostate cancer radiotherapy multi-modality imaging. *Radiation Oncology*, 14(1):237, December 2019.

[OT08] Alpay Özcan and Nikolaos Tsekos. The Interconnection of MRI Scanner and MR-Compatible Robotic Device: Synergistic Graphical User Interface to Form a Mechatronic System. *IEEE/ASME Transactions on Mechatronics*, 13(3):362–369, June 2008. Conference Name: IEEE/ASME Transactions on Mechatronics.

[ÖVP+20] Yusuf Özbek, Michael Vogele, Christian Plattner, Pedro Costa, Mario Griesser, and Matthias Wieczorek. Fluoroscopy-guided robotic biopsy intervention system. *Current Directions in Biomedical Engineering*, 6(1), May 2020.

[PA10] Sachin Patil and Ron Alterovitz. Interactive Motion Planning for Steerable Needles in 3D Environments with Obstacles. *Proceedings of the ... IEEE/RAS-EMBS International Conference on Biomedical Robotics and Biomechatronics. IEEE/RAS-EMBS International Conference on Biomedical Robotics and Biomechatronics*, pages 893–899, 2010.

[PAVE20] Danial Pour Arab, Sandrine Voros, and Caroline Essert. Dynamic path planning for percutaneous procedures in the abdomen during free breathing. *International Journal of Computer Assisted Radiology and Surgery*, 15(7):1195–1203, July 2020.

[PBB+09] O. Piccin, L. Barbé, B. Bayle, M. de Mathelin, and A. Gangi. A Force Feedback Teleoperated Needle Insertion Device for Percutaneous Procedures. *The International Journal of Robotics Research*, 28(9):1154–1168, September 2009. Publisher: SAGE Publications Ltd STM.

[PBN+21] Mirza Pojskic, Miriam Bopp, Christopher Nimsky, Barbara Carl, and Benjamin Sass. Initial Intraoperative Experience with Robotic-Assisted Pedicle Screw Placement with Cirq® Robotic Alignment: An Evaluation of the First 70 Screws. *Journal of Clinical Medicine*, 10(24):5725, January 2021. Number: 24 Publisher: Multidisciplinary Digital Publishing Institute.

[PKK16] Shin-Hyung Park, Jae-Chul Kim, and Sung Joon Kim. Alternative fiducial markers for Vero real-time tumor tracking radiotherapy: A phantom study. *Journal of the Korean Physical Society*, 69(11):1700–1704, December 2016.

[PMP+03] Alexandru Patriciu, Dumitru Mazilu, Doru Petrisor, Louis Kavoussi, and Dan Stoianovici. Automatic Targeting Method and Accuracy Study in Robot Assisted Needle Procedures. In Gerhard Goos, Juris Hartmanis, Jan van Leeuwen, Randy E. Ellis, and Terry M. Peters, editors, *Medical Image Computing and Computer-Assisted Intervention - MICCAI 2003*, volume 2878, pages 124–131. Springer Berlin Heidelberg, Berlin, Heidelberg, 2003.

[PSV+16] Lauren H. Poniatowski, Sneha S. Somani, Domenico Veneziano, Sean McAdams, and Robert M. Sweet. Characterizing and Simulating Needle Insertion Forces for Percutaneous Renal Access. *Journal of Endourology*, 30(10):1049–1055, October 2016. Publisher: Mary Ann Liebert Inc.

[PSW+00] Alexandru Patriciu, Dan Stoianovici, Louis L. Whitcomb, Thomas Jarrett, Dumitru Mazilu, Alexandru Stanimir, Iulian Iordachita, James Anderson, Russell Taylor, and Louis R. Kavoussi. Motion-Based Robotic

Instrument Targeting under C-Arm Fluoroscopy. In Gerhard Goos, Juris Hartmanis, Jan van Leeuwen, Scott L. Delp, Anthony M. DiGoia, and Branislav Jaramaz, editors, *Medical Image Computing and Computer-Assisted Intervention – MICCAI 2000*, volume 1935, pages 988–998. Springer Berlin Heidelberg, Berlin, Heidelberg, 2000.

[Qua] Quality Ablation - Standardized and Reproducible Tumour Treatments. https://www.cascination.com/en/quality-ablation.

[RACF+18] ANDREI ROMAN, PATRICIU ACHIMAS-CADARIU, BOGDAN FETICA, VLAD GATA, and ANDRADA SEICEAN. CT-guided procedures: an initial experience. *Clujul Medical*, 91(4):427, October 2018. Publisher: Universty of Medicine and Pharmacy of Cluj-Napoca, Romania.

[RBF21] Milovan Regodic, Zoltan Bardosi, and Wolfgang Freysinger. Automated fiducial marker detection and localization in volumetric computed tomography images: A three-step hybrid approach with deep learning. *Journal of Medical Imaging*, 8(2):025002, April 2021.

[RCNY+14] Hongliang Ren, Enrique Campos-Nanez, Ziv Yaniv, Filip Banovac, Hernan Abeledo, Nobuhiko Hata, and Kevin Cleary. Treatment Planning and Image Guidance for Radiofrequency Ablation of Large Tumors. *IEEE Journal of Biomedical and Health Informatics*, 18(3):920–928, May 2014. Conference Name: IEEE Journal of Biomedical and Health Informatics.

[Ris00] Risk Factors: Age - NCI. https://www.cancer.gov/about-cancer/causes-prevention/risk/age, 04/29/2015 - 08:00.

[RMK+11] Kyle B Reed, Ann Majewicz, Vinutha Kallem, Ron Alterovitz, Ken Goldberg, Noah J Cowan, and Allison M Okamura. Robot-assisted needle steering. *IEEE robotics & automation magazine*, 18(4):35–46, 2011.

[RSF13a] E. Rohmer, S. P. N. Singh, and M. Freese. V-rep: a versatile and scalable robot simulation framework. In *Proc. of The International Conference on Intelligent Robots and Systems (IROS)*, 2013.

[RSF13b] Eric Rohmer, Surya P N Singh, and Marc Freese. Coppeliasim (formerly V-REP): a versatile and scalable robot simulation framework. In *Proceedings of The International Conference on Intelligent Robots and Systems (IROS),(Tokyo). Available online at: www. coppeliarobotics. com*, 2013.

[RUM18] José R. Rojas-Solano, Luis Ugalde-Gamboa, and Michael MacHuzak. Robotic bronchoscopy for diagnosis of suspected lung cancer: A feasibility study. *Journal of bronchology & interventional pulmonology*, 25(3):168, July 2018.

[SAM+02] Solomon S, Patriciu A, Bohlman M, Kavoussi L, and Stoianovici D. Robotically Driven Interventions: A Method of Using CT Fluoroscopy without Radiation Exposure to the Physician. *Radiology*, 225(1):277–282, October 2002.

[SBM16] Michael Safaee, John Burke, and Michael W. McDermott. Techniques for the Application of Stereotactic Head Frames Based on a 25-Year Experience. *Cureus*, 8(3), March 2016. Publisher: Cureus.

[SCD+97] Dan Stoianovici, Jeffrey A. Cadeddu, Roger D. Demaree, Stephen A. Basile, Russell H. Taylor, Louis L. Whitcomb, William N. Sharpe, and Louis R. Kavoussi. An efficient needle injection technique and radiological guidance method for percutaneous procedures. *Lecture Notes in Computer Science (including subseries Lecture Notes in Artificial Intelligence and Lecture Notes in Bioinformatics)*, 1205:295–298, 1997.

[Sci] Scikit-image: Image processing in Python [PeerJ]. https://peerj.com/articles/453/.

[SCP+03a] D. Stoianovici, K. Cleary, A. Patriciu, D. Mazilu, A. Stanimir, N. Craciunoiu, V. Watson, and L. Kavoussi. AcuBot: a robot for radiological interventions. *IEEE Transactions on Robotics and Automation*, 19(5):927–930, October 2003. Conference Name: IEEE Transactions on Robotics and Automation.

[SCP+03b] Dan Stoianovici, Kevin Cleary, Alexandra Patriciu, Dumitru Mazilu, Alexandru Stanimir, Nicolae Craciunoiu, Vance Watson, and Louis Kavoussi. AcuBot: A Robot for Radiological Interventions. *IEEE Transactions on Robotics and Automation*, 19(5):927–930, 2003. Publisher: Institute of Electrical and Electronics Engineers Inc. ISBN: 1042-296X.

[SEHC+21] Davide Scorza, Sara El Hadji, Camilo Cortes, A Bertelsen, Francesco Cardinale, Giuseppe Baselli, Caroline Essert, and Elena De Momi. Surgical planning assistance in keyhole and percutaneous surgery: A systematic review. *Medical Image Analysis*, 67:101820, January 2021.

[SES+] Boris Schulz, Katrin Eichler, Petra Siebenhandl, Tatjana Gruber-Rouh, Christoph Czerny, Thomas Josef Vogl, and Stephan Zangos. Accuracy and speed of robotic assisted needle interventions using a modern cone beam computed tomography intervention suite: a phantom study.

[SES+11] Alexander Seitel, Markus Engel, Christof M. Sommer, Boris A. Radeleff, Caroline Essert-Villard, Claire Baegert, Markus Fangerau, Klaus H. Fritzsche, Kwong Yung, Hans-Peter Meinzer, and Lena Maier-Hein. Computer-assisted trajectory planning for percutaneous needle insertions. *Medical Physics*, 38(6Part1):3246–3259, 2011. _eprint: https://onlinelibrary.wiley.com/doi/pdf/10.1118/1.3590374.

[SES+13] Boris Schulz, Katrin Eichler, Petra Siebenhandl, Tatjana Gruber-Rouh, Christoph Czerny, Thomas Josef Vogl, and Stephan Zangos. Accuracy and speed of robotic assisted needle interventions using a modern cone beam computed tomography intervention suite: a phantom study. *European Radiology*, 23(1):198–204, January 2013.

[SFJ+05] R. Shamir, M. Freiman, L. Joskowicz, M. Shoham, E. Zehavi, and Y. Shoshan. Robot-assisted image-guided targeting for minimally invasive neurosurgery: Planning, registration, and in-vitro experiment". 8 th. international conference on medical image computing and conputer assisted intervention (MICCAI, 2005.

[Sha18] Navid Shahriari. *Flexible Needle Steering for Computed Tomography-Guided Interventions*. PhD thesis, University of Groningen, Groningen, 2018.

[SHOM15a] Navid Shahriari, Edsko Hekman, Matthijs Oudkerk, and Sarthak Misra. Design and evaluation of a computed tomography (CT)-compatible needle insertion device using an electromagnetic tracking system and CT images. *International Journal of Computer Assisted Radiology and Surgery*, 10(11):1845–1852, 2015.

[SHOM15b] Navid Shahriari, Edsko Hekman, Matthijs Oudkerk, and Sarthak Misra. Design and evaluation of a computed tomography (CT)-compatible needle insertion device using an electromagnetic tracking system and CT images. *International Journal of Computer Assisted Radiology and Surgery*, 10(11):1845–1852, November 2015. Publisher: Springer Verlag.

[SHv+17] Navid Shahriari, Wout Heerink, Tim van Katwijk, Edsko Hekman, Matthijs Oudkerk, and Sarthak Misra. Computed tomography (CT)-compatible remote center of motion needle steering robot: Fusing CT images and electromagnetic sensor data. *Medical Engineering & Physics*, 45:71–77, July 2017.

[SHvK+17] Navid Shahriari, Wout Heerink, Tim van Katwijk, Edsko Hekman, Matthijs Oudkerk, and Sarthak Misra. Computed tomography (CT)-compatible remote center of motion needle steering robot: Fusing

CT images and electromagnetic sensor data. *Medical Engineering & Physics*, 45:71–77, July 2017.

[SJA+10] Reuben R. Shamir, Leo Joskowicz, Luca Antiga, Roberto I. Foroni, and Yigal Shoshan. Trajectory planning method for reduced patient risk in image-guided neurosurgery: concept and preliminary results. In *Medical Imaging 2010: Visualization, Image-Guided Procedures, and Modeling*, volume 7625, page 76250I. SPIE, March 2010. Issue: 23 ISSN: 16057422.

[SJL+21] Peter Schullian, Edward Johnston, Gregor Laimer, Daniel Putzer, Gernot Eberle, Arno Amann, Maria Effenberger, Manuel Maglione, Martin C. Freund, Alexander Loizides, and Reto Bale. Frequency and risk factors for major complications after stereotactic radiofrequency ablation of liver tumors in 1235 ablation sessions: a 15-year experience. *European Radiology*, 31(5):3042–3052, May 2021.

[SK92a] W W Scott and J E Kuhlman. Phantom for use in lung biopsy training. *Radiology*, 184(1):286–287, 1992. Pmid: 1609095.

[SK92b] W. W. Scott and J. E. Kuhlman. Phantom for use in lung biopsy training. *Radiology*, 184(1):286–287, 1992.

[SKD+08a] S. Shah, A. Kapoor, J. Ding, P. Guion, D. Petrisor, J. Karanian, W. F. Pritchard, D. Stoianovici, B. J. Wood, and K. Cleary. Robotically assisted needle driver: evaluation of safety release, force profiles, and needle spin in a swine abdominal model. *International Journal of Computer Assisted Radiology and Surgery*, 3(1):173–179, June 2008.

[SKD+08b] S. Shah, A. Kapoor, J. Ding, P. Guion, D. Petrisor, J. Karanian, W. F. Pritchard, D. Stoianovici, B. J. Wood, and K. Cleary. Robotically assisted needle driver: evaluation of safety release, force profiles, and needle spin in a swine abdominal model. *International Journal of Computer Assisted Radiology and Surgery 2008 3:1*, 3(1):173–179, May 2008. Publisher: Springer.

[SKP+17] Dan Stoianovici, Chunwoo Kim, Doru Petrisor, Changhan Jun, Sunghwan Lim, Mark W. Ball, Ashley Ross, Katarzyna Jadwiga MacUra, and Mohamad E. Allaf. MR Safe Robot, FDA Clearance, Safety and Feasibility of Prostate Biopsy Clinical Trial. *IEEE/ASME Transactions on Mechatronics*, 22(1):115–126, February 2017.

[SMH+17] Philip J. Swaney, Arthur W. Mahoney, Bryan I. Hartley, Andria A. Remirez, Erik Lamers, Richard H. Feins, Ron Alterovitz, and Robert J.

Webster. Toward Transoral Peripheral Lung Access: Combining Continuum Robots and Steerable Needles. *Journal of Medical Robotics Research*, 02(01):1750001, March 2017.

[SMK12] Ioan A. Sucan, Mark Moll, and Lydia E. Kavraki. The Open Motion Planning Library. *IEEE Robotics & Automation Magazine*, 19(4):72–82, December 2012. Conference Name: IEEE Robotics & Automation Magazine.

[SMR+15] Philip J. Swaney, Arthur W. Mahoney, Andria A. Remirez, Erik Lamers, Bryan I. Hartley, Richard H. Feins, Ron Alterovitz, and Robert J. Webster. Tendons, concentric tubes, and a bevel tip: Three steerable robots in one transoral lung access system. In *Robotics and Automation (ICRA), 2015 IEEE International Conference On*, volume 2015-June, pages 5378–5383. IEEE, June 2015.

[SMW+21] Françoise J. Siepel, Bogdan Maris, Marcel K. Welleweerd, Vincent Groenhuis, Paolo Fiorini, and Stefano Stramigioli. Needle and Biopsy Robots: a Review. *Current Robotics Reports*, 2(1):73–84, March 2021.

[SPB+02] Stephen B. Solomon, Alexandru Patriciu, Mark E. Bohlman, Louis R. Kavoussi, and Dan Stoianovici. Robotically driven interventions: A method of using CT fluoroscopy without radiation exposure to the physician. *Radiology*, 225(1):277–282, October 2002. Publisher: Radiological Society of North America Inc.

[SSH+09] Benjamin D. Smith, Grace L. Smith, Arti Hurria, Gabriel N. Hortobagyi, and Thomas A. Buchholz. Future of Cancer Incidence in the United States: Burdens Upon an Aging, Changing Nation. *Journal of Clinical Oncology*, 27(17):2758–2765, June 2009.

[ŠŠJ+17] Filip Šuligoj, Marko Švaco, Bojan Jerbić, Bojan Šekoranja, and Josip Vidaković. Automated Marker Localization in the Planning Phase of Robotic Neurosurgery. *IEEE Access*, 5:12265–12274, 2017.

[SSNY19] D.A. DImitri A. Schreiber, D.B. Daniel B. Shak, Alexander M. A.M. Norbash, and Michael C. Yip. An Open-Source 7-Axis, Robotic Platform to Enable Dexterous Procedures within CT Scanners. In *IEEE International Conference on Intelligent Robots and Systems*, pages 386–393. Institute of Electrical and Electronics Engineers Inc., November 2019.

[SWA+98] Dan Stoianovici, Louis L. Whitcomb, James H. Anderson, Russell H. Taylor, and Louis R. Kavoussi. A modular surgical robotic system for image guided percutaneous procedures. In *Lecture Notes in Computer Science (including subseries Lecture Notes in Artificial Intelligence*

and Lecture Notes in Bioinformatics), volume 1496, pages 404–410. Springer Verlag, 1998. ISSN: 16113349.

[SWH+09a] Alexander Seitel, Conor J. Walsh, Nevan C. Hanumara, Jo-Anne Shepard, Alexander H. Slocum, Hans-Peter Meinzer, Rajiv Gupta, and Lena Maier-Hein. Development and evaluation of a new image-based user interface for robot-assisted needle placements with the Robopsy system. In *Medical Imaging 2009: Visualization, Image-Guided Procedures, and Modeling*, volume 7261, pages 305–313. SPIE, March 2009.

[SWH+09b] Alexander Seitel, Conor J. Walsh, Nevan C. Hanumara, Jo-Anne Shepard, Alexander H. Slocum, Hans-Peter Meinzer, Rajiv Gupta, and Lena Maier-Hein. Development and evaluation of a new image-based user interface for robot-assisted needle placements with the Robopsy system. 7261(March 2009):72610X, 2009.

[SYJ+22] Dimitri Schreiber, Zhaowei Yu, Hanpeng Jiang, Taylor Henderson, Guosong Li, Julie Yu, Renjie Zhu, Alexander M. Norbash, and Michael C. Yip. CRANE: A 10 Degree-of-Freedom, Tele-surgical System for Dexterous Manipulation within Imaging Bores. In *2022 International Conference on Robotics and Automation (ICRA)*, pages 5487–5494, May 2022.

[TATPO+11a] Saúl Tovar-Arriaga, Ralf Tita, Jesús Carlos Pedraza-Ortega, Efren Gorrostieta, and Willi A. Kalender. Development of a robotic FD-CT-guided navigation system for needle placement–preliminary accuracy tests. *The International Journal of Medical Robotics and Computer Assisted Surgery*, 7(2):225–236, 2011. _eprint: https://onlinelibrary.wiley.com/doi/pdf/10.1002/rcs.393.

[TATPO+11b] Saúl Tovar-Arriaga, Ralf Tita, Jesús Carlos Pedraza-Ortega, Efren Gorrostieta, and Willi A. Kalender. Development of a robotic FD-CT-guided navigation system for needle placement-preliminary accuracy tests. *International Journal of Medical Robotics and Computer Assisted Surgery*, 7(2):225–236, June 2011. Publisher: John Wiley & Sons, Ltd.

[TCO08] Nikolaos V. Tsekos, Eftychios Christoforou, and Alpay Ozcan. A General-Purpose MR-Compatible Robotic System. *IEEE Engineering in Medicine and Biology Magazine*, 27(3):51–58, May 2008. Conference Name: IEEE Engineering in Medicine and Biology Magazine.

[TDC+10] Michael J. Thun, John Oliver DeLancey, Melissa M. Center, Ahmedin Jemal, and Elizabeth M. Ward. The global burden of cancer: Priorities for prevention. *Carcinogenesis*, 31(1):100–110, January 2010.

[Tea13] National Lung Screening Trial Research Team. Results of initial low-dose computed tomographic screening for lung cancer. *New England Journal of Medicine*, 368(21):1980–1991, 2013.

[TKCM07] Nikolaos Tsekos, Azadeh Khanicheh, Eftychios Christoforou, and Constantinos Mavroidis. Magnetic resonance–compatible robotic and mechatronics systems for image-guided interventions and rehabilitation: A review study. *Annu. Rev. Biomed. Eng.*, 9:351–387, 2007.

[TKII18] Ryosuke Tsumura, Jin Seob Kim, Hiroyasu Iwata, and Iulian Iordachita. Preoperative Needle Insertion Path Planning for Minimizing Deflection in Multilayered Tissues. *IEEE Robotics and Automation Letters*, 3(3):2129–2136, July 2018.

[TOC05] Nikolaos V. Tsekos, Alpay Özcan, and Eftychios Christoforou. A Prototype Manipulator for Magnetic Resonance-Guided Interventions Inside Standard Cylindrical Magnetic Resonance Imaging Scanners. *Journal of Biomechanical Engineering*, 127(6):972–980, August 2005.

[TTC+09] I. Chen Tsai, Wei Lin Tsai, Min Chi Chen, Gee Chen Chang, Wen Sheng Tzeng, Si Wa Chan, and Clayton Chi Chang Chen. CT-guided core biopsy of lung lesions: A primer. *American Journal of Roentgenology*, 193(5):1228–1235, November 2009.

[TTP+11] Saúl Tovar-Arriaga, Ralf Tita, Jesús Carlos Pedraza-Ortega, Efren Gorrostieta, and Willi A. Kalender. Development of a robotic FD-CT-guided navigation system for needle placement-preliminary accuracy tests. *International Journal of Medical Robotics and Computer Assisted Surgery*, 7(2):225–236, June 2011.

[Tur] Robert Turocy. K974513. https://www.accessdata.fda.gov/scripts/cdrh/cfdocs/cfpmn/pmr

[TWL+17] Panwen Tian, Ye Wang, Lei Li, Yongzhao Zhou, Wenxin Luo, and Weimin Li. CT-guided transthoracic core needle biopsy for small pulmonary lesions: Diagnostic performance and adequacy for molecular testing. *Journal of Thoracic Disease*, 9(2):333–343, 2017.

[UBM21] Michael Unger, Johann Berger, and Andreas Melzer. Robot-Assisted Image-Guided Interventions. *Frontiers in Robotics and AI*, 8, 2021.

[vBWSH21] Kirsten van Baarsen, Peter Woerdeman, Mariam Slot, and Eelco Hoving. ITVT-07. Robotic alignment module Cirq for navigated brainstem tumor biopsies. *Neuro-Oncology*, 23(Supplement_6):vi229, November 2021.

[vdBPA+11] Jur van den Berg, Sachin Patil, Ron Alterovitz, Pieter Abbeel, and Ken Goldberg. LQG-Based Planning, Sensing, and Control of Steerable Needles. In David Hsu, Volkan Isler, Jean-Claude Latombe, and

Ming C. Lin, editors, *Algorithmic Foundations of Robotics IX: Selected Contributions of the Ninth International Workshop on the Algorithmic Foundations of Robotics*, Springer Tracts in Advanced Robotics, pages 373–389. Springer, Berlin, Heidelberg, 2011.

[vvDv15] Nick J van de Berg, Dennis J van Gerwen, Jenny Dankelman, and John J van den Dobbelsteen. Design choices in needle steering—A review. *IEEE/ASME Transactions on Mechatronics*, 20(5):2172–2183, 2015.

[Wal10] Conor James Walsh. Image-guided robots for dot-matrix tumor ablation. *A. Mechanical and Manufacturing Engineering*, 2010. Publisher: Massachusetts Institute of Technology.

[Wei21] Hannah K. Weir. Cancer Incidence Projections in the United States Between 2015 and 2050. *Preventing Chronic Disease*, 18, 2021.

[WHS+07] Conor James Walsh, Nevan Hanumara, Alexander Slocum, Rajiv Gupta, and Jo-Anne Anne Shepard. Evaluation of a patient-mounted, remote needle guidance and insertion system for CT-guided, percutaneous lung biopsies. In *ASME 2007 2nd Frontiers in Biomedical Devices Conference*, pages 39–40. American Society of Mechanical Engineers, American Society of Mechanical Engineers, 2007.

[WHS+08a] Conor J. Walsh, Nevan C. Hanumara, Alexander H. Slocum, Jo Anne Shepard, and Rajiv Gupta. A patient-mounted, telerobotic tool for CT-guided percutaneous interventions. *Journal of Medical Devices, Transactions of the ASME*, 2(1):011007, March 2008.

[WHS+08b] Conor J Walsh, Nevan C. Hanumara, Alexander H. Slocum, Jo-Anne Shepard, and Rajiv Gupta. A patient-mounted, telerobotic tool for ct-guided percutaneous interventions. *ASME Journal of Medical Devices*, 2(1), 2008.

[WHS+09] Conor James Walsh, Nevan Hanumara, Alexander Slocum, Rajiv Gupta, and Jo-Anne Shepard. Evaluation of a Patient-Mounted, Remote Needle Guidance and Insertion System for CT-Guided, Percutaneous Lung Biopsies. pages 39–40. American Society of Mechanical Engineers Digital Collection, February 2009.

[WJTT16] Ye Wang, Faming Jiang, Xiaobo Tan, and Panwen Tian. CT-guided percutaneous transthoracic needle biopsy for paramediastinal and non-paramediastinal lung lesions: Diagnostic yield and complications in 1484 patients. *Medicine*, 95(31), 2016.

[WKK+17] Hyung Jin Won, Namkug Kim, Guk Bae Kim, Joon Beom Seo, and Hongho Kim. Validation of a CT-guided intervention robot for biopsy

and radiofrequency ablation: experimental study with an abdominal phantom. *Diagnostic and Interventional Radiology*, 23(3):233–237, May 2017.

[WLH+14] Ying Wang, Wentao Li, Xinhong He, Guodong Li, and Lichao Xu. Computed tomography-guided core needle biopsy of lung lesions: Diagnostic yield and correlation between factors and complications. *Oncology Letters*, 7(1):288–294, January 2014.

[WLP+19a] Di Wu, Gang Li, Niravkumar Patel, Jiawen Yan, Reza Monfaredi, Kevin Cleary, and Iulian Iordachita. Remotely Actuated Needle Driving Device for MRI-Guided Percutaneous Interventions. In *2019 International Symposium on Medical Robotics (ISMR)*, pages 1–7, April 2019.

[WLP+19b] Di Wu, Gang Li, Niravkumar Patel, Jiawen Yan, Reza Monfaredi, Kevin Cleary, and Iulian Iordachita. Remotely Actuated Needle Driving Device for MRI-Guided Percutaneous Interventions, 5 2019.

[WM04] J.B. West and C.R. Maurer. Designing optically tracked instruments for image-guided surgery. *IEEE Transactions on Medical Imaging*, 23(5):533–545, May 2004.

[WSH+11a] Gerlig Widmann, Peter Schullian, Marion Haidu, Martin Fasser, and Reto Bale. Targeting accuracy of CT-guided stereotaxy for radiofrequency ablation of liver tumours. *Minimally Invasive Therapy & Allied Technologies*, 20(4):218–225, July 2011. Publisher: Taylor & Francis _eprint: https://doi.org/10.3109/13645706.2010.533923.

[WSH+11b] Gerlig Widmann, Peter Schullian, Marion Haidu, Martin Fasser, and Reto Bale. Targeting accuracy of CT-guided stereotaxy for radiofrequency ablation of liver tumours. *Minimally Invasive Therapy & Allied Technologies*, 20(4):218–225, July 2011.

[WSOB12a] Gerlig Widmann, Peter Schullian, Martin Ortler, and Reto Bale. Frameless stereotactic targeting devices: technical features, targeting errors and clinical results. *The International Journal of Medical Robotics and Computer Assisted Surgery*, 8(1):1–16, 2012. _eprint: https://onlinelibrary.wiley.com/doi/pdf/10.1002/rcs.441.

[WSOB12b] Gerlig Widmann, Peter Schullian, Martin Ortler, and Reto Bale. Frameless stereotactic targeting devices: Technical features, targeting errors and clinical results. *The International Journal of Medical Robotics and Computer Assisted Surgery*, 8(1):1–16, 2012.

[WSWW11] Renda Soylemez Wiener, Lisa M. Schwartz, Steven Woloshin, and H. Gilbert Welch. Population-based risk of complications following

transthoracic needle lung biopsy of a pulmonary nodule. *Annals of internal medicine*, 155(3):137–144, August 2011.

[WTE+07] Max J. Warnock, Christopher Toland, Damien Evans, Bill Wallace, and Paul Nagy. Benefits of Using the DCM4CHE DICOM Archive. *Journal of Digital Imaging*, 20(Suppl 1):125–129, November 2007.

[WTW+14] D. Wallach, G. Toporek, S. Weber, R. Bale, and G. Widmann. Comparison of freehand-navigated and aiming device-navigated targeting of liver lesions. *The International Journal of Medical Robotics and Computer Assisted Surgery*, 10(1):35–43, 2014. _eprint: https://onlinelibrary.wiley.com/doi/pdf/10.1002/rcs.1505.

[xac] Homepage - XACT Robotics. https://xactrobotics.com/.

[XDAG08] Jijie Xu, Vincent Duindam, Ron Alterovitz, and Ken Goldberg. Motion planning for steerable needles in 3D environments with obstacles using rapidly-exploring Random Trees and backchaining. In *2008 IEEE International Conference on Automation Science and Engineering*, pages 41–46, August 2008. ISSN: 2161-8089.

[Yan10] Ziv Yaniv. Evaluation of spherical fiducial localization in C-arm cone-beam CT using patient data: Evaluation of spherical fiducial localization in C-arm cone-beam. *Medical Physics*, 37(10):5298–5305, September 2010.

[YJY+17] Yunpeng Yang, Shan Jiang, Zhiyong Yang, Wei Yuan, Huaisu Dou, Wei Wang, Daguang Zhang, and Yuan Bian. Design and analysis of a tendon-based computed tomography-compatible robot with remote center of motion for lung biopsy. *Proceedings of the Institution of Mechanical Engineers, Part H: Journal of Engineering in Medicine*, 231(4):286–298, 2017.

[YLJB18] Ziv Yaniv, Bradley C. Lowekamp, Hans J. Johnson, and Richard Beare. SimpleITK Image-Analysis Notebooks: A Collaborative Environment for Education and Reproducible Research. *Journal of Digital Imaging*, 31(3):290–303, June 2018.

[YLL+09] Lifeng Yu, Xin Liu, Shuai Leng, James M Kofler, Juan C Ramirez-Giraldo, Mingliang Qu, Jodie Christner, Joel G Fletcher, and Cynthia H McCollough. Radiation dose reduction in computed tomography: techniques and future perspective. *Imaging in medicine*, 1(1):65–84, October 2009.

[Yos85] Tsuneo Yoshikawa. Manipulability of Robotic Mechanisms. *The International Journal of Robotics Research*, 4(2):3–9, June 1985. Publisher: SAGE Publications Ltd STM.

[You] Jae You. Brief communication (Original). Multimodal imaging fiducial markers for kinematic measurement of joint models. https://sciendo.com/article/10.5372/1905-7415.0704.205.

[YWQ+10] Liangjing Yang, Rong Wen, Jing Qin, Chee Kong Chui, Kah Bin Lim, and Stephen Kin Yong Chang. A robotic system for overlapping radiofrequency ablation in large tumor treatment. *IEEE/ASME Transactions on Mechatronics*, 15(6):887–897, December 2010.

[ZME+11] Stephan Zangos, Andreas Melzer, Katrin Eichler, Cyrus Sadighi, Axel Thalhammer, Boris Bodelle, Renate Wolf, Tatjana Gruber-Rouh, Dirk Proschek, Renate Hammerstingl, Cindy Müller, Martin G. Mack, and Thomas J. Vogl. MR-compatible Assistance System for Biopsy in a High-Field-Strength System: Initial Results in Patients with Suspicious Prostate Lesions. *Radiology*, 259(3):903–910, June 2011. Publisher: Radiological Society of North America.

[ZPK18] Qian-Yi Zhou, Jaesik Park, and Vladlen Koltun. Open3D: A Modern Library for 3D Data Processing, January 2018.

[ZSS+20] Yichen Zhang, Lizheng Shi, Michael J Simoff, Oliver J Wagner, and James Lavin. Biopsy frequency and complications among lung cancer patients in the United States. *Lung Cancer Management*, 9(4):LMT40, December 2020.

[ZTK+11] Yu Zhou, Kaarvannan Thiruvalluvan, Lukasz Krzeminski, William H. Moore, Zhigang Xu, and Zhengrong Liang. An experimental system for robotic needle biopsy of lung nodules with respiratory motion. In *2011 IEEE International Conference on Mechatronics and Automation, ICMA 2011*, 2011.